UNIVERSITY OF SOUTHAMPTON

FACULTY OF ENGINEERING, SCIENCE AND MATHEMATICS

School of Physics and Astronomy

MAGNETIZATION SWITCHING AND SPIN-DEPENDENT TRANSPORT IN $REFe_2$ EXCHANGE SPRING MULTILAYERS

By Kevin Norman Martin

Thesis for the degree of Doctor of Philosophy

July 2008

UNIVERSITY OF SOUTHAMPTON

ABSTRACT

FACULTY OF ENGINEERING SCIENCE AND MATHEMATICS

SCHOOL OF PHYSICS AND ASTRONOMY

Doctor of Philosophy

MAGNETIZATION SWITCHING AND SPIN-DEPENDENT TRANSPORT IN $REFe_2$ EXCHANGE SPRING MULTILAYERS

By Kevin Norman Martin

The properties of rare earth-transition metal Laves phase films and multilayers, grown by molecular beam epitaxy, form the subject of this thesis. In particular, $ErFe_2/YFe_2$ superlattices, which order magnetically out of plane, are discussed in some detail. When a magnetic field is applied out of plane, magnetic exchange springs form in the soft YFe_2 layers. These exchange springs result in broad reversible regions in the hysteresis curve, which can lead to negative coercivity in multilayers given sufficiently thick soft layers. However, there is a cross-over temperature, T_{CO}, above which the coercivity of these multilayers becomes positive, with additional transitions at high fields. The spin configurations occurring in $ErFe_2/YFe_2$ multilayers during magnetic reversal have been studied using bulk magnetometry and micromagnetic modelling. At high fields and high temperatures, the magnetization of the hard layers points in-plane, at right angles to the applied magnetic field.

In addition, more complex $ErFe_2/YFe_2/DyFe_2/YFe_2$ superlattices have also been created, where there is competition between the anisotropies of the $ErFe_2$ and $DyFe_2$ layers. The coupling between the different hard Er/Dy layers is easily changed by varying the soft YFe_2 layer thickness. The interactions between the competing Er and Dy anisotropies are mediated both by soft layer thickness and temperature. A rich phase diagram of switching processes has been identified.

Finally, the galvanomagnetic properties of $ErFe_2/YFe_2$ multilayers have been investigated using magneto-transport measurements. Both exchange spring giant magnetoresistance and the anomalous Hall effect are described in detail. The Hall effect data is complemented with results both from bulk magnetometry and micromagnetic modelling. It is shown that the anomalous Hall effect couples mainly to the Fe magnetisation in $ErFe_2/YFe_2$ multilayers. Nevertheless, very specific information about the magnetisation processes can be obtained from Hall effect measurements.

Contents

Chapter 1. Introduction 1

Chapter 2. Background 5

2.1. Recent and current research in magnetic materials 6
2.2. Magnetism of $REFe_2$ intermetallics 14
2.3. Exchange springs in $REFe_2$ films and multilayers 19
2.4. Transport properties of $REFe_2$ films and multilayers 24

Chapter 3. Experimental techniques 32

3.1. Molecular Beam Epitaxy 33
3.2. The Vibrating Sample Magnetometer 36
3.3. Magneto-transport 41

Chapter 4. Exchange spring driven spin-flop in $ErFe_2/YFe_2$ multilayers 48

4.1. Exchange springs in $ErFe_2/YFe_2$ multilayers 49
4.2. Multilayer spin-flop 55
4.3. Conclusions 61

Chapter 5. Multilayers with competing anisotropies 62

5.1. $ErFe_2/YFe_2/DyFe_2/YFe_2$ multilayers 63
5.2. Magnetic switching patterns 65
5.3. Conclusions 75

Chapter 6. Giant magnetoresistance and the anomalous Hall effect in $REFe_2$ laves phase materials 76

6.1. Giant magnetoresistance in $REFe_2$ films and superlattices 77
6.2. Anomalous Hall effect in $REFe_2$ films and superlattices 84
6.3. Conclusions 90

Chapter 7. Summary 91

References 95

Publications 98

DECLARATION OF AUTHORSHIP

I, Kevin Norman Martin, declare that the thesis entitled

MAGNETIZATION SWITCHING AND SPIN-DEPENDENT TRANSPORT IN $REFe_2$ EXCHANGE SPRING MULTILAYERS

and the work presented in the thesis are both my own, and have been generated by me as the result of my own original research. I confirm that:

- this work was done wholly or mainly while in candidature for a research degree at this University;
- where any part of this thesis has previously been submitted for a degree or any other qualification at this University or any other institution, this has been clearly stated;
- where I have consulted the published work of others, this is always clearly attributed;
- where I have quoted from the work of others, the source is always given. With the exception of such quotations, this thesis is entirely my own work;
- I have acknowledged all main sources of help;
- where the thesis is based on work done by myself jointly with others, I have made clear exactly what was done by others and what I have contributed myself;
- parts of this work have been published as;

K. N. Martin *et al.*, J. Appl. Phys. **101**, 09K511 (2007).
K. N. Martin *et al.*, Appl. Phys. Lett. **89**, 132511 (2006)

Acknowledgements

I would like to take this opportunity to thank some of the people that have helped to make this thesis possible. Firstly, I would like to thank my supervisor, Peter de Groot, for his advice and support throughout my studies. Secondly, Graham Bowden, for helping me write better papers and for working with me at facilities. I would also like to thank Sasha Zhukov and Ed Filby, for showing me the ropes when I started. I thank Chris Morrison, for his valuable help and company during the long days in Grenoble. I'd also like to thank Ke Wang for the help he provided and for many thought provoking conversations. In addition, I thank other students and ex students in the group: Clare Horn, Sasha Goncharov, John O'Neill, Daowei Wang, Atef Ahmed and Roger Buckingham.

The project would not have been possible without the aid of Roger Ward, head of the MBE group at Oxford University. Also, none of the in-house experiments could have been performed without the aid of Dennis Torkington, Colin Miles, Tom Perkins and Justin Harris, who provided me with technical assistance as well as essential cryogenic liquids. I would also like to thank Ilya Sheikin, Eric Mossang, Christiane Warth-Martin, Hanka Zeman and Kim Pla of the Grenoble High Magnetic Field Laboratory.

Finally, I could not have completed this thesis without the help of my family, particularly my parents Garry and Judy Martin, who have supported me throughout my entire undergraduate and post graduate career.

Chapter 1. Introduction

Research into exchange spring magnets has flourished in recent years. These magnets consist of a hard magnetic material exchange coupled to a soft magnetic material. A magnetic multilayer, consisting of alternating hard and soft magnetic layers, is just one example. In fact, magnetic multilayers have been studied for over 60 years [1]. However, recent advances in modern deposition methods have vastly expanded the possibilities for engineering magnetic materials with prescribed properties. One such method is Molecular Beam Epitaxy (MBE), a technique originally developed for semiconductor production. This technique can be used to create multilayers possessing a specific crystalline orientation, artificially structured on the nanometre scale, with specific properties [2]. The ability to produce man made magnetic materials, with novel properties, has revitalized basic and applied research in magnetism [3].

In this thesis, we report the characterization of MBE grown $REFe_2$ multilayers and thick films. Rare earth-transition metal (R-TM) intermetallics represent an important class of magnetic materials. The rare earth ions possess high magnetocrystalline anisotropy while the transition metal has a large saturation magnetization. The combination of these two properties is ideal for permanent magnets. Hard magnets based on $SmCo_5$, for example, have the highest uniaxial anisotropies of any magnet, of the order of 10^7 J/m^3 [4]. Magnets based on $Fe_{14}Nd_2B$ boast the highest energy products so far achieved, in excess of 50 MGOe [5]. R-TM intermetallics also exhibit giant magnetostriction [6], a property utilized extensively to create powerful actuators and motors. R-TM films and multilayers have uses in MEMS [7]. Additionally, the $REFe_2$ multilayers that are the subject of this thesis exhibit magnetic exchange springs. Materials such as these could have important applications in data storage media [8].

The aim of this work has been to study the magnetic reversal and transport properties of the $REFe_2$ multilayers. Exchange spring multilayers make ideal model systems for studying exchange spring phenomena [9, 10]. Understanding the basic properties of

exchange springs is essential if technical applications are to be realized. This project builds on a large amount of research conducted on $DyFe_2$ films and $DyFe_2/YFe_2$ multilayers [11]. Such materials display useful features such as tuneable coercivity [2] and giant magnetoresistance (GMR) [12]. More recently, $ErFe_2$ films and $ErFe_2/YFe_2$ multilayers have been grown. These materials order magnetically out of plane. This facilitates the study of other phenomena, such as the anomalous Hall effect (AHE). The anomalous Hall effect is still a poorly understood phenomenon. As the materials are single crystals and can be grown very thin, they are ideal for AHE studies. The MBE method has also been used to create crystalline samples of mixed multilayers such as $ErFe_2/YFe_2/DyFe_2/YFe_2$ and $ErFe_2/DyFe_2$ [13]. These multilayers are characterized by competing anisotropies, which allow very different kinds of exchange spring systems to be investigated.

MBE grown multilayers allow a great deal of control over the material parameters. Variables such as the thicknesses of the component layers and the total thickness of the multilayer are easily tailored for specific experiments. In addition, by their very nature, the samples are single crystals. This allows material properties such as the magnetocrystalline anisotropy to be examined, as well as allowing patterning along known crystalline directions [14-16]. This last point is especially important in the study of transport properties. The characterization methods employed in this work include magnetometry and magneto-transport. In addition, extensive micromagnetic modelling work has been performed in a parallel project by Jurgen Zimmerman, in the Computational Engineering and Design Group, School of Engineering Sciences.

In chapter 2 of this thesis an overview is given of research in nanomagnetism. This section sets the context for the research detailed in this thesis. Particular attention is given to those areas where exchange spring magnets have recently attracted a great deal of attention, such as permanent magnets and data storage. Section 2.1 finishes with an overview of the recent research into R-TM intermetallics, which the work reported in later chapters of this thesis builds upon. Section 2.2 describes the most important aspects of the magnetism of $REFe_2$ intermetallics. In particular, the interactions that lead to the formation of magnetic exchange springs are identified. This is followed by a description of both in-plane and out of plane exchange springs in $REFe_2$ multilayers. The effect of exchange springs on the technical aspects of the

hysteresis loops of these materials is also explained. The last part of the chapter details the galvanomagnetic properties of $REFe_2$ intermetallics, in particular the AHE and GMR.

In Chapter 3 the experimental techniques used to create and characterize $REFe_2$ films and multilayers are briefly discussed. The first technique described, in section 3.1, is Molecular Beam Epitaxy. Both the basic principals of MBE and the specific techniques used to grow the $REFe_2$ materials are explained. The Vibrating Sample Magnetometer (VSM), used to collect bulk magnetization data, is the subject of section 3.2. The basic physical principals of the VSM are explained, along with the specific techniques employed to measure hysteresis loops of $REFe_2$ films and multilayers. Electronic transport measurements are the subject of section 3.3. The basic experimental set up is described, along with point contact measurements, patterning techniques and the separation of different components of the data.

In chapter 4, both bulk magnetometry and micromagnetic modelling on $ErFe_2/YFe_2$ multilayers are presented and discussed. At low temperatures, the magnetic reversal of these exchange spring multilayers displays many of the features described in chapter 2. In particular, there is a cross-over temperature T_{CO}, above which the character of the hysteresis loop changes dramatically. Above T_{CO}, the magnetic reversal process becomes more complex, with additional transitions at high fields. The spin configurations adopted by the multilayers are identified, using micromagnetic modelling as a guide. Another interesting feature is the exchange spring driven spin-flop which occurs at high fields and high temperatures. This behaviour is explained in terms of simple energy arguments, which also allow the dependence of T_{CO} on the composition of the multilayer to be understood.

In chapter 5, bulk magnetometry and micromagnetic modelling, this time on $ErFe_2/YFe_2/DyFe_2/YFe_2$ multilayers, are presented and discussed. These multilayers contain two different magnetically hard materials, $ErFe_2$ and $DyFe_2$. The two different types of hard layer have competing magnetic anisotropy. The coupling between the hard layers varies with both the temperature and the thickness of the magnetically soft YFe_2 layers. It leads to a complex phase diagram of switching processes.

Transport measurements of $ErFe_2/YFe_2$ multilayers are the subject of chapter 6. The first section details GMR due to exchange springs. The GMR increases with the tightness of the exchange springs. For fields applied in plane, it is found that there are still irreversible processes occurring in fields above 20 T. With the field applied out of plane, the anomalous Hall effect quickly becomes important. In section 6.2, AHE measurements on $ErFe_2$ and $ErFe_2/YFe_2$ multilayers are presented and discussed. The experimental results are complemented by modelled hysteresis curves. In $ErFe_2/YFe_2$ multilayers, it is shown that the AHE couples mainly to the Fe magnetization. As the $ErFe_2$ layers themselves contain Fe moments, any change in the Er magnetization leads to a concomitant change in the Fe magnetization. In this sense, the AHE can be considered element specific. Indeed, the AHE provides additional information that cannot be obtained through bulk magnetometry.

Finally, in chapter 7 a summary of the project and this thesis can be found. The main results are restated with a brief explanation.

Chapter 2. Background

A brief review is given of the recent and current research in magnetic materials and exchange spring media, in the first part of this chapter. It deals with the concepts that are important for understanding the results presented in this thesis. A review of some of the basic magnetic properties of $REFe_2$ materials is given first, which is followed by a description of exchange springs in $ErFe_2/YFe_2$ multilayers. In particular, the conditions that lead to the formation of exchange springs are detailed, along with their effect on reducing the coercivity of the hysteresis loops of $REFe_2$ multilayers. The experimental results and their simulation are detailed in chapters 4 and 5. The final part of this chapter focuses on the transport properties of $REFe_2$ films and multilayers, including the anomalous Hall effect and giant magnetoresistance. Experimental studies of these two effects are presented and discussed in chapter 6.

2.1. Recent and current research in magnetic materials

In recent years there has been a great deal of interest in nano-magnetism, with applications suggested in fields such as microelectromechanical systems (MEMS) [7, 17-20], data storage [8, 21, 22] and even drug delivery [23]. The nano-magnets in this thesis can be described simply as $REFe_2$ exchange spring magnets. Rare earth transition metal composites have a secure place in the subject we call magnetism, thanks to their use as magnetostrictive materials, permanent magnets and magneto-optical data storage media [24, 25]. The figure of merit for a permanent magnet is its maximum energy product, $(BH)_{max}$, in the second quadrant of the magnetization curve. The theoretical maximum energy product of a material is an intrinsic property defined by [26]

$$(BH)^*_{max} = \mu_0 M_0^2 / 4 \qquad (2.1)$$

where M_0 is the spontaneous magnetization, equal to the remanence for an ideal rectangular hysteresis loop. To achieve a high $(BH)_{max}$, a material must possess a large saturation magnetization and high coercivity. At present, the record energy product is held by $Nd_2Fe_{14}B$ magnets, which have $(BH)_{max}$ in excess of 50 MGOe [5] while the theoretical limit is 516 kJ/m^3 (62 MGOe).

The development of magnets with higher $(BH)_{max}$ over the last century, is shown schematically in Fig 2.1. The dates and energy products are taken from Beaujour (2003) [11]. Early permanent magnets were created by adding carbon impurities to soft iron. Such impurities harden the iron, both mechanically and magnetically. Another example is Tungsten steel, first used in the 1940's [4]. These have modest coercivities of about 90 Oe. Co-Mo and Co-Cr steels possess coercivities of about 180 Oe and energy products around 1 MGOe.

The first magnets offering significantly better performance were Alnico (Al, Ni and Co) materials. They provide energy products of 1.5 – 7.5 MGOe and have excellent corrosion resistance [11]. Manufacturing Alnico magnets involves precipitating elongated ferromagnetic Fe-Co particles throughout an Al-Ni matrix. The hard

magnetism of Alnico magnets derives from the shape of these particles. From the late 1930's onwards, Alnico has been used in many applications, in motors and loudspeakers [4].

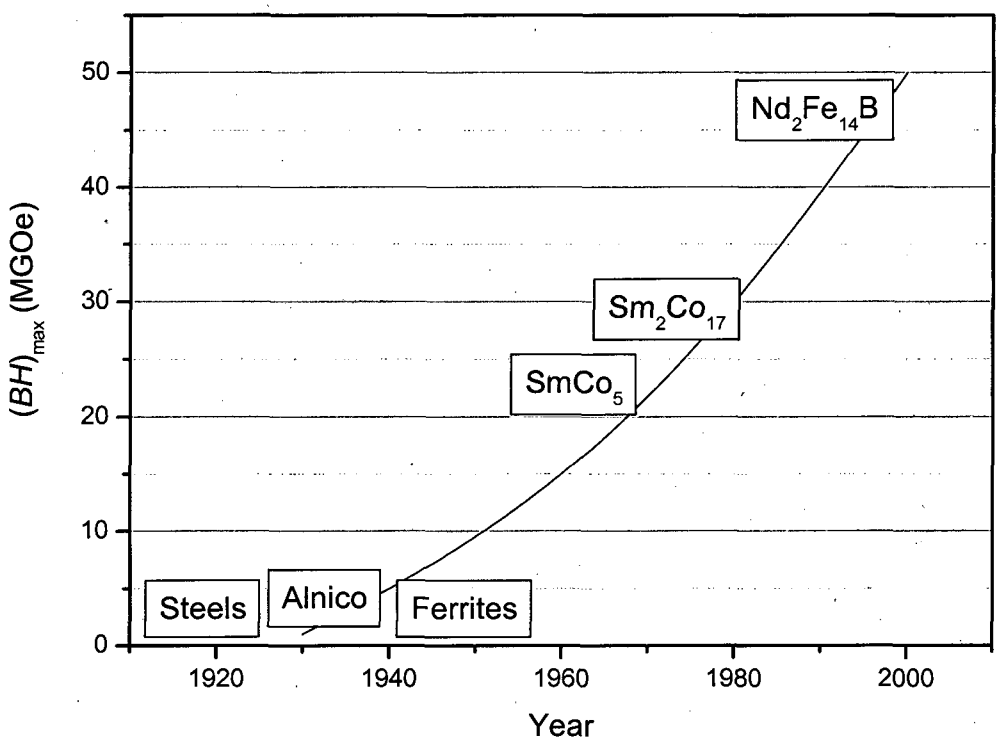

Figure 2.1. Increase in $(BH)_{max}$ of permanent magnets over the last century. Taken from Beaujour (2003)

However, the bulk of permanent magnets made today are hard ferrites. These are predominantly complex oxides, developed by powder metallurgical methods. They provide coercive forces three to eight times greater than most Alnicos, but their maximum energy product $(BH)_{max}$ is relatively low. The low cost and high coercive field of these magnets have made them particularly attractive in applications such as separators, motors and speakers [27].

Rare earth-transition metal intermetallics currently provide the best permanent magnet properties. SmCo magnets are the materials of choice for small, high performance devices operating between 175 – 350 °C. They are hard, brittle materials, often pressed or moulded into shape to avoid machining. Unfortunately, the rare earth content of these magnets also makes them relatively expensive. Single phase $SmCo_5$ can exhibit room temperature coercivity of 40 kOe, while magnets based on Sm_2Co_{17}

provide $(BH)_{max}$ up to 30 MGOe [4]. They are used in applications such as watches, motors, generators and magnetic bearings. Magnets based on $Nd_2Fe_{14}B$ can have $(BH)_{max}$ in excess of 50 MGOe [5]. However, the high Fe content of these magnets means they are susceptible to corrosion and in many applications require a corrosion resistant coating [27].

In the early 90's Skomski and Coey [26, 28, 29] predicted that permanent magnets with an energy product as high as 1 MJ/m^3 (120 MG Oe) could be made with a rare earth content of only 5 wt %. They imagined a composite material made from an aligned hard-magnetic phase with very high anisotropy, embedded in a soft-magnetic matrix with a high saturation magnetization. Such materials are called 'exchange-spring' or 'exchange hardened' magnets. The anisotropy of the hard phase stabilises the soft phase against demagnetization. An exchange coupled hard/soft magnetic multilayer is an obvious example of such an exchange spring magnet.

Since Skomski and Coey's work, exchange hardened magnets have been extensively studied both theoretically and experimentally (for example by Fullerton *et al.* [10, 30]). The latter have studied strongly exchange coupled Sm-Co films and Sm-Co$(1\bar{1}00)$/TM superlattices, grown by dc magnetron sputtering, in which the coupling between the different layers is ferromagnetic. The experimental results for both Sm-Co films and Sm-Co/Fe bilayers agreed quantitatively with simulation [30]. They concluded that exchange spring behaviour could be understood in terms of the intrinsic parameters of the hard and soft magnetic phases. They also measured the energy products of a series of Sm-Co/Co bilayers [10]. Though the highest energy product measured was only ~14 MGOe, the results clearly indicated the advantage of the exchange spring mechanism. The reversal properties of such samples have also been studied using recoil hysteresis loops [31]. Recoil loops are measured by repeatedly removing and reapplying a demagnetizing field to a sample, increasing the demagnetizing field with each successive application. When the magnetizing and demagnetizing curves do not overlap, the recoil loop is said to be open. Open recoil loops are often attributed to a breakdown of the exchange coupling. Hence, the area enclosed by the loop is associated with the decoupled volume in the soft phase [31]. However, element specific recoil loops have been obtained recently by Choi *et al.* [32,

33], using X-ray Resonant Magnetic Scattering (XRMS) magnetometry complemented by micromagnetic simulation. These results show that the open recoil loops in Sm-Co/Fe bilayers are linked to variations in the hard layer anisotropy.

A great deal of research has also been performed on MBE grown single crystal $REFe_2$ Laves phase materials, similar to those discussed in later chapters. As well as being excellent model systems with which to study exchange springs, these materials display useful features such as exchange spring GMR [12]. Magnetic measurements of $DyFe_2/YFe_2$ multilayers showed that features such as the coercivity could be engineered by adjusting the thicknesses of the component layers [2]. In particular, the antiferromagnetic coupling between the hard and soft phases can lead to negative coercivity in multilayers with thick soft layers [34]. Initially, the magnetically hard $DyFe_2$ layers were thought to dominate the magnetization processes in the multilayers. However, X-ray Magnetic Circular Dichroism (XMCD) measurements performed by Dumesnil *et al.* (2004) [35] revealed surprising behaviour at high temperatures. In multilayers with sufficiently thick soft layers, magnetic reversal begins in the hard layers. Figure 2.2 shows the results of bulk magnetometry and XMCD obtained for a [$DyFe_2$(50 Å)/YFe_2(200 Å)] superlattice at both 100 K and 200 K. At 100K there is one switch of the hard layers, accompanied by the formation of exchange springs in the soft layers. The coercivity at 100 K is negative. At 200 K, magnetic reversal begins in the $DyFe_2$ layers. There are three irreversible switches in the hysteresis curve and the coercivity is positive.

The spin configurations occurring at high temperatures in $DyFe_2/YFe_2$ multilayers with thick soft layers were studied using Polarized Neutron Reflectometry (PNR) and micromagnetic simulation [36]. At low fields, the YFe_2 magnetization points in the magnetic field direction. The $DyFe_2$ magnetization is forced to point opposite the applied field. At high fields, the hard and soft layer magnetizations point -33±12°and 42±10° from the field, respectively. Unusual high temperature spin configurations also occur in $ErFe_2/YFe_2$ multilayers, which order magnetically out of plane. The results of bulk magnetometry and micromagnetic modelling of $ErFe_2/YFe_2$ multilayers are described in chapter 4 of this thesis.

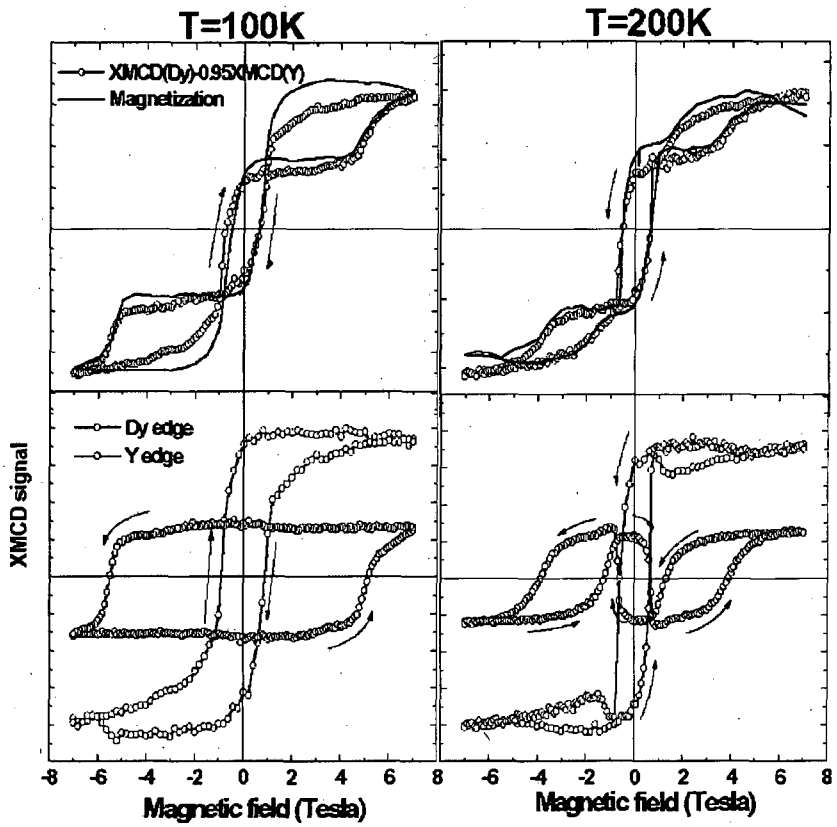

Figure 2.2. Measurements of XMCD and magnetization obtained for a [$DyFe_2$(50 Å)/YFe_2(200 Å)] superlattice. The top panels show macroscopic magnetization measurements (solid curves) superimposed on a linear combination of the XMCD loops measured at the Y and Dy edges. The bottom panels show the XMCD loops at the Y edge (light circles) and the Dy edge (dark circles). After Dumesnil *et al.* (2004).

The magnetic reversal processes of TbFeCo/[Co/Pd] multilayers have been studied by Watson *et al.* [37] using PNR and magnetometry. These multilayers show strong perpendicular anisotropy and could form part of a prototype data storage media. An interfacial domain wall forms in these materials at intermediate applied field, due to competition between the Zeeman energy and exchange energy. A useful feature of PNR is that it allows characterization of the depth dependent magnetization of a sample. Watson *et al.* [37] showed that the shape and location of the interfacial domain wall varied systematically with the applied field and the exchange stiffness of the Co-Co interaction in the Co/Pd layers. The Co-Co interaction depends on the thickness of the Pd interlayers. These techniques can be used to characterize the depth dependent magnetic structure of data storage media with perpendicular magnetic anisotropy.

Exchange spring coupled films are also of interest in applications such as domain wall junctions and exchange biasing [10]. Domain wall junctions consist of two soft layers separated by a thin hard layer [38]. These are used to study the behaviour of domain walls interacting with the potential barrier created by the hard layer. Exchange biasing is a property of many antiferromagnetic/ferromagnetic (AF/FM) bilayer systems, which occurs when the material is cooled through the Neel temperature T_N of the AF layer [39]. The hysteresis loop of such a material is shifted along the field axis by the exchange field H_E. The coercivity, H_c, is different in increasing fields than for decreasing fields. This is shown schematically in Fig. 2.3. However, exchange bias systems are still poorly understood. They are usually analyzed in terms of the exchange anisotropy at the AF/FM interface. This exchange anisotropy stabilizes the magnetic moment in the FM layer in one particular direction (see Fig 2.3). This is unlike uniaxial anisotropy, where there are two minimum energy directions for the magnetic moment 180° apart. Exchange bias systems are important in applications involving permanent magnets, magnetoresistive sensors and magnetic recording media, among others (see the review of Nogues and Schuller [39] and references therein).

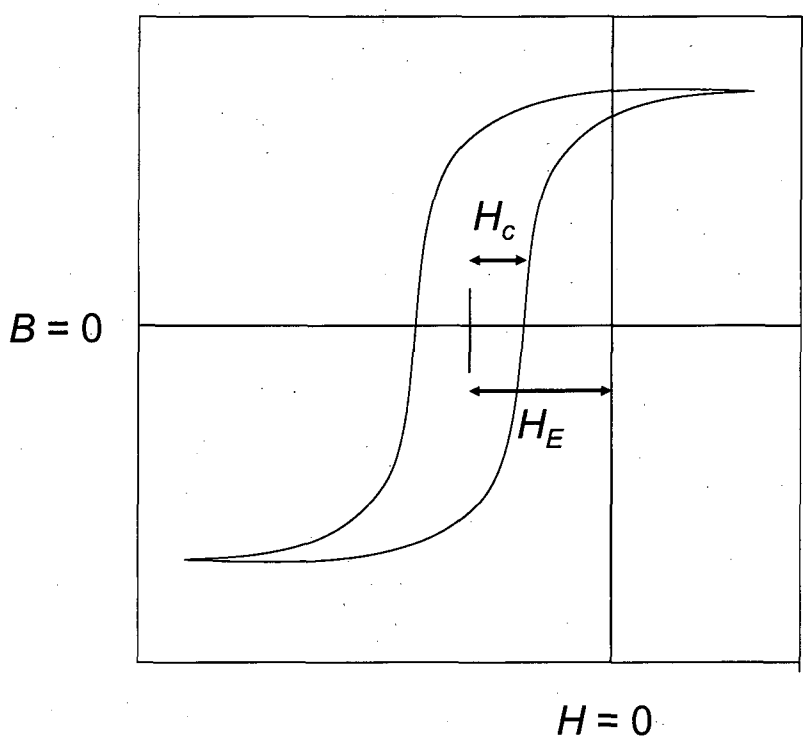

Figure 2.3. Schematic of a hysteresis loop showing significant exchange bias. The loop is shifted along the field axis by the exchange field H_E.

Stronger permanent magnets will always find applications in magnetic MEMS, or magMEMS [7]. Some 'proof of concept' devices already developed include pressure sensors and hearing implants [17]. Many of the magnetic interactions that are important in applications benefit greatly from scale reduction [40]. A comparison of various permanent magnets has been given, for example, by Chin [20]. For use in magMEMS, a permanent magnet film must display reasonable magnetic properties, compatibility with MEMS processing (electroplating, sputtering, dry or wet etching, etc), and environmental stability. Rare earth based films have the best magnetic properties, but are not always the best choice for magMEMS because of their high corrosion rate. The most preferable alternatives suggested by Chin are Pt-Fe or Pt-Co magnets, or hybrid magnet thick films made from a magnetic powder and photo-etchable resin.

Rare earth based materials are used extensively for applications which involve magnetostriction [41-43]. It has been known since the early 1970's that rare earth-iron intermetallics exhibit giant magnetostriction. Among these compounds, the optimised binary intermetallic $Tb_{0.3}Dy_{0.7}Fe_{1.9}$ (Terfenol-D) provides the best value for large magneto-elasticity (~1% [41]) in low fields, at room temperature [43]. Terfenol-D has found many applications, for example high power transducers for acoustics and mechanical functions (see [43] and references therein).

There is a great deal of current research into new materials for magnetic data storage. Large amounts of data necessitate an ever increasing areal density of hard disk drives. The change from longitudinal recording to perpendicular recording is one example of recent progress in this area [44], but other innovations will be required if storage density is to reach $1Tb/in^2$ and beyond. The traditional hard disk medium consists of magnetic 'bits', composed of grains. Reducing the number of grains in a bit would decrease the signal to noise ratio (SNR), so scaling of the traditional hard disk requires a reduction in grain size. However, reducing the volume V of a grain in turn lowers its anisotropy energy $K_U V$, where K_U is the magnetocrystalline anisotropy. This scaling down is subject to the so-called superparamagnetic limit [45, 46], where the magnetic energy becomes comparable to thermal energies, $K_B T$. If the magnetic energy of the grains is reduced too far, thermal effects can switch the magnetization of the grains and data will be lost. Increasing K_U is in turn limited by the need to be able to write

data to the medium. Modern write heads provide a field of up to 1.4 T [8]. The main criteria that data storage must satisfy are high density, writability, stability and good SNR. It is difficult to satisfy all of these criteria together.

The exchange spring mechanism can be used to make a medium easier to write to. They allow the use of materials with higher magnetic anisotropy and thus greater thermal stability. Thiele *et al.* [47] have suggested exchange spring media for thermally assisted magnetic recording (TAR), in FeRh/FePt bilayers. FeRh is AF at room temperature, but FM above a certain critical temperature, which they denote T_N. In order to write to the material, it is heated above T_N so that FeRh becomes FM. In this state the FeRh layer aids the switching of the FePt layer via an exchange spring mechanism. After writing to the material the heat is removed and the FeRh layer cools below T_N, becoming AF again. The thermal stability of the material is determined primarily by the high anisotropy FePt layer. Another method, proposed by Suess *et al.* [8, 21] is to embed a soft (low anisotropy) magnetic layer between two hard (high anisotropy) magnetic layers. Application of a write field nucleates a domain in the soft layer that facilitates switching of the hard layer magnetization. The structure has a much lower coercivity than a single hard layer, allowing the use of materials with higher anisotropy than normal. Another possibility is to use tilted media. Tilted media is similar to perpendicular media, but the grains have anisotropy directions at some angle α, ideally 45°, to the write field H_w. A schematic of the easy axis direction in tilted media is shown in Fig 2.4 (a). This configuration allows the use of higher anisotropy materials. A major source of noise in recording media is the switching field distribution (SFD) caused by the easy axis distribution of the grains (EAD). According to the Stoner Wolfarth model [48], the sensitivity of the switching field to α is a maximum when α is close to 0 or 90°. When α is close to 45° the sensitivity of H_w to α is a minimum. This minimizes the SFD, thereby improving SNR. Compared with perpendicular media, tilted media allow faster switching rates, better SNR and better thermal stability [49, 50].

Victora and Shen [22] have proposed a composite medium consisting of hard and soft regions within each grain as an alternative to tilted media. These authors concluded that composite media performed much like tilted media, while being more easily fabricated. A schematic representation of a grain is shown in Fig 2.4 (b). The grain is

made up of a soft region of volume V_1 and anisotropy K_1 exchange coupled to a hard region of volume V_2 and anisotropy K_2. Composite media utilize the exchange spring mechanism to increase the ratio of the stabilizing energy barrier to the switching field.

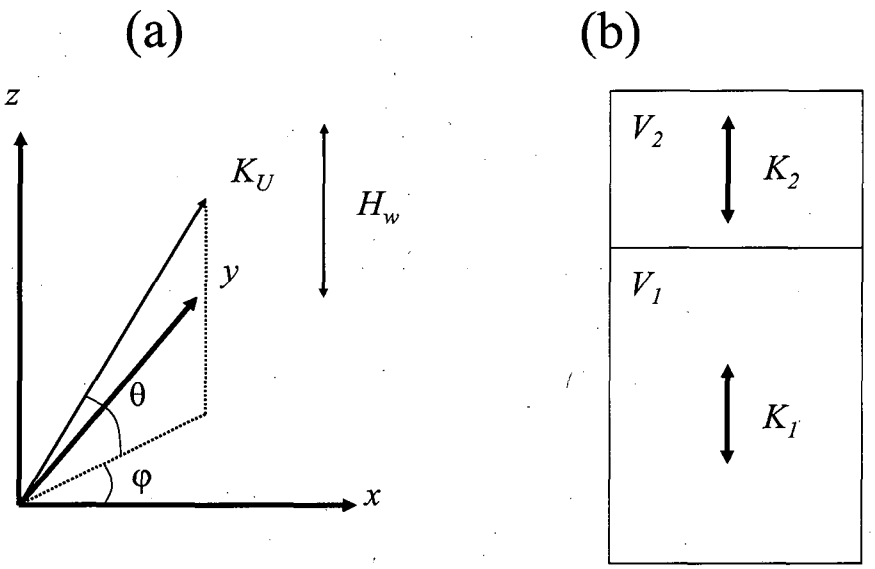

Figure 2.4. Schematic representation of the easy axis direction for tilted media (a) and a possible grain configuration for composite media (b).

In section 2.3 of this thesis, exchange springs in $ErFe_2/YFe_2$ multilayers are discussed. However, first a summary is given of the basic interactions that characterize the $REFe_2/YFe_2$ multilayers and which lead to the formation of magnetic exchange springs.

2.2. Magnetism of $REFe_2$ intermetallics

The structure of $REFe_2$ Laves phase intermetallics is illustrated in Fig 2.5 (a,b), looking along the [110] (a) and [111] (b) directions, respectively. These are the two growth directions for the MBE films detailed in this thesis. The large, green (small, red) balls represent the RE (Fe) atoms. Each unit cell contains 8 RE and 16 Fe atoms. The lattice parameters of the different compounds considered in this work are given in table 2.1, after Mougin *et al.* [51].

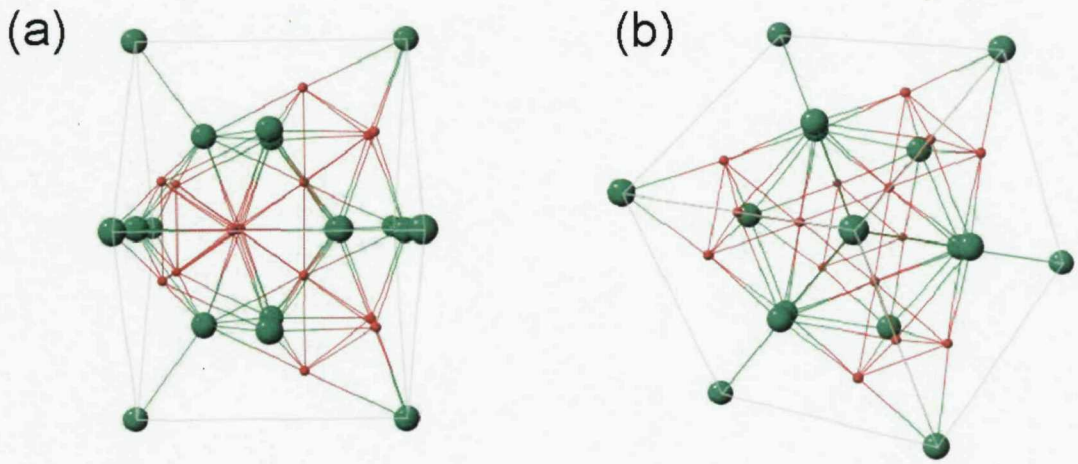

Figure 2.5. The structure of the Laves Phase intermetallics shown looking along the [110] (a) and [111] (b) directions

Compound	Lattice parameter (Å)
$DyFe_2$	7.324
$ErFe_2$	7.28
YFe_2	7.362

(2.1)

Table 2.1. Room temperature lattice parameters for the different compounds considered in this work. After Mougin *et al.* (1999).

The $REFe_2$ (RE is a heavy rare-earth) Laves phase compounds are characterized by; (i) Strong (600 K) ferromagnetic Fe-Fe exchange; (ii) strong antiferromagnetic RE-Fe exchange; (iii) strong anisotropy at the rare-earth sites, which dictates the direction of the easy axis of the compound. Ferromagnetic RE-RE exchange also exists, but this is much weaker than the Fe-Fe and RE-Fe exchange interactions.

The Fe-Fe exchange interaction is strong and long range. In samples of pure Fe it can be as high as 1000 K, while in the $REFe_2$ intermetallics it is typically around 600 K. The 3*d* electrons responsible for magnetism in Fe have quite localized wavefunctions, but the spatial extent of these wavefunctions is only about half an interatomic

distance. The idea that direct exchange interactions could account for the ferromagnetism of the magnetic metals was disproved in 1960 by Stuart and Marshall [52]. They showed that direct exchange interactions were far too weak to explain the experimentally determined Curie temperatures. In a series of papers circa 1950, Zener [53-56] proposed a mechanism involving both direct and indirect exchange. In this model, the localised *d* electrons polarized the conduction electrons, which then aligned the atomic moments. Zener assumed ferromagnetic *s-d* and antiferromagnetic *d-d* exchange and predicted that ferromagnetism would occur for systems in which the neighbouring incomplete *d* shells were sufficiently far apart for the indirect *s-d* exchange to dominate the direct *d-d* exchange. However, it was later noticed [57-59] that the *s-d* interaction would result in an oscillatory spatial polarization of the conduction electrons, falling off rapidly with distance from the localised moment. This new theory of indirect exchange was developed independently by Ruderman and Kittel, Kasuya and Yosida, and is often referred to as the RKKY model. After direct exchange was ruled out as causing the ferromagnetism of Fe, RKKY exchange became the favoured explanation. However, in the 1960's and 1970's, Stearns [60-64] showed, with Mössbauer and NMR measurements, that the *s* electron polarization was negative at the first two neighbour shells. The polarization of an *s* electron at the distance of the nearest neighbour from an Fe atom is in the opposite direction to that of the atom. This means that the exchange between the itinerant *s* electrons and the localised *d* shells tends to align the atomic spins antiferromagnetically. Therefore, *d-s* coupling cannot be responsible for the ferromagnetism of Fe. Stearns [64, 65] proposed that the localised *d* electrons were in fact coupled through a small number of itinerant *d* electrons. This model remains a viable explanation of long range ordering in Fe, but it is still an open question.

As in the case of the Fe-Fe exchange, direct Heisenberg exchange cannot be responsible for long range order in rare-earth materials, because it would require electron hopping between different sites. The 4*f* orbitals responsible for rare-earth magnetism are highly localised (the radius of a 4*f* wavefunction is only about 10% of an atomic spacing). But magnetic ordering in rare-earth metals can be understood in terms of the RKKY model. The moment at one $4f^n$ site polarizes the 6*s* conduction electrons there. These weakly polarized conduction electrons have spatially extended

wavefunctions, so they can transfer the spin information to other sites. This type of indirect exchange is weaker than the exchange coupling in $3d$ transition metals. The oscillatory spatial polarization of the conduction electrons mentioned above can give rise to ferromagnetism, antiferromagnetism or helimagnetism in rare-earths.

The coupling between rare-earth and transition metal moments is ferromagnetic for light rare-earths and antiferromagnetic for heavy rare-earths (such as Er or Dy). However, the spin-spin coupling between rare-earths and transition metals is always antiferromagnetic. This is illustrated schematically in Fig 2.6. (a) Except for Gd, the rare-earth species have $L \geq S$. For the first half of the $4f$ series ($4f$ shell less than half full) Hund's third rule requires $\boldsymbol{L}$ and $\boldsymbol{S}$ to be antiparallel, leading a reduction in the net effective moment given by $g\mu_B[J(J+1)]^{1/2}$. So for the light rare-earths the net moment is reduced. For the heavy rare-earths $\boldsymbol{L}$ and $\boldsymbol{S}$ combine additively, leading to an increase in the net effective moment. As μ_B is negative and $L \geq S$, the net moment is antiparallel to $\boldsymbol{L}$ for light rare-earths, and antiparallel to both $\boldsymbol{L}$ and $\boldsymbol{S}$ for heavy rare-earths.

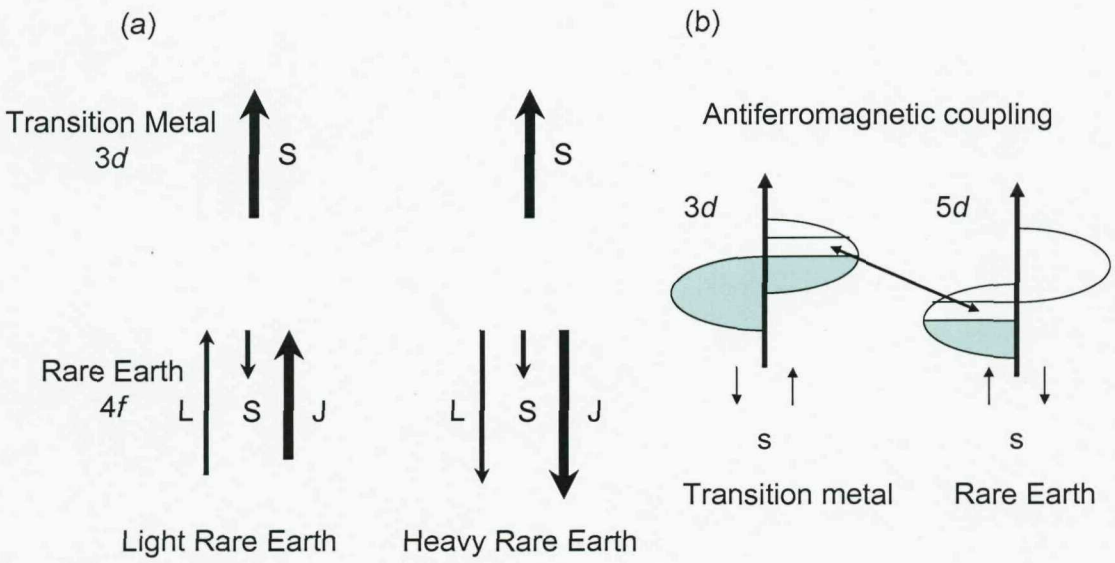

Figure 2.6. Schematic representation of the exchange coupling between Rare Earth and Transition Metal moments.

One explanation for the antiferromagnetic coupling between rare earth and transition metal spins has been given by Campbell [66]. The explanation focuses on the $5d^2$ rare earth conduction electrons. These electrons always have spin parallel to the $4f$

electrons due to ferromagnetic 4*f*-5*d* coupling at the rare earth site. The $5d^2$ rare earth conduction electrons interact with the $3d^n$ electrons of the transition metal. As there are only majority spin electrons in the 5*d* orbitals and only minority spin holes in the 3*d* transition metal orbitals, the exchange between these two sets of *d* states is always antiferromagnetic. This is shown schematically in Fig 2.6 (b). The $REFe_2$ intermetallic compounds most often referred to in this thesis are $ErFe_2$ and $DyFe_2$. Both of these exhibit antiferromagnetic coupling between the rare earth and Fe moments.

In a $REFe_2$ intermetallic compound, the direction of easy magnetization is dictated by the strong magnetocrystalline anisotropy at the RE sites. The Callen-Callen model of magnetic anisotropy [67] had for years been successful in interpreting many RE compounds. However, it proved insufficient to describe the $REFe_2$ compounds. Given the phenomenological constants K_1 and K_2 only major cubic symmetry axes [001], [101] and [111] are allowed directions of easy magnetization. However, work done by Atzmony and Dariel [68] in the 1970's showed that certain alloys (e.g. $Tb_xDy_{1-x}Fe_2$) had non major cubic symmetry axes of easy magnetization. This led them to introduce a third phenomenological parameter, K_3. Such a term had been seen before in measurements on a single crystal of nickel [69], but its effects were much smaller. Atzmony and Dariel found other surprising results. For example, their calculations predicted a change of sign of K_1 (K_2) in $HoFe_2$ ($DyFe_2$) as the temperature increased. The change of sign occurs rapidly, over a temperature range of ~20 K. However, the Callen and Callen model of anisotropy predicts that the anisotropy parameters should decrease monotonically with increasing temperature. Later, by extending the Callen-Callen model to second order perturbation theory, Martin *et al.* [70] were able to explain both the unexpected changes of sign of K_1 and K_2 in $HoFe_2$ and $DyFe_2$, respectively, and the origin and behaviour of the K_3 term witnessed by Atzmony and Dariel.

In the case of MBE grown Laves phase compounds, the shear strain induced during crystal growth [51, 71] is significant. The contribution from the strain modifies the easy axes of the MBE grown Laves phase materials with respect to those of the bulk materials. This contribution (second rank) falls off much more slowly with temperature than the fourth, sixth etc, magnetocrystalline anisotropy terms, leading to

a temperature dependence of the easy axis in some cases [71]. For example, the easy axis in $DyFe_2$ is [001] at low temperatures, as in the bulk. However, as the temperature is increased, the easy axis rotates towards the $[1\bar{1}0]$ direction. Vector magnetometry work by Zhukov *et al.* [72] has shown that, at room temperature, the easy axis of (110) MBE grown $DyFe_2$ is about 15° out of plane, above the $[1\bar{1}0]$ axis. The magnetocrystalline easy axes in (110) $ErFe_2$ films and multilayers are the <111> body diagonals. However, the strain term favours the out of plane [111] or $[11\bar{1}]$ axes. As the temperature is increased, the strain begins to dominate the magnetocrystalline anisotropy, moving the easy axis towards the [110] growth direction. In the case of (111) $ErFe_2$ films and multilayers, both the magnetocrystalline and strain anisotropy favour the [111] growth axis [73]. These materials will be discussed further in chapter 4.

The magnetocrystalline anisotropy of YFe_2 is very small. The material is magnetically soft. In the multilayers discussed in this thesis, the YFe_2 layers are strongly exchange coupled to the hard layers. The combination of hard and soft layers gives rise to the possibility of magnetic exchange springs, discussed below.

2.3. Exchange springs in $REFe_2$ multilayers

The magnetic behaviour of a thin film, consisting of a very soft magnetic layer in close molecular contact with a very hard magnetic layer, was first considered by Goto *et al.* [74]. These authors considered a bilayer with FM coupling between the hard and soft materials. The exchange coupling between the hard and soft layers tends to align spins parallel at the interfaces. They found that the onset of exchange springs occurred at a critical bending field B_B. At this field, which is insufficient to switch the hard layer magnetization, the local magnetization in the soft layer becomes dependent on the depth along the thickness of the film. They also found that $B_B \propto 1/d^2$, where d is the thickness of the soft layer. Fig 2.7 shows a schematic representation of the magnetization configuration of a bilayer exchange spring (a), along with the configuration for the symmetric (multilayer) exchange spring (b) described below. A bilayer exchange spring is pinned at one interface only. The spins in such an exchange

spring make angles between 0 and φ, where φ can be 180°. The shorthand for such a spring is (0- φ). A multilayer exchange spring is pinned at both interfaces. The result is a symmetric exchange spring, often denoted by (0-φ-0).

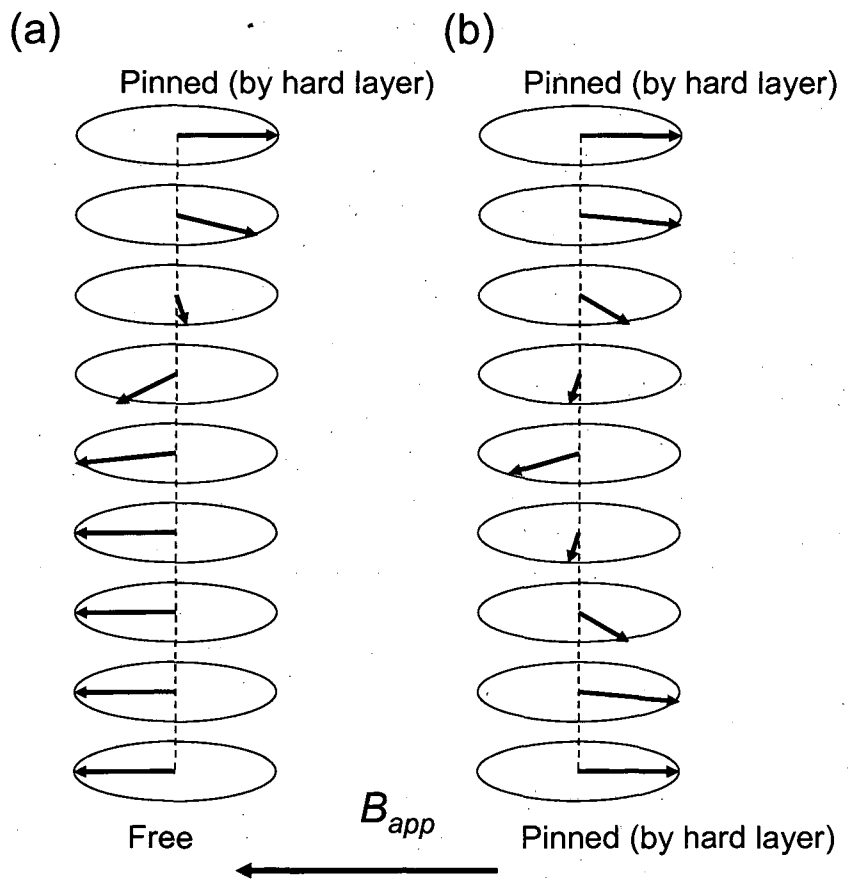

Figure 2.7. Schematic representation of exchange springs in bilayers (a) and multilayers (b). The black arrows represent the magnetic moments in the soft layer.

More recently, Bowden *et al.* [75] considered discrete exchange springs in magnetic multilayers. They used numerical methods to calculate the explicit form of exchange springs. In their notation, the energy of the exchange spring E is given by

$$E = \sum_{n} \varepsilon(n) \tag{2.2}$$

where

$$\varepsilon(n) = +\mu_{Fe} B_{APP} \cos\theta_n - \frac{1}{2}\mu_{Fe} B_{EX} \left[\cos(\theta_n - \theta_{n-1}) + \cos(\theta_{n+1} - \theta_n)\right] \tag{2.3}$$

In equation (2.3) μ_{Fe} is the moment of an Fe spin, B_{APP} is the applied field, shown in Fig 2.7, B_{EX} is the exchange field and θ_n denotes the angle of the n^{th} spin. Also note that in equation (2.3) only nearest neighbour interactions are considered and the anisotropy associated with the soft layers has been ignored. The first term in equation (2.3) corresponds to the Zeeman energy of an Fe moment in the applied field. The second term corresponds to the exchange energy associated with the angle between nearest neighbour spins. The first term, Zeeman energy, is minimized when θ_n is 180°, i.e., the spin points in the applied field direction. However, the exchange energy is minimized when the angle between nearest neighbour spins is small.

A full derivation of the form of exchange springs can be found in Bowden *et al.* [75]. The result of the competition between exchange and Zeeman energy is that, above B_B, the Fe spins rotate gradually throughout the soft layer as shown in Fig 2.7. The authors found that, for a multilayer spring

$$B_B / B_{EX} = (\pi / N)^2 \tag{2.4}$$

where N is the number of monolayers of Fe in the soft layer. In the case of a bilayer spring

$$B_B / B_{EX} = (\pi / 2N)^2 \tag{2.5}$$

Note that, for a given N, the bending field is always lower for bilayer springs than multilayer springs. This makes intuitive sense as the bilayer spring is only pinned at one interface. The $1/N^2$ dependence agrees with the result of Goto *et al.* [74].

In $ErFe_2/YFe_2$ multilayers, vertical exchange springs form in the soft YFe_2 layers because of competition between Zeeman energy and exchange energy. In zero field and in the absence of domains, the multilayer is a man-made ferrimagnet. The hard layer magnetization points along an out of plane <111> axis. The Fe in the hard layers is antiparallel to that of Er because of the Er-Fe AF coupling, and the strong Fe-Fe exchange aligns the Fe moments throughout the sample opposite the hard layer magnetization. This situation is shown in Fig 2.8 (a). Application of a magnetic field

$B_{app} > B_B$ along the easy axis causes the Fe moments to rotate throughout the soft layer, as shown in Fig 2.8 (b).

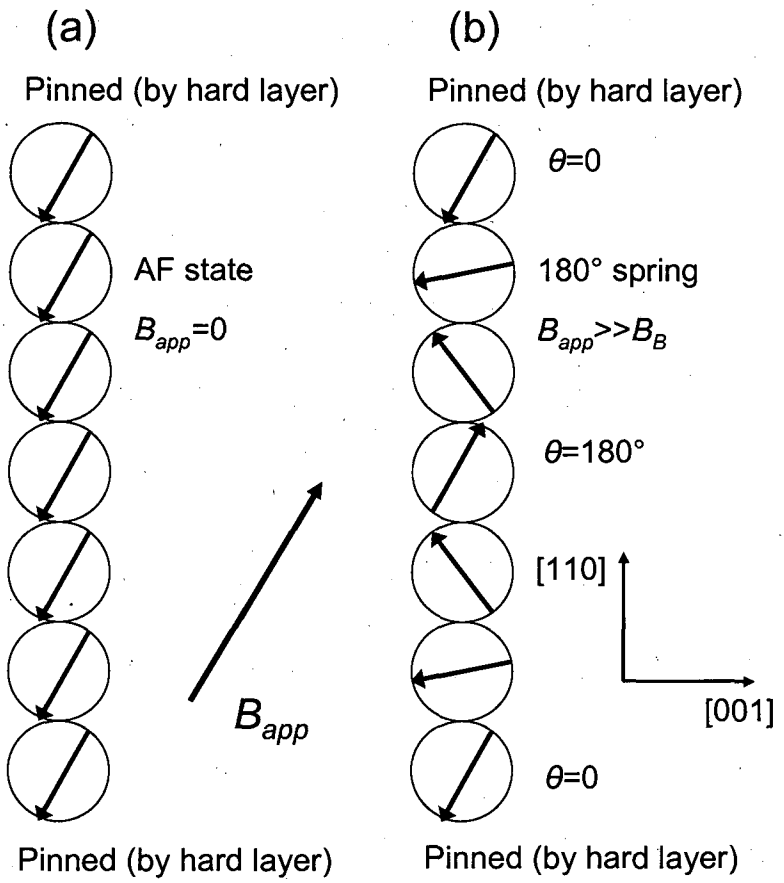

Figure 2.8. Spin configurations in the YFe_2 layers of a $ErFe_2/YFe_2$ multilayer at zero field (a) and at $B_{app} > B_B$ (b).

Exchange springs in $ErFe_2/YFe_2$ multilayers have a marked effect on their hysteresis loop. An example, the hysteresis loop of [$ErFe_2$(50 Å)/YFe_2(150 Å)] × 20 at a temperature of 70 K, is shown in Fig 2.9. In this case, the field is applied along the [110] direction. At high fields (point 1 on Fig 2.9) the $ErFe_2$ magnetization points close to the applied field direction and there are tight exchange springs in the soft layers. As the field is reduced, the exchange springs unwind reversibly until, at zero field, the multilayer is in an AF configuration.

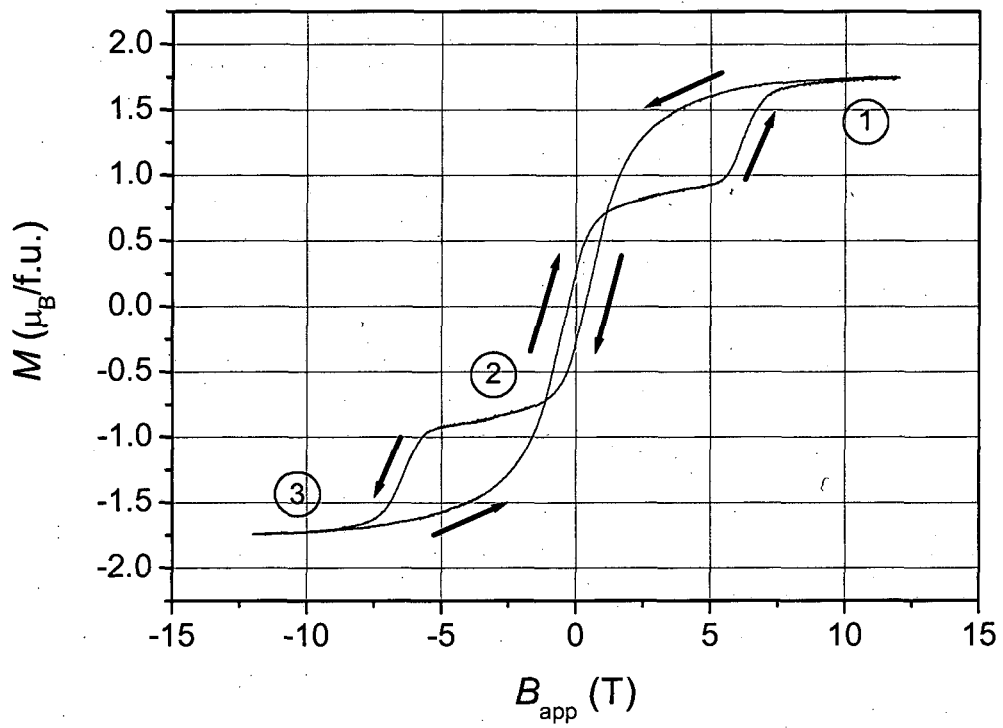

Figure 2.9. Hysteresis loop of [$ErFe_2$(50 Å)/YFe_2(150 Å)] × 20 at 70K. The arrows indicate the direction in which the field is being swept.

One consequence of this unwinding is that the magnetization of an YFe_2 dominated multilayer may reverse before the applied field. In this case, the conventionally defined coercivity of the multilayer is negative [34]. This behaviour is seen in the example shown in Fig 2.9. Note that on reducing the field, the entire magnetization curve between point 1 and point 2 is reversible. When the field reaches a sufficiently high negative value (point 3 on Fig 2.9), the hard layers switch so that the $ErFe_2$ magnetization points close to the new applied field direction. This irreversible transition is accompanied by the formation of exchange springs in the soft layers. The spin configuration of the multilayer at point 3 is the mirror opposite of the spin configuration at point 1. If the field is now increased towards point 1, the magnetization curve once again consists of reversible unwinding of exchange springs until a large positive field is reached. At this point the hard layers switch again and tight exchange springs form in the soft layers. If the field continues to increase, the exchange spring will wind tighter. This behaviour is also reversible. The exchange springs act like domain walls. When they wind tighter, the effective domain wall

width is smaller. This can have important effects on the transport properties of exchange spring multilayers, described below.

2.4 Transport properties of $REFe_2$ films and multilayers

The galvanomagnetic properties of magnetic materials are varied and often complicated. They can also be useful for device applications. One of the best known galvanomagnetic effects is the Hall effect, sometimes called the ordinary Hall effect (OHE). When a magnetic field is applied perpendicular to an electric current in a slab of material, an electric field is set up across the slab, perpendicular to both the magnetic field and the current. It occurs because the Lorentz force on the charge carriers in a magnetic field deflects their velocity at right angles to the current direction. Charge carriers build up on one side of the material, setting up an electric field across the sample. This field opposes the deflection of the charge carriers, so in equilibrium there is no current flow perpendicular to the applied electric field. The OHE is largest in semiconductors where the carrier density is low. The high conductivity in a metal effectively shorts out the Hall voltage. However, magnetic materials can display the anomalous Hall effect (AHE), which can be several orders of magnitude larger than the OHE. This effect is described below. Another well known galvanomagnetic effect is magnetoresistance (MR). An applied magnetic field deflects charge carriers from the current direction. These carriers orbit the applied field and do not contribute to the current until they are scattered. Thus an applied magnetic field increases the resistance of a material. Because a deflection of the charge carriers in either direction away from the current direction increases the resistance, the resistance change must be an even power of the applied field. If the relaxation time is long (the resistivity is low), the effect of the magnetic field on the resistance is large. The magnetoresistance ratio for many ferromagnetic metals obeys

$$\frac{\Delta\rho}{\rho} \propto \left(\frac{B}{\rho}\right)^2 \tag{2.6}$$

Equation (2.6) is known as Kohler's rule [76].

Once again, the situation is more complicated in magnetic materials, where the range of magnetoresistive effects includes anisotropic magnetoresistance (AMR), giant magnetoresistance (GMR) and tunnelling magnetoresistance (TMR), among others. GMR and AHE are the galvanomagnetic effects detailed in this thesis.

Resistivity in metals is caused by scattering of the conduction electrons. At low temperatures the dominant mechanism is scattering from impurities in the regular lattice potential. Phonon scattering is another source of resistance in metals. As the temperature increases, so does the number of phonons in the metal, leading to an increase in the resistance. Another source of resistance is GMR. GMR is one of the most important applications yet realised for spintronics. It was discovered independently by Albert Fert and Peter Grünberg in the 1980's [77, 78], an achievement that has recently earned them the Nobel Prize for physics [79, 80]. GMR is extremely important as it is now used extensively in modern read heads for hard disk drives.

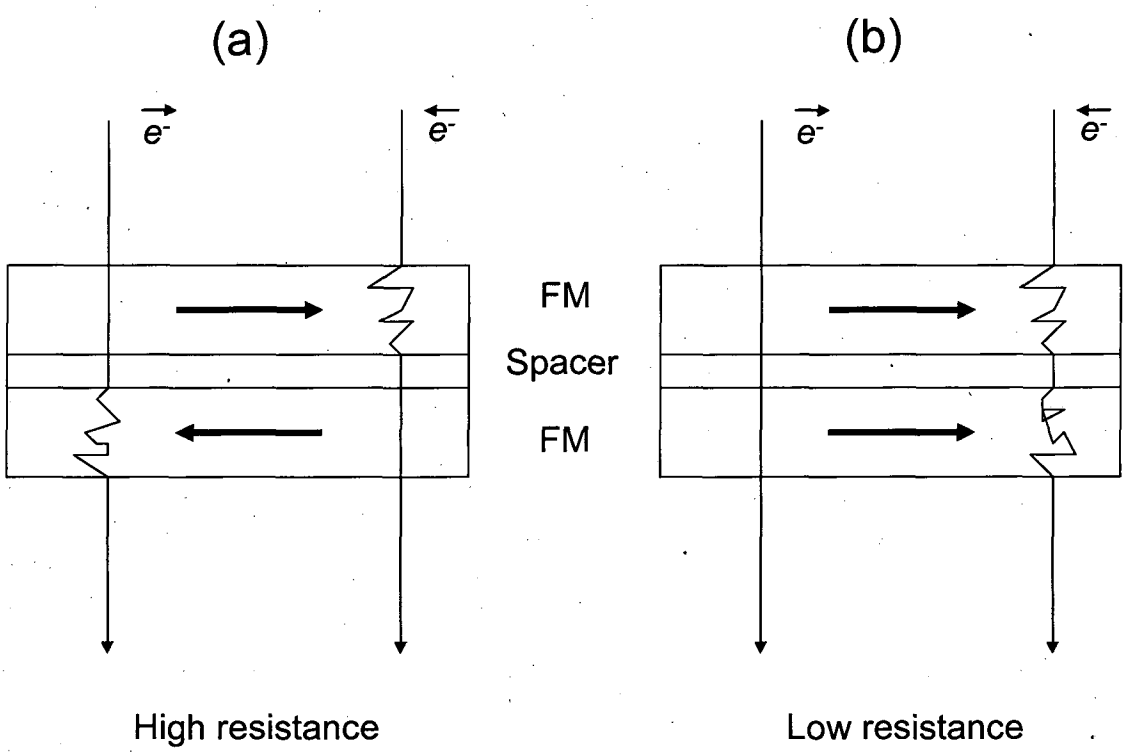

Figure 2.10. The standard GMR structure consists of two FM layers separated by a non magnetic spacer. In the high resistance state (a) the two FM layers have opposite magnetization and in the low resistance state (b) they have parallel magnetization.

The standard GMR arrangement, shown schematically in Fig 2.10 (a,b), consists of two FM layers separated by a non-magnetic spacer layer. The resistance decreases when the magnetization directions of the FM layers are brought into alignment by a magnetic field. The mechanism of GMR is easily understood in terms of a two current model, in which electrons of opposite spin traverse different arms of a parallel resistance network. When the magnetizations of the two FM layers are antiparallel, electrons of both spins encounter significant resistance. However, when the magnetizations of the two FM layers are aligned parallel, electrons with parallel spins pass easily through the structure, while electrons of opposite spin see a large resistance. In this case, the low resistance spin channel effectively shorts the high resistance channel, leading to a dramatic drop in the resistance of the structure. Note that GMR has an even, or symmetric, dependence on the applied field. That is, when the sign of the magnetic field changes, the GMR is unchanged:

$$\frac{\Delta\rho}{\rho_0}(B) = \frac{\Delta\rho}{\rho_0}(-B) \tag{2.7}$$

where B is the applied field, ρ_0 is the resistivity of the material (when B is zero), and $\Delta\rho = \rho - \rho_0$ is the change in resistivity resulting from the application of B. Also note that GMR is often expressed as a percentage

$$\text{GMR}(\%) = \frac{\rho - \rho_0}{\rho_0} \times 100 \tag{2.8}$$

In the 1990's it was argued [81, 82] that domain walls in ferromagnets should give rise to GMR-like magnetoresistance. The mechanism suggested by Viret *et al.* [82] rested on the inability of an electron spin to track the reorientation of magnetization within a domain wall. A more complete quantum mechanical treatment was given by Levy and Zhang [83]. In this model, however, the inability of the electron spin to track the reorientation of magnetization in a domain wall is not a source of scattering. The electron spin mis-tracking mixes channels of opposite spin, resulting in spin dependent scattering from impurity centres. This model has been employed by Gordeev *et al.* [12] to estimate the GMR due to exchange springs in $DyFe_2/YFe_2$

multilayers. According to these authors, the exchange springs act like domain walls with an effective thickness equal to the thickness required for the Fe moments to rotate by 180°. As the applied field is increased, the exchange springs wind tighter, so their effective domain wall thickness decreases. They used a simple model based on parallel resistances,

$$\frac{\Delta R}{R} = \left[\left(\frac{t_Y}{\rho_Y} + \frac{t_D}{\rho_D} \right) \left(\frac{2\delta_w}{\rho_Y} - \frac{2\delta_w}{\rho_w} \right)^{-1} - 1 \right]^{-1} \tag{2.9}$$

where ρ_w and δ_w are, respectively, the resistivity and effective thickness of the exchange spring; ρ_Y, ρ_D and t_Y, t_D, are the resistivities and thicknesses of the YFe_2 and $DyFe_2$ layers, respectively. According to Levy and Zhang [83], the resistivity in the domain wall region in the current in plane (CIP) geometry can be written,

$$\rho_w = \rho_0 \left[1 + \frac{\alpha}{\delta_w^2} \right] \tag{2.10}$$

where $\alpha = \frac{1}{5}\left(\pi\hbar^2 k_F / 4mJ\right)^2 \left(\rho_0^{\uparrow} - \rho_0^{\downarrow}\right)^2 / \left(\rho_0^{\uparrow}\rho_0^{\downarrow}\right)$, $\rho_0^{\uparrow}$ and $\rho_0^{\downarrow}$ are the resistivities of the spin up and spin down current channels, respectively; $\rho_0 = \left[1/\rho_0^{\uparrow} + 1/\rho_0^{\downarrow}\right]^{-1}$ is the resistivity without domain walls; J is the magnetic exchange constant; k_F is the Fermi wave vector and m is the effective mass of the electron. In the model of Levy and Zhang [83], δ_w is the domain wall thickness, corresponding to a rotation of the local magnetization through 180°. Equation (2.10) shows that the resistivity in the domain wall region increases as δ_w decreases. The estimates of δ_w used by Gordeev *et al.* [12] were obtained from magnetic modelling, and subsequently doubling the thickness required for the Fe moments to rotate through 90°. The magnitude of the GMR in these structures was found to be as high as 32% at 23 T.

In Chapter 6.2 of this thesis, the AHE in $ErFe_2/YFe_2$ multilayers is presented and discussed. Since its discovery in 1881 [84, 85] the Hall effect has been a well studied

and highly useful phenomenon. By way of contrast, the AHE is still poorly understood over a century since its discovery. In recent years there has been renewed interest in the AHE, due in part to its potential application in field sensors and memory devices [86, 87] and its use in characterising thin films with a perpendicular component of magnetization [88, 89]. This revival has resulted in a great deal of theoretical and experimental research. On the theoretical side, the work of Karplus and Luttinger [90] has recently been interpreted by several authors in terms of the Berry curvature of occupied Bloch states (see references [91-93] and references therein). Experimentally [94], data have been interpreted within the theoretical framework referenced above, but there have been alternative interpretations, for example the modified skew scattering model of Gerber *et al* [95].

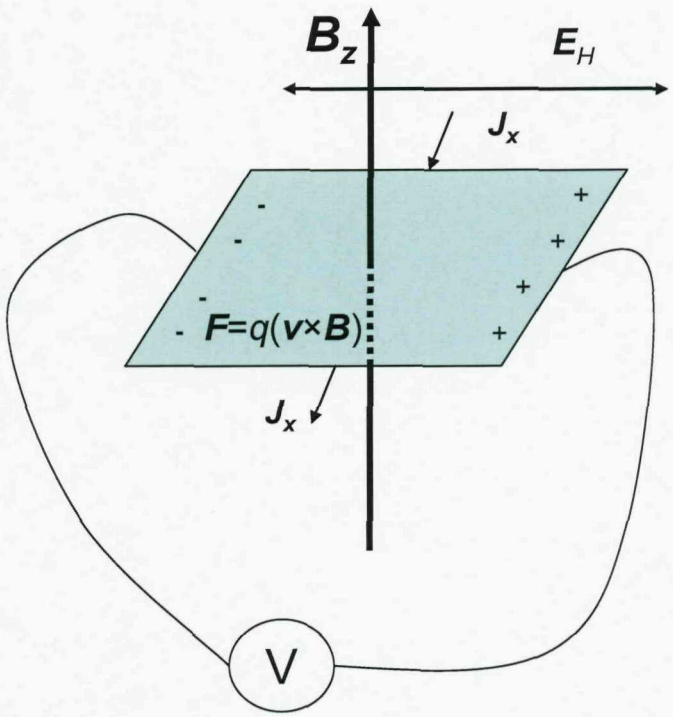

Figure 2.11. Standard geometry of Hall effect measurements

The standard geometry used to measure the Hall effect is shown in Fig. 2.11. A magnetic field B_z applied to a conductor in which the current density is J_x generates a transverse electric field known as the Hall field E_H. This leads to the definition of the ordinary Hall coefficient

$$E_H = R_0 J B_z \tag{2.11}$$

and the Hall resistivity

$$\rho_{xy} = \frac{E_H}{J_x} \tag{2.12}$$

Note that the Hall field has odd, or antisymmetric, dependence on the applied magnetic field direction. That is, when the sign of the magnetic field changes, the sign of the Hall field also changes:

$$E_H(B_z) = -E_H(-B_z) \tag{2.13}$$

The sign of the Hall field also depends on the nature of the charge carriers. Fig 2.11 shows the situation for electrons. For holes, the Hall voltage will have the opposite polarity.

In ferromagnetic metals the Hall resistivity ρ_{xy} takes the form [96-98]

$$\rho_{xy} = R_0 B + \mu_0 R_s M \tag{2.14}$$

where the first term represents the ordinary Hall effect, with R_0 the ordinary Hall coefficient. The second term is an anomalous component, proportional to the spontaneous Hall coefficient R_s and the perpendicular magnetization M. R_s itself takes the form:

$$R_s = a\rho_{xx} + b\rho_{xx}^2 \tag{2.15}$$

where ρ_{xx} is the standard resistivity of the metal and a and b are constants. Measurement of the standard resistivity thus gives information about the mechanism of the AHE in a metal. The first term in equation 2.15 is normally attributed to a mechanism known as skew scattering and the second term to another mechanism, the

quantum mechanical side jump proposed by Berger in the 1970's [99]. Experimentally, AHE data are often fitted in terms of a single power law [94, 95]

$$\rho_{AH} \propto \rho_{xx}^{n} \tag{2.16}$$

where ρ_{AH} is the anomalous Hall resistivity, $n=1$ corresponds to skew scattering, $n=2$ corresponds to the side jump and $1 \leq n \leq 2$ is accepted as a superposition of these two mechanisms. However, the experimental data do not always fit the theoretical expectations. For instance, n as high as 3.7 has been reported for granular Co-Ag films [100]. As mentioned earlier, however, this is not the only interpretation of these terms [95]. Many different scattering mechanisms have been proposed [96].

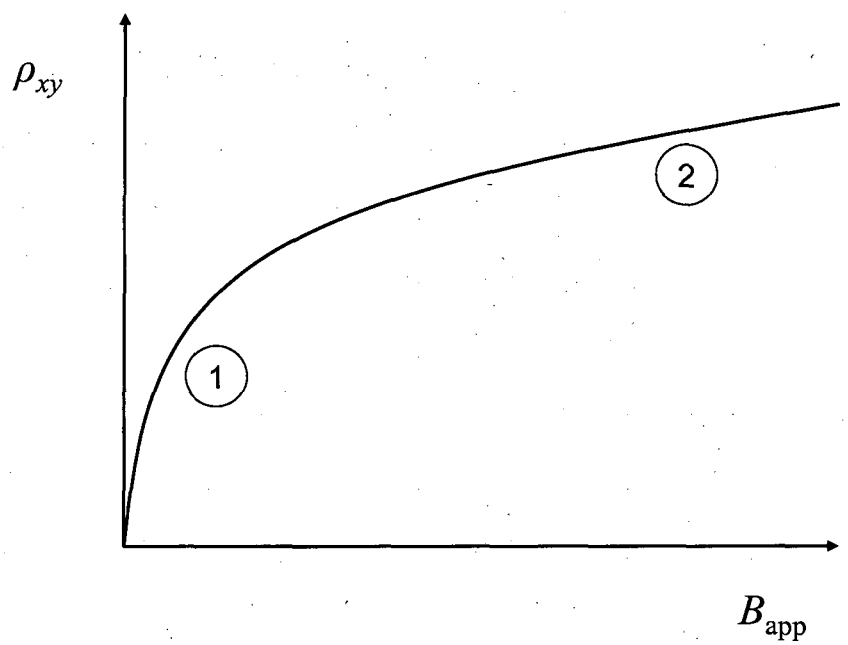

Figure 2.12. Hall resistivity ρ_{xy} for a hypothetical metal with appreciable magnetization and negligible coercivity.

A schematic representation of the Hall resistivity in a magnetic material as a function of magnetic field is shown in Fig 2.12. A single domain of a ferromagnetic material in zero field will have a spontaneous Hall resistivity of $\mu_0 R_s M$. The sign of the corresponding Hall voltage depends on the orientation of the magnetization in the domain, so for a sufficiently large number of randomly oriented domains the

transverse Hall voltage will be zero. An applied magnetic field progressively aligns the magnetic domains along the field direction, leading to a large initial slope of the Hall voltage (point 1 on Fig 2.12). At magnetic saturation the spontaneous Hall resistivity is $\mu_0 R_s M_s$. Above saturation (point 2 on Fig 2.12) the slope of the ρ_{xy} vs B_{app} curve is given by [96]

$$\frac{\partial \rho_{xy}}{\partial B_{app}} = R_0 + \mu_0 R_s \frac{\partial M_s}{\partial B_{app}} \tag{2.17}$$

where the factor $\partial M_s / \partial B_{app}$ is the high field susceptibility. This factor arises because true saturation is never reached in real samples for finite fields. It is generally small, so the high field slope of the data is often thought to be mainly due to the OHE. However, for many ferromagnetic metals R_s is much greater than R_0, so that the second term on the right hand side of equation (2.17) can be an appreciable fraction of R_0. Therefore care must be exercised when obtaining values for R_0 from the high field slope of such data. In chapter 6, it will be demonstrated that the AHE provides information about the magnetization processes occurring in $ErFe_2/YFe_2$ multilayers. It is also an interesting effect in its own right, with many open questions regarding its origin.

Chapter 3. Experimental techniques

The experimental methods used in this work to grow and study $REFe_2$ films and multilayers are briefly outlined. The basic principles of MBE are outlined in section 3.1, along with the specific techniques used to grow single crystal $REFe_2$ Laves phase materials. In section 3.2, the principles of the VSM are discussed, together with a description of the methods used to collect the magnetometry data of chapter 4 and 5. In section 3.3, the patterning methods used to collect the transport data are outlined, together with the techniques used to collect the giant magnetoresistance and AHE data of chapter 6.

3.1. Molecular Beam Epitaxy

Molecular Beam Epitaxy (MBE) was originally developed for semiconductor growth. The first metals grown to high quality by MBE were body centred cubic (bcc) Nb-Ta superlattices [101, 102]. Later, face centred cubic (fcc) Ir and hexagonal close packed (hcp) Ru were grown [103], as well as other bcc metals like Cr [104]. The ability to create high quality, epitaxial magnetic nanostructures led to, notably, the discovery of GMR in Fe/Cr superlattices in 1988 [78].

Crystal growth by MBE involves the deposition of atomic elements onto a substrate at an elevated temperature. Typical growth rates are of the order of a few Å/s. This, combined with the ability to shutter the beams in a fraction of a second, allows layer by layer growth and nearly atomically abrupt interfaces between materials. To obtain high purity samples, the material sources must be extremely pure and the process must be carried out in an ultra-clean environment. The substrate is maintained in ultra high vacuum (UHV) during its *in-situ* preparation and during the growth process. Typically, the background pressure in the growth chamber is around 4×10^{-8} mbar. The technique also allows *in-situ* surface characterization by such tools as Reflection High Energy Electron Diffraction (RHEED) and Auger Electron Spectroscopy (AES). RHEED allows real-time monitoring of the surface lattice parameter and diffracted intensity profiles, and can also be used to calibrate growth rates. Electrons reflect from the surface and strike a phosphor screen, creating a pattern consisting of a specular reflection and diffraction pattern. The diffraction pattern is indicative of the surface crystallography. A smooth surface creates a streaky diffraction pattern. If the surface is rough, the streaks are 'spotty' and the diffraction pattern less clear. Polycrystalline surfaces result in rings circling the straight through beam, and amorphous surfaces generate a haze rather than a diffraction pattern.

The $REFe_2$ films and multilayers that are the subject of this thesis were grown by Roger Ward, of the Clarendon Laboratory at Oxford University. They were created by MBE using the Balzers UMS 630 UHV facility, a schematic of which is shown in Fig 3.1. The system has both a growth chamber and a sample introduction (loadlock) chamber, allowing samples to be brought into and out of the growth chamber while

maintaining vacuum. The growth chamber is pumped by both a turbo molecular pump and a Titanium Sublimation Pump (TSP). There are five independently heated evaporation sources. Two effusion cells are heated by radiation from a resistance heated filament. These are suitable for evaporating metals with a relatively high vapour pressure below 1300°C. When higher evaporation temperatures are required, the source can be bombarded directly by three high energy electron beam (e-beam) guns. A liquid nitrogen cryoshield surrounds the sources, providing additional trapping of impurities.

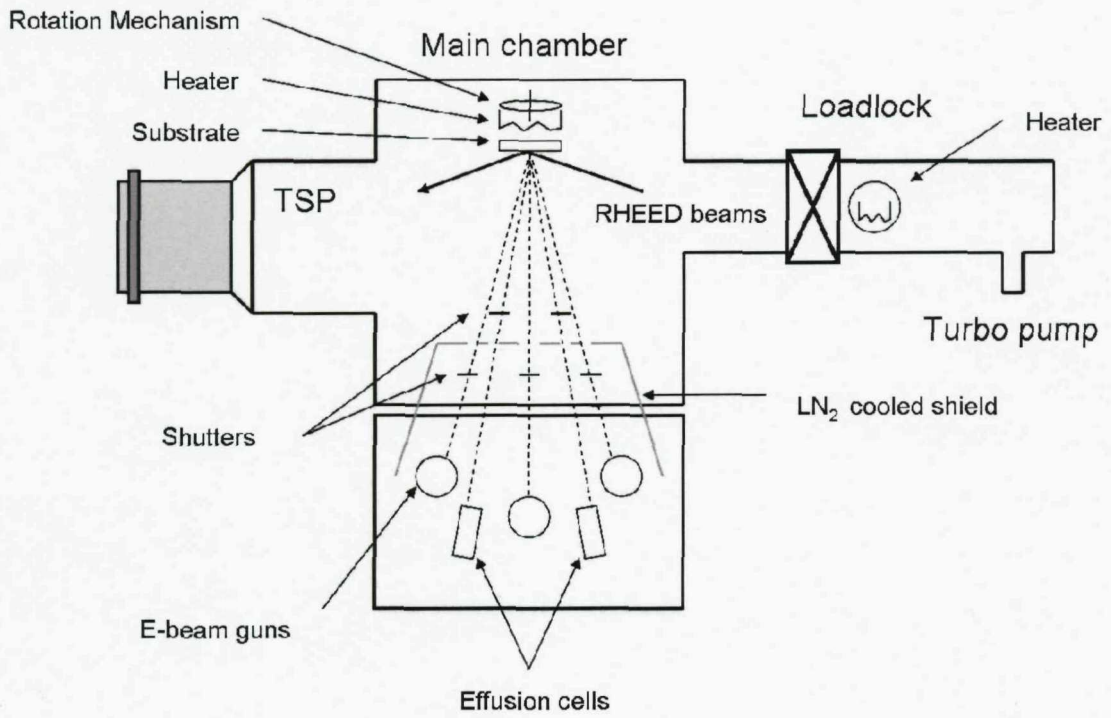

Figure 3.1. Schematic of the MBE facility used to grow the $REFe_2$ films and multilayers.

The exact growth conditions of the films and multilayers discussed in this thesis depends on the required sample properties such as growth orientation and material composition. In general, the procedure closely follows that described by Bentall *et al.* [105]. An epi-prepared $(11\bar{2}0)$ sapphire substrate of dimensions 10×12 mm is out-gassed at 800°C for several hours. A buffer layer is deposited on the heated substrate. The buffer layer provides relief from the strain produced by the lattice mismatch between the $REFe_2$ Laves phase and the substrate, and also provides a chemical barrier to prevent inter-diffusion between the RE metals and the substrate. For (110)

growth this is typically around 75 Å of (110) Nb. Next, a seed layer of typically 20 Å Fe is deposited at a temperature of around 500°C. The seed layer relaxes the mismatch strain between the $REFe_2$ Laves phase and the bcc Nb. The Laves phase is grown on top of this, at temperatures ranging from 750°C for thick films to 450°C for multilayers. Films and multilayers have also been grown in (111) orientation. In this case, the buffer layer is typically 100 Å of (110) Mo and there is no seed layer. The full epitaxial relationships are

$$(110)/[1\,\bar{1}0]\mathrm{Nb} \,||\, (110)/[1\,\bar{1}0]\mathrm{REFe_2} \tag{3.1a}$$

$$(110)/[1\,\bar{1}0]\mathrm{Mo} \,||\, (111)/[1\,\bar{1}0]\mathrm{REFe_2} \tag{3.1b}$$

for (110) and (111) growth, respectively. RHEED patterns obtained during the growth process indicate that the epitaxy proceeds initially via 3D (island) growth. The resulting RHEED patterns are very spotty. During the first few repeats the streaks develop progressively from initial 3D spot patterns to streaks, indicating decreasing surface roughness. Fig 3.2 shows the RHEED patterns for a typical sample after the surface smoothes. The well-formed streaks signify that the growing surface contains only single or double atomic plane steps over a lateral distance equal to at least the coherence length of the electron beam (of order 500 nm).

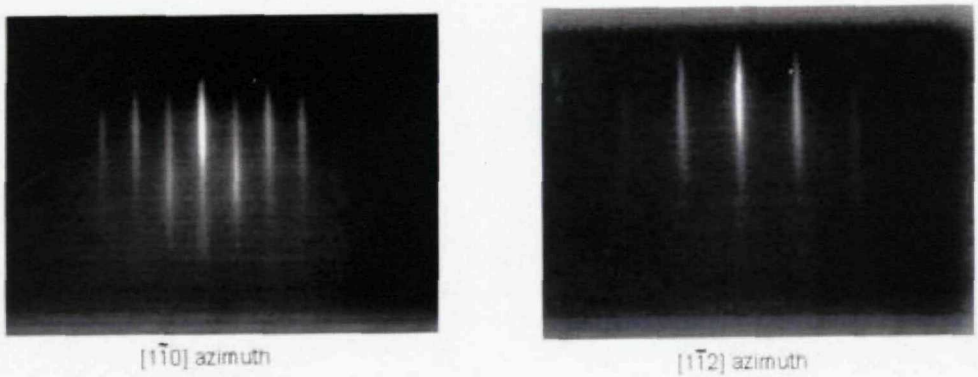

Figure 3.2. RHEED patterns obtained during epitaxial growth of a typical multilayer

The difference in the thermal expansion coefficients of sapphire and $REFe_2$ generates tensile strain in the samples [51, 71]. The exact size and direction of the strain depends on the sample composition. For example, in (110) $DyFe_2$ films there is an average of around 0.6% lattice expansion in the film plane and around -0.4%

contraction along the growth direction [71]. The magneto-elastic strain energy associated with this can modify the easy axis direction [71] and the anisotropy parameters [106] of epitaxial $REFe_2$ films relative to the bulk. Though the strain energy itself is temperature dependent, it decreases more slowly with temperature than the magnetocrystalline anisotropy. This leads to a temperature dependence of the easy axis in some cases, as discussed in section 2.2.

3.2. The Vibrating Sample Magnetometer

The VSM is accepted as the standard magnetic measurement technique [107, 108]. The technique allows for fast and easy collection of bulk magnetization curves. It can be used to investigate moments as small as 10^{-7} Am^2. The first uni-axial VSM was developed in 1956 by Foner and Van Oesterhart [109, 110].

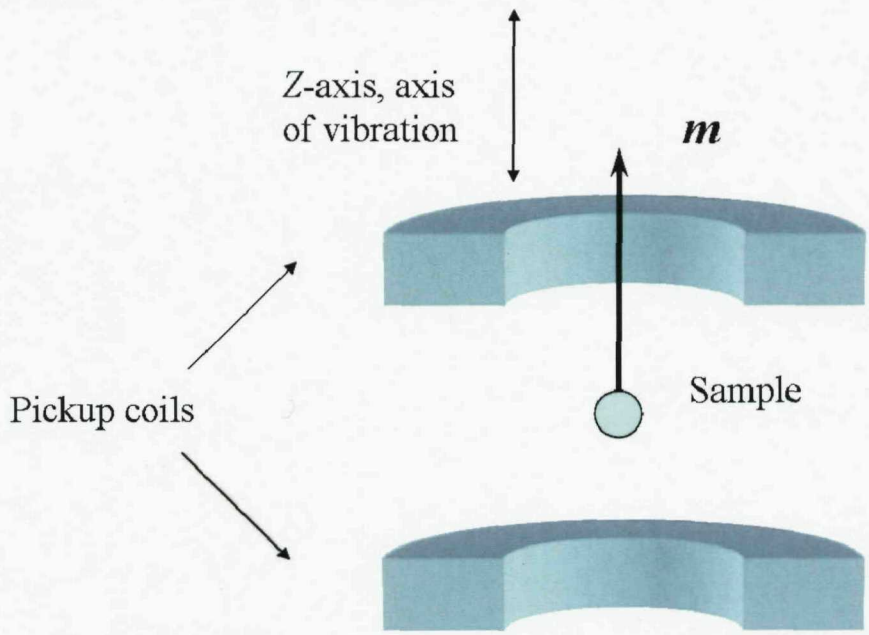

Figure 3.3. A schematic representation of the pick up coils and sample in a uniaxial VSM

A schematic representation of the heart of a uniaxial VSM can be seen in Fig. 3.3. A magnet produces a magnetic field in the z-direction. The field must have a high degree of homogeneity. The sample is mounted on a cylindrical rod or other suitable holder. It is assumed that the sample is homogeneously magnetized by the applied field and small enough to be considered as a simple magnetic dipole. The holder and sample vibrate with sinusoidal motion along the field direction. The frequency of vibration is

typically in the range 10 Hz – 1000 Hz, with amplitude of order 1mm. The vibration of the magnetized sample results in a change of flux through the pickup coils. This in turn induces an electromotive force (emf) ε in the coils. For vibration in the z-direction with frequency ω, amplitude z_a and equilibrium position z_0, a full derivation[11] yields the result

$$\varepsilon = z_a \omega m \sin(\omega t) G(z_0) \tag{3.1}$$

where m is the magnetic moment of the sample in the z-direction, t is time and the term on the right of equation (3.1) is the geometric sensitivity function

$$G(z_0) = \left. \frac{d(\mathbf{B}/\mathbf{I})}{dz} \right|_{z_0} \tag{3.2}$$

where **B** is the field that would be generated by a fictitious current **I** circulating in the pickup coils. $G(z_0)$ is assumed to be constant over the whole sample volume, and is determined using known magnetic moments such as nickel, platinum or palladium. The generalized form of this function may be written $G(x,y,z)$ where x, y and z are the coordinates of the sample position. Optimum measurements are obtained by maximizing $G(z)$ and minimizing $G(x)$ and $G(y)$. Any vibration of the sample in the x or y directions should be avoided. The sample should also be small in x and y dimensions compared with the internal dimensions of the coils. Careful positioning of the pickup coils is essential. The signal from the coils is amplified using a phase sensitive detector or lock-in amplifier. Any inhomogeneity of the magnetic field over the range of motion of the sample will also be a source of error. Variations in the frequency or amplitude of the vibration are other possible sources of error. Any noise at the frequency of vibration, caused for instance by vibration of the superconducting magnet and/or coils, must be avoided.

The experimental data reported in chapters 4 and 5 was obtained using an Oxford Instruments Aerosonic 3001 Vibrating Sample Magnetometer[111]. This is a uniaxial VSM. It incorporates a superconducting magnet that provides fields up to ±12 T. The magnet has a homogeneity of 0.1 % over a 10mm diameter sphere[11]. The sensitivity

of the instrument is ~ 2×10^{-6} emu (2×10^{-9} Am^2). The magnet is surrounded by a jacket of liquid He, which cools it to the superconducting state. This, in turn, is surrounded by a vacuum. Outside this space is a jacket of liquid nitrogen. The vacuum and liquid nitrogen shield reduce the rate at which liquid He is lost through evaporation. Liquid He can be sprayed through a needle valve into a space around the sample in order to cool it. The liquid He expands adiabatically as it flows into the space through the needle valve. Thus, temperatures below liquid He temperature (4.2 K) are achievable. There is a heater within the magnet bore. The heater power and the flow of liquid He from the needle valve are adjusted to stabilise the temperature at a given target value.

Measurements are made on roughly square pieces of the film. These pieces are typically 5mm on a side. Larger sizes risk friction with the sides of the pick up coils and are a source of noise, but smaller samples lead to smaller signals. 5mm samples provide sufficient signal (typically ~ 1×10^{-3} emu, 1×10^{-6} Am^2) while being small enough to avoid frictional noise.

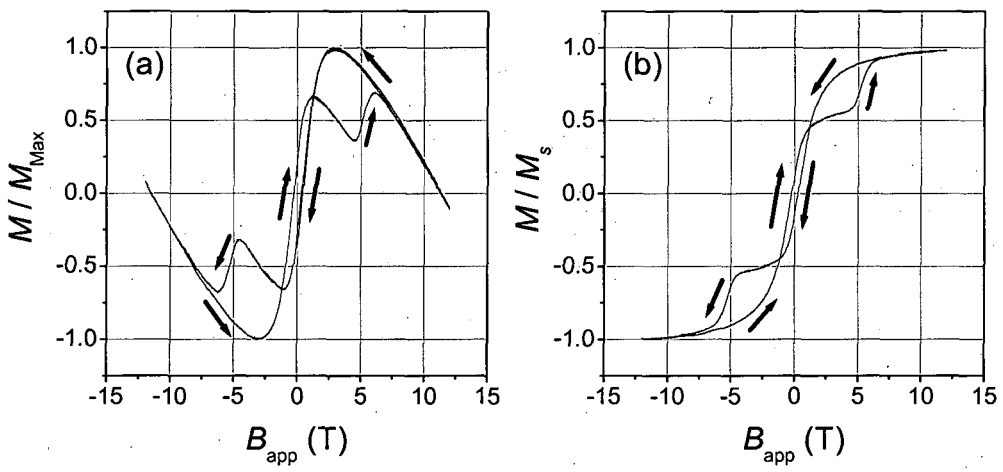

Figure 3.4. Magnetization curves for the (110) multilayer [$ErFe_2$(50 Å)/YFe_2(150 Å)] × 20 at a temperature of 100 K with the diamagnetic contribution due to the sample holder and rod included (a) and removed (b). The arrows indicate the direction in which the field is being swept.

The thickness of the Laves phase films is typically 4000 Å. The sapphire substrate thickness is ~ 1mm. The sample holder and sapphire substrate have a very large volume compared with the Laves phase material. Therefore, the data obtained shows a significant diamagnetic component from the holder and substrate. This component is

removed by a simple linear subtraction. As an example, magnetization data for the (110) multilayer [$ErFe_2$(50 Å)/YFe_2(150 Å)] × 20 at 100 K is shown in Fig 3.4 (a,b). The data in Fig 3.4 (a) includes the linear diamagnetic contribution of the substrate and holder. Fig 3.4 (b) shows the same data after a linear subtraction has been made to remove the diamagnetic contribution.

The VSM measures the moment of the entire sample in emu, where 1 emu = 1×10^{-3} Am^2. If values for the magnetization of the sample are to be made, the sample dimensions must be known. In this thesis, magnetization is sometimes shown in units of Bohr magnetons per formula unit (μ_B/f.u.). But when the quantitative values of magnetization are not important, the normalized magnetization M / M_s is often used. This is simply the ratio of the magnetization M to its value at saturation M_s. In order to convert from emu to Bohr magnetons per formula unit it is important to know the lattice parameters given in chapter 2. If m(emu) is the moment in emu and $M(\mu_B/\text{f.u.})$ is the magnetization in μ_B/f.u. then for an $ErFe_2/YFe_2$ multilayer

$$M(\mu_B/\text{f.u.})=\frac{m(\text{emu})}{(N_E+N_Y)\times\mu_B} \tag{3.3}$$

where N_E is the number of $ErFe_2$ formula units and N_Y is the number of YFe_2 formula units. N_E is given by

$$N_E=\frac{8At_E}{a_E^3}\times n \tag{3.4}$$

where A is the surface area of the sample, t_E is the thickness of an $ErFe_2$ layer, a_E is the $ErFe_2$ lattice parameter and n is the number of bilayer repeats. The factor of 8 appears because there are 8 formula units in a unit cell. In exactly the same fashion

$$N_Y=\frac{8At_Y}{a_Y^3}\times n \tag{3.5}$$

where t_Y and a_Y are the thickness of an YFe_2 layer and the YFe_2 lattice parameter, respectively.

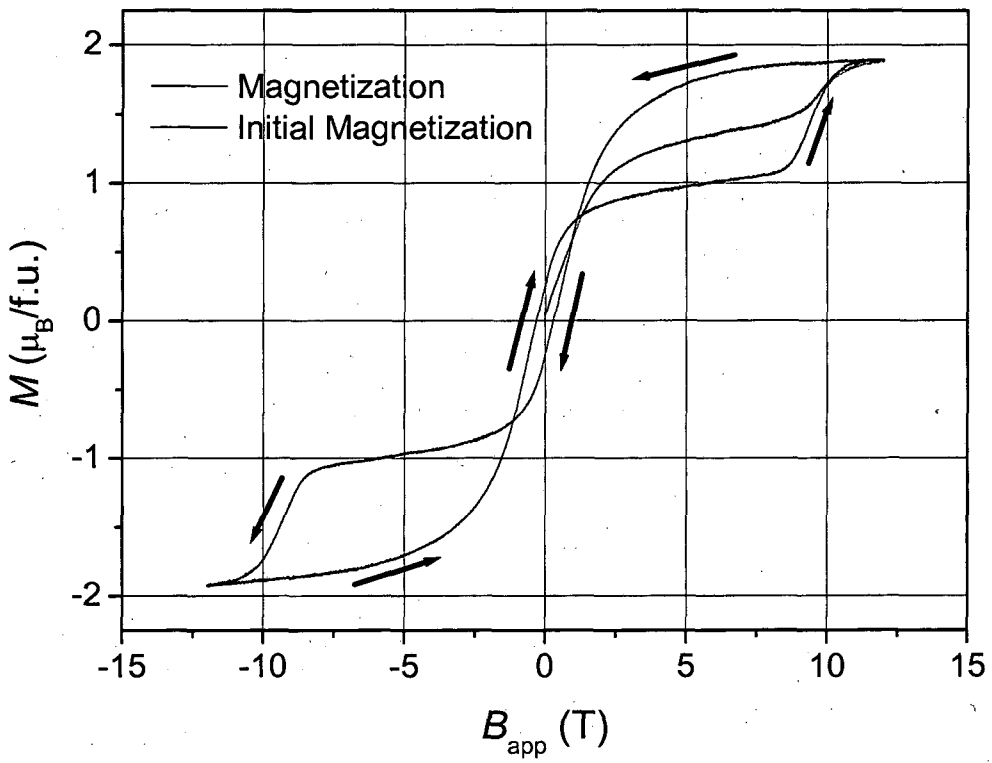

Figure 3.5. Magnetization curve for the (110) multilayer [$ErFe_2$(50 Å)/YFe_2(150 Å)] × 20 at 10 K. The field is applied in the [110] direction. The arrows show the direction in which the field is being swept. The red curve shows the magnetization on applying a field to the multilayer in the virgin state.

It is important to apply a maximum field sufficient to saturate the magnetization of a sample. The magnetic history of the sample being measured can also be important. In the virgin state, there are many randomly oriented domains, resulting in a net zero magnetization. If a positive field is applied, domains aligned parallel with the field grow at the expense their antiparallel counterparts. This process gives rise to the initial increase in magnetization as the applied field is increased from zero. At magnetic saturation, the sample can be considered as a single domain. During the course of a full hysteresis loop, the sample will be exposed to a negative field large enough to reverse its magnetization. If the field is then brought back to a large positive value, the magnetization curve will not generally lie on top of the initial magnetization curve. As an example, magnetization data for the (110) multilayer [$ErFe_2$(50 Å)/YFe_2(150 Å)] ×

20 at a temperature of 10 K is shown in Fig 3.5. The initial magnetization curve is shown in red.

3.3. Magneto-transport

Some of the magneto-transport measurements were performed in-house and some were performed at the Grenoble High Magnetic Field Laboratory (GHMFL).

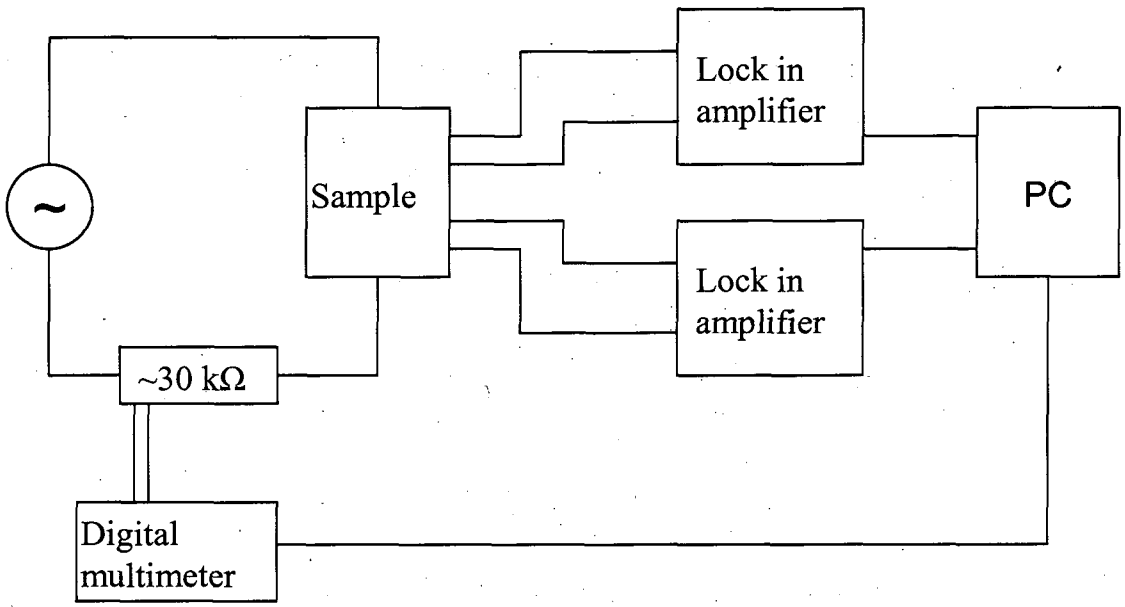

Figure 3.6. Block schematic of a magneto-transport experiment.

A schematic representation of the typical set up used in-house is shown in Fig. 3.6. A signal generator provides an a.c. output and a reference signal for the lock-in-amplifiers. The frequency is chosen to avoid the background noise at 50 Hz. The value often used was 61 Hz. The output is fed through a large resistance, typically 30 kΩ. The resistance of the sample is of order 1 ohm. The large resistance in series with the sample limits the current through the sample to the order of 100 μA or less and ensures that the variation of the current through the sample is negligible during a measurement. This simplifies the experiment as it is not necessary to monitor changes in the current as the sample resistance changes. The current is limited to the order of 100 μA as higher currents could damage the silver paste contacts. The number of contacts depends on the experimental geometry. The simplest case is a standard four point measurement in which current flows between two outer contacts and voltage is

measured between two inner contacts. Lock-in-amplifiers measure the voltages between various points of the sample. They have an input resistance of order 1 MΩ. The current in the circuit is determined by measuring the voltage across a known resistance, typically 1 kΩ, in series with the larger resistance. The sample itself is mounted on a brass platform. This platform can be rotated in order to perform experiments with the field along different crystallographic axes. Gold wires are contacted to the sample surface with silver conducting paint.

In-house, a superconducting magnet provides fields up to 14 T. This magnet and the sample are cooled in the same way as the magnet in the VSM. In this case, there are two heaters, one within the magnet bore and one on the sample platform. The heater power and the flow of liquid He from the needle valve are adjusted to stabilise the temperature at the target value. Experiments at the GHMFL were performed with resistive magnets. These are either 10 MW magnets providing fields of ±23 T, or 20 MW magnets providing fields of ±28 T. In either case, the sample is cooled using a flow cryostat, placed within the magnet bore. Data collected at temperatures as low as 3.5 K is reported in chapter 6.

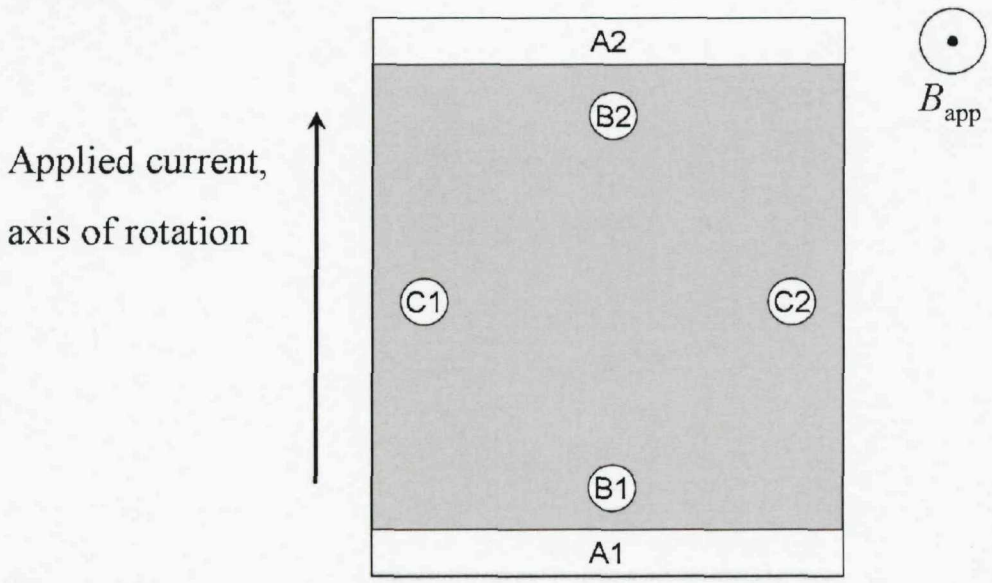

Figure 3.7. Contact arrangement used to collect transport data on un-patterned samples. The current is provided by contacts A1 and A2, B1 and B2 measure the longitudinal voltage and contacts C1 and C2 measure the transverse voltage. Early experiments were performed on samples without the contacts C1 and C2.

Earlier experiments were performed on un-patterned samples, using either a 4-contact or 6-contact arrangement. The contact arrangements are shown in Fig. 3.7. The contacts A1 and A2 used to apply the current are extended to the edges of the sample. Ideally, this provides a current in the x-direction throughout the entire sample. A lock-in-amplifier measures the voltage V_B between contacts B1 and B2. If perfectly aligned along the x-axis, these contacts will measure magnetoresistive effects and not measure any contribution from the Hall voltage. If the six contact arrangement is used, another lock-in-amplifier measures the voltage V_C between contacts C1 and C2. If perfectly aligned along the y-axis, these contacts measure the Hall voltage, with no contribution from magnetoresistive effects. As noted in chapter 2, the applied field B_{app} must have an out of plane component to generate a Hall effect. In practice, the alignment between the contact pairs is not perfect. Thus, a component of the Hall voltage is measured across B1 and B2 (provided B_{app} has an out of plane component). Likewise, a component of the magnetoresistance is measured across C1 and C2. In order to obtain the longitudinal or transverse (Hall) voltage, the data is separated into components that are even or odd in B_{app}, respectively. As noted in chapter 2, both the OHE and AHE have odd field symmetry, whereas magnetoresistive effects like GMR have even field symmetry. Therefore, the even component

$$V_l = \tfrac{1}{2}[V_B(B) + V_B(-B)] \tag{3.6}$$

is the longitudinal voltage between B1 and B2, whereas the odd component

$$V_H = \tfrac{1}{2}[V_C(B) - V_C(-B)] \tag{3.7}$$

is the transverse voltage between C1 and C2. When adding and subtracting the appropriate voltages as shown in equations (3.6) and (3.7), it is important that voltages at increasing positive field are compared to those at increasing negative field. Similarly, voltages at decreasing positive field are compared to those at decreasing negative field. At a given value of B_{app} the magnetoresistance is

$$\frac{\Delta\rho}{\rho_0}(\%) = \frac{V_l(B_{app}) - V_l(B=0)}{V_l(B=0)} \times 100 \tag{3.8}$$

The Hall resistivity ρ_H is given by

$$\rho_H = (V_H / I)t \tag{3.9}$$

where I is the applied current and t is the film thickness.

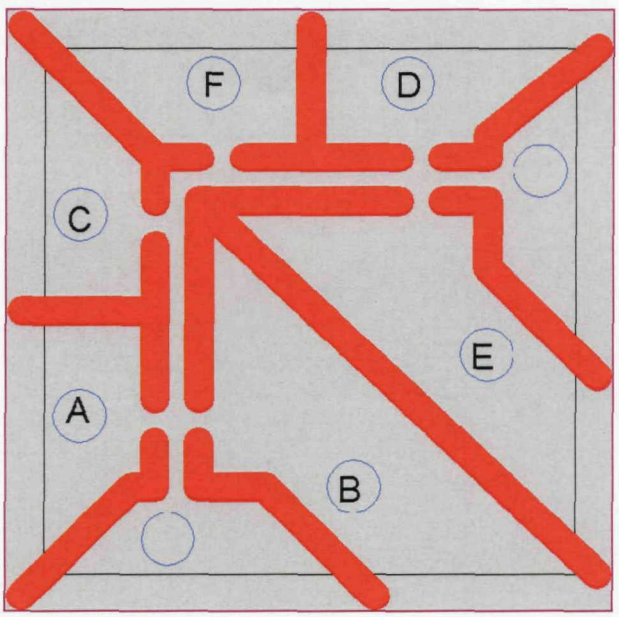

Figure 3.8. Geometry of the patterned samples. The red lines show where the multilayer has been milled away. The blue circles are contact points. The contacts labelled A-F are used to measure voltages, the others provide the current.

Patterned samples have several advantages over un-patterned samples. Quantitative analysis of the resistivity is much more easily performed for samples with a well defined geometry. Patterned samples also have a higher resistance than un-patterned samples, increasing the signal that is measured. Many of the measurements reported in chapter 6 were performed on samples patterned with the geometry shown in Fig 3.8. The width of the current channels is 300 μm, with a typical error of 30-50 μm. The length of the current channels between contacts A and C is 2.25 mm with a typical error of 0.05 mm. The pattern allows simultaneous measurement of the longitudinal and transverse magnetoresistance when the field is applied in plane. When the field is applied perpendicular to the plane, the pattern allows simultaneous measurement of the transverse magnetoresistance and Hall voltage. The pattern is created on a piece of

a film roughly 5mm square, using a computer controlled milling machine. Diamond (hardness 10) coated bits are necessary to mill away the top of the sapphire (hardness 9) substrate. It is relatively easy to obtain values for the resistivity of patterned materials. Detailed measurements of the resistivity versus temperature for a (110) $ErFe_2/YFe_2$ multilayer and (111) $ErFe_2$ film are given in chapter 6. The resistivity curves can in principal provide information about the mechanism of the AHE. They also allow determination of the residual resistance ratio (RRR). The RRR is given by the ratio of the room temperature resistance to the residual resistance at low temperatures. This provides information about the purity of the material and the scattering processes.

Application of a magnetic field perpendicular to the plane of an ideally patterned sample would generate magnetoresistance along AC and DF and a Hall voltage along AB and DE. However, the patterning is not ideal. Misalignment of the contacts results in a small component of the Hall voltage being measured across AC and DF. A small component of the longitudinal voltage is measured across AB and DE. Therefore, it is still necessary to separate the data into odd and even components.

When making measurements using the sample geometry shown in Fig. 3.8, V_{ij} denotes the voltage between two contacts, i and j. Then

$$V_{l1} = \tfrac{1}{2}[V_{AC}(B) + V_{AC}(-B)] \tag{3.10a}$$

$$V_{l2} = \tfrac{1}{2}[V_{DF}(B) + V_{DF}(-B)] \tag{3.10b}$$

$$V_{H1} = \tfrac{1}{2}[V_{AB}(B) - V_{AB}(-B)] \tag{3.10c}$$

$$V_{H2} = \tfrac{1}{2}[V_{DE}(B) - V_{DE}(-B)] \tag{3.10d}$$

Again, it is important to compare the voltages at increasing fields (positive and negative) with each other and similarly for voltages at decreasing fields. In the case where the field is applied in plane, the longitudinal magnetoresistance $\Delta\rho_{xx}/\rho_{xx0}$ and the transverse magnetoresistance $\Delta\rho_{yy}/\rho_{yy0}$ are

$$\frac{\Delta\rho_{xx}}{\rho_{xx0}}(\%) = \frac{V_{l1}(B_{\text{app}}) - V_{l1}(B=0)}{V_{l1}(B=0)} \times 100 \tag{3.11a}$$

$$\frac{\Delta\rho_{yy}}{\rho_{yy0}}(\%) = \frac{V_{I2}(B_{app}) - V_{I2}(B=0)}{V_{I2}(B=0)} \times 100 \qquad (3.11b)$$

When the field is applied perpendicular to the plane the distinction between the two different in-plane directions is less clear. The hall resistivities ρ_{H1} and ρ_{H2} are given by

$$\rho_{H1} = (V_{H1}/I)t \qquad (3.12a)$$

$$\rho_{H2} = (V_{H2}/I)t \qquad (3.12b)$$

Differences in the Hall resistivity or magnetoresistance of these materials along different in-plane directions have not yet been interpreted for the case where the applied field is perpendicular to the plane. In fact, there may be effects due to the crystal anisotropy of the materials.

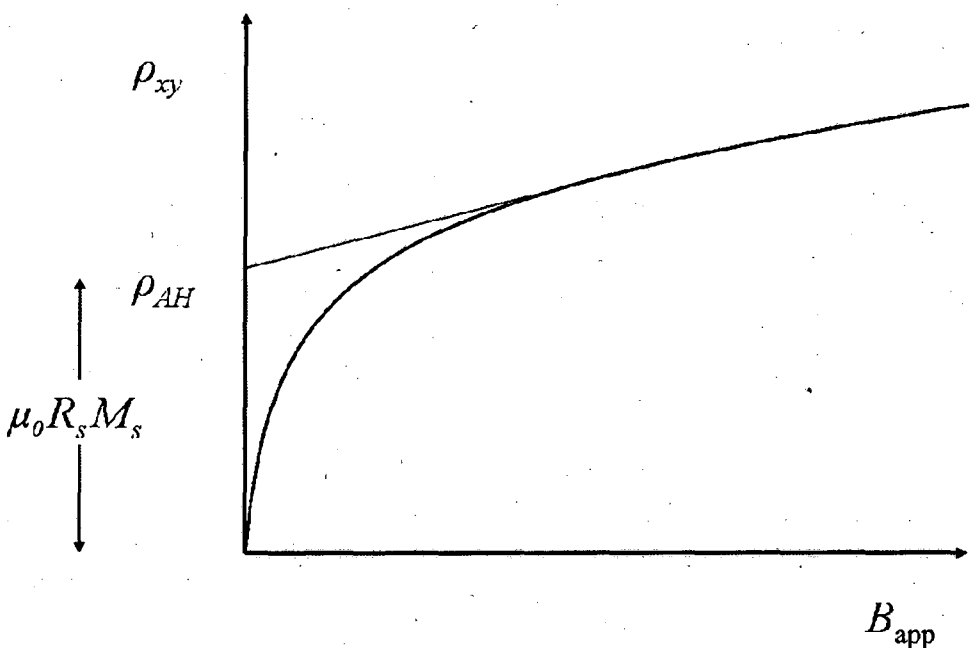

Figure 3.9. Determination of the anomalous Hall resistivity ρ_{AH} from the Hall resistivity ρ_{xy} for a hypothetical metal with appreciable magnetization.

In the case of a material with a relatively simple response to an applied field, such as an $ErFe_2$ film, it is easy to separate out ρ_{AH}, the anomalous contribution to the Hall

resistivity. It is necessary to determine the linear slope of the data at high field. As noted in chapter 2, this slope arises from the OHE and high field susceptibility. Extrapolating along this slope from magnetic saturation to zero field removes these contributions. This is shown schematically in Fig 3.9. The anomalous Hall resistivity ρ_{AH} is given by the intercept as shown. In the case of multilayers, which show a more complex response to an applied field, this analysis may be misleading. For example, in the next chapter an exchange spring driven spin-flop state in which the Er moments, and hence the Fe moments in the $ErFe_2$ layers, point in plane at high fields, is presented and discussed. The in plane moments do not contribute to the AHE and simply removing the linear effects from the point at which the magnetization seems to have saturated will give a deceptively low value of ρ_{AH}.

Chapter 4. Exchange spring driven spin-flop in $ErFe_2/YFe_2$ multilayers

Magnetization loops for (110) MBE grown $ErFe_2/YFe_2$ multilayer films are presented and discussed. The direction of easy magnetization for the Er layers is out of plane, near a <111> type crystal axis. For fields applied along the (110) crystal growth axis, out-of-plane magnetic exchange springs are set up in the magnetically soft YFe_2 layers. The unwinding of these exchange springs leads to a gradual, reversible change of the magnetization. Negative values of the coercive field are obtained at low temperatures for multilayers with sufficiently thick soft magnetic layers. However, there is a cross-over temperature, T_{CO}, above which the coercivity of these multilayers becomes positive, with additional transitions at high fields. The spin configurations occurring during magnetic reversal are identified using micromagnetic modelling. At sufficiently high fields, applied perpendicular to the multilayer film plane, the energy is minimized by an exchange spring driven multilayer spin-flop [112, 113]. In this state, the average magnetization of the $ErFe_2$ layers switches into a nominally hard in plane <111> axis, perpendicular to the applied field. This behaviour is explained with a simple energy argument. Finally, the dependence of T_{CO} on the relative thicknesses of the $ErFe_2$ and YFe_2 layers is described.

4.1. Exchange springs in $ErFe_2/YFe_2$ multilayers

Epitaxial RE-Fe superlattices have proven to be ideal model systems in which to study exchange spring phenomena [10]. They display a rich variety of features, including negative coercivity [34]. But new features continue to be discovered. For example, X-ray Magnetic Circular Dichroism (XMCD) studies on a YFe_2 dominated $DyFe_2/YFe_2$ system reveal complex magnetization reversal processes [35]. In a [$DyFe_2$(30 Å)/YFe_2(120 Å)]×22 superlattice, there are two different regimes. At low temperatures, the magnetization is characterized by a negative coercivity, associated with the unwinding of exchange springs, plus a one-step magnetic reversal as the hard $DyFe_2$ layers switch irreversibly. However at higher temperatures, the loop is characterized by a positive coercivity and a three-step magnetic reversal process. In the latter, the switching of the YFe_2 and $DyFe_2$ layers take place at different fields [35].

Both bulk magnetometry measurements and micromagnetic modelling were performed to characterize a series of (110) MBE grown $ErFe_2/YFe_2$ multilayers. Data was obtained for the three superlattices [$ErFe_2$(100 Å)/YFe_2(50 Å)] × 27 (SL1), [$ErFe_2$(50 Å)/YFe_2(100 Å)] × 27 (SL2), [$ErFe_2$(50 Å)/YFe_2(150 Å)] × 20 (SL3) and a 4000 $ErFe_2$ film (F1). The magnetic data was obtained using a vibrating sample magnetometer, using applied fields B_{app} of up to ± 12 T, within a temperature range of 10 to 310 K [111]. The multilayers were grown by MBE following a procedure described elsewhere [114].

For a full description of the $ErFe_2$ films and $ErFe_2/YFe_2$ multilayers see section 2.2. The measurements shown here have been obtained for (110) films and multilayers. The magnetocrystalline easy axes in the hard $ErFe_2$ layers are parallel to the <111> type crystal axes, however the magneto-elastic strain term ($b_2\varepsilon_{xy}$) (see Mougin *et al* [51, 71]) favours an easy axis nearly along the out of plane <111> axes, roughly 35° from the growth axis and in the $[11\bar{1}]-[110]$ plane.

Exchange springs form when it is energetically favourable to do so. As described in section 2.3, the important contributions to the energy are anisotropy of the hard layers,

the Zeeman energy and the exchange energy. Calculation of the magnetization of the compounds within the multilayer and the anisotropy at the rare-earth sites have been performed by Martin *et al.* (2006) [70]. Fig 4.1 (a) shows the variation of the magnetic moment for $ErFe_2$ and YFe_2 with temperature. The magnetic moment on the Er sites falls off rapidly with increasing temperature, while the variation of the Fe moment is much slower. Fig 4.1 (b) shows the anisotropy barrier in Er, plotted against temperature. The anisotropy also decreases rapidly as the temperature increases. Drastic changes in the character of the hysteresis loop of $ErFe_2$ films and $ErFe_2/YFe_2$ multilayers occur as the temperature is varied. In this section we detail the low temperature behaviour of $ErFe_2$ films and $ErFe_2/YFe_2$ multilayers. The surprising behaviour of $ErFe_2/YFe_2$ multilayers at higher temperatures will be covered in the next section.

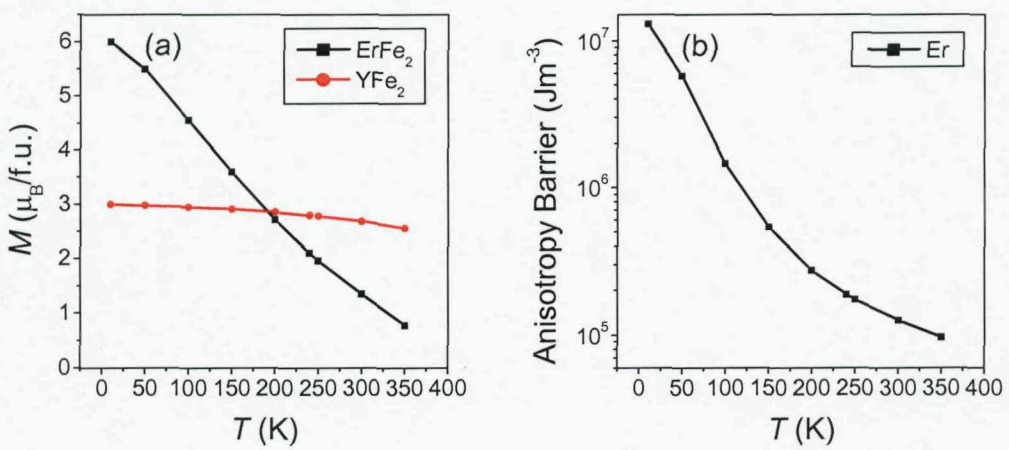

Figure 4.1. Variation with temperature of the magnetization of the compounds that make up the multilayers (a) and the anisotropy energy barrier at the Er sites (b). From Martin *et al.* (2006).

Fig 4.2 shows results obtained for the four samples listed above at a temperature of 100 K with the field applied in the [110] direction, perpendicular to the film plane. The coercivity of F1 (a) at this temperature is 0.79(2) T. SL1 also shows a positive coercivity of 1.65(2) T. The hysteresis curve for SL1 (b) has one irreversible transition at the coercive field and shows no evidence of exchange springs at low fields. The high field necessary to saturate the sample could indicate the presence of exchange springs in the soft layers winding tighter with increasing field. A feature that is most

noticeable for SL1, but that is present in all the curves in Fig 4.2, is a small jump in the magnetization at very low fields. This is thought to be due to the switching of small domains at the edges of the sample.

Completely different behaviour is seen in the magnetization curve of SL2 (c). Starting at high fields, magnetic reversal of the multilayer proceeds by reversible unwinding of the exchange springs in the soft YFe_2 layers. As the spin configuration approaches the AF state the total magnetization of the multilayer decreases. In samples with sufficiently thick YFe_2 layers this can result in the magnetization going negative while the field is still positive. The conventional coercivity of these samples is therefore negative. The coercivity of SL2 at 100 K is -0.06(2) T. The magnetic reversal of the multilayer continues reversibly until the magnetization of the hard $ErFe_2$ layers switches at -3.9(1) T. The larger error in this measurement is caused by the difficulty in determining the exact switching field from the experimental data. This irreversible transition is accompanied by the formation of tight exchange springs in the soft layers.

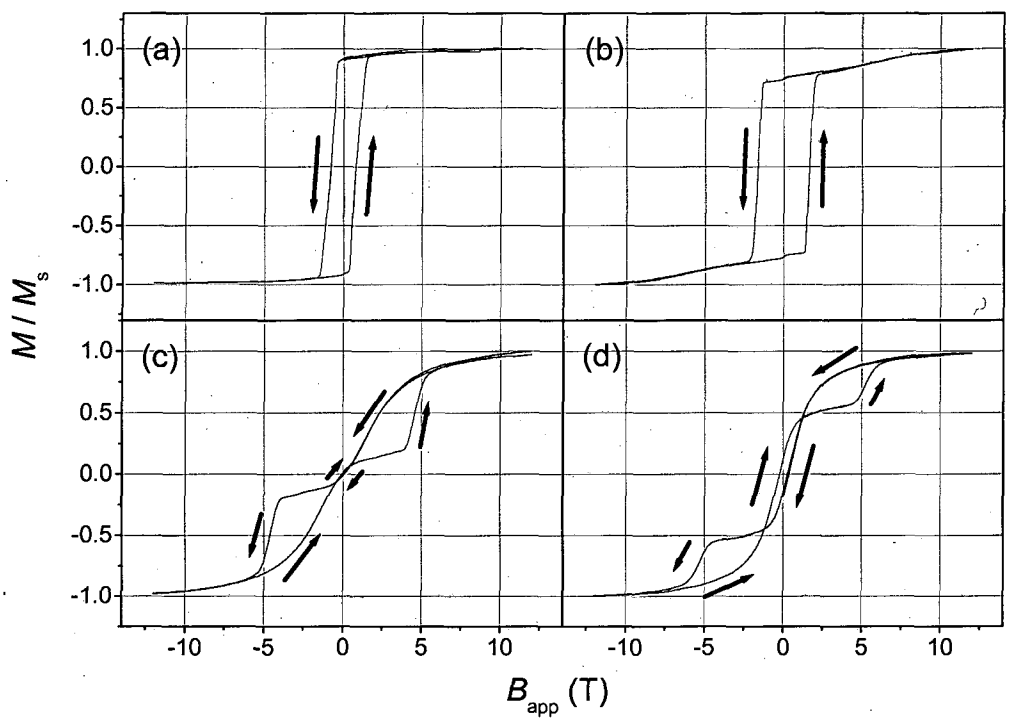

Figure 4.2. Magnetization curves for F1, 4000 Å $ErFe_2$ (a), SL1, [$ErFe_2$(100 Å)/YFe_2(50 Å)] × 27 (b), SL2, [$ErFe_2$(50 Å)/YFe_2(100 Å)] × 27 (c) and SL3, [$ErFe_2$(50 Å)/YFe_2(150 Å)] × 20 (d) at a temperature of 100 K. The applied field is in the [110] growth direction, perpendicular to the film plane. The arrows indicate the direction in which the field is being swept.

Similar behaviour is observed in the magnetization curve of SL3 (d). The thicker YFe_2 layers in SL3 result in a larger negative value for the coercivity of -0.25(2) T at 100 K. As the exchange spring unwinds more and more of the Fe spins in the soft layers point in the opposite direction to the applied field. The thicker these layers are in comparison to the hard layers, the sooner the total magnetization of the multilayer will reverse. For SL3 the irreversible switch of the hard layers occurs at a reverse field of 4.3(1) T. This transition occurs because the gain in Zeeman energy in the hard layers outweighs the cost in exchange energy associated with the exchange spring in the soft layers. As SL3 has thicker soft layers than SL2 a higher applied field is required to initiate the transition.

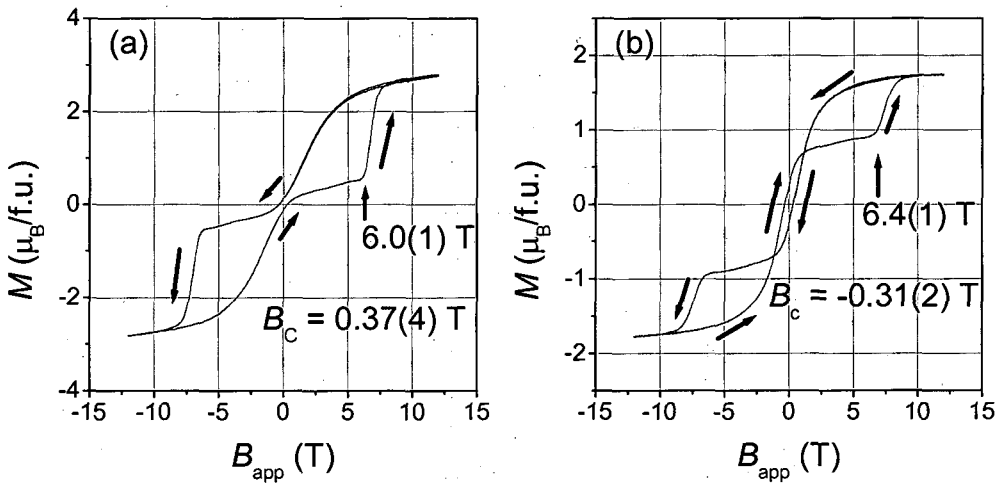

Figure 4.3. Magnetization curves for [$ErFe_2$(50 Å)/YFe_2(100 Å)] × 27 (SL2) (a) and [$ErFe_2$(50 Å)/YFe_2(150 Å)] × 20 (SL3) (b) at a temperature of 50 K. The applied field is in the [110] growth direction.

Figure 4.3 shows the magnetization curves for SL2 (a) and SL3 (b) at a temperature of 50 K. At this temperature there is a higher anisotropy associated with the hard layers and a larger magnetic moment on the Er sites. The hard layers switch at a higher applied field, due to their increased anisotropy. The irreversible switching of the hard layers in SL2 and SL3 now occurs at 6.0(1) T and 6.4(1) T respectively. The coercivity of SL3 is again negative, -0.31(2) T. SL2, however, is now characterized by a positive coercivity of 0.37(4) T. The additional error in the measurement of the coercivity of SL2 is due to a small exchange bias effect that shifts the loop in the positive field direction. This crossover from negative to positive coercivity is a

consequence of the variation of the Er moment with temperature. At 50 K the Er moment is stronger than at 100 K. For SL2 at 50 K, the hard $ErFe_2$ layers contribute more to the total magnetization than the soft YFe_2 layers. In the AF state the total magnetization will thus have the same sign as the $ErFe_2$ magnetization. But this is not true for SL3, due to the thicker YFe_2 layers. The soft layer magnetization in SL3 is greater than the hard layer magnetization for all temperatures studied so far.

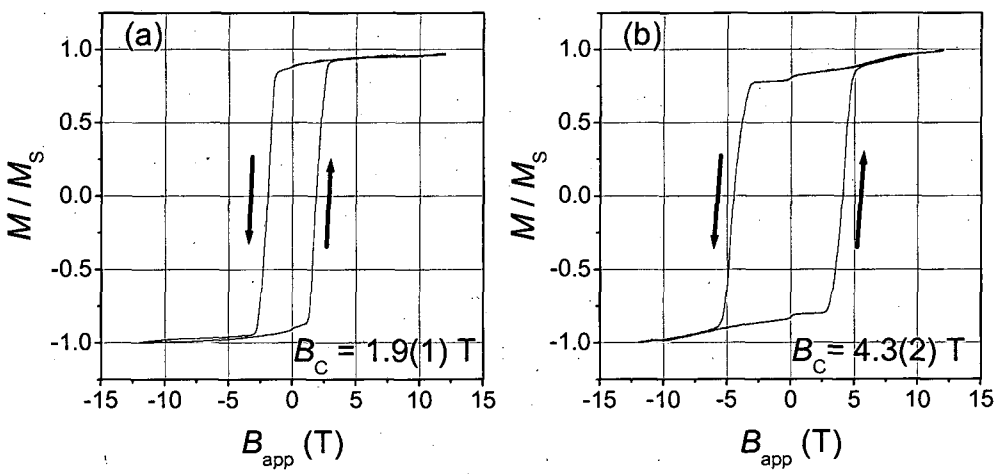

Figure 4.4. Magnetization curves for 4000 Å $ErFe_2$ (F1) (a) and [$ErFe_2$(100 Å)/YFe_2(50 Å)] × 27 (SL1) (B) at a temperature of 50 K. The applied field is along the [110] growth direction.

It is interesting to note that the field at which the hard layers switch is higher for samples with thick soft layers. Fig 4.4 shows the magnetization curves for F1 (a) and SL1 (b) at 50 K. The coercivity of the film is 1.9(1) T and that of SL1 is 4.3(2) T. Again, an exchange bias effect adds extra uncertainty to the coercivity of SL1. The higher switching fields in the multilayers are due to the additional energy considerations associated with the soft layers. While the soft layer magnetization points in the direction of the applied field and all the Fe moments are collinear, the exchange energy and the Zeeman energy of the soft layer are at a minimum. When the hard layers switch, the soft layer spins at the interface are constrained to point opposite the applied field, increasing the Zeeman energy of the soft layers. Exchange springs in the soft layer lower the Zeeman energy at a cost in exchange energy. In order for the hard layers to switch, the gain in Zeeman energy in the hard layers must

outweigh the cost in exchange and Zeeman energy in the soft layers. This pushes the irreversible switching out to higher fields for multilayers with thicker soft layers.

The low temperature magnetization curves of $ErFe_2/YFe_2$ multilayers with thick soft layers can be summarised as follows. At high fields the hard layer magnetization points close to the applied field. At the interfaces between layers the Fe spins are forced to point opposite the field due to the strong Fe-Fe exchange. Tight exchange springs in the soft layers minimize the Zeeman energy at a cost of exchange energy. As the field is reduced the exchange springs unwind reversibly and the magnetization of the multilayer decreases. Eventually the exchange springs unwind completely and the AF configuration is recovered. At this point the total magnetization can be positive or negative, depending on the temperature and the relative thicknesses of the hard and soft layers. Higher temperatures or thick soft layers result in a negative value for the conventionally defined coercivity. At a large negative field the hard layer magnetization switches irreversibly. In summary, the resulting magnetization curves are qualitatively similar to those reported elsewhere for $DyFe_2/YFe_2$ multilayers [115].

Magnetization curves have also been obtained recently for MBE grown (111) materials, a 4000 Å $ErFe_2$ film (F2) and the multilayer [$ErFe_2$(50 Å)/YFe_2(100 Å)] × 27 (SL4). The magnetocrystalline anisotropy in these materials once again favours a <111> easy axis and the strain induced during crystal growth favours the out of plane <111> axes. We therefore expect the easy axis in these materials to be the out of plane [111] direction, perpendicular to the film plane. If the easy axis is perpendicular to the film plane, in the same direction as the applied field, then the magnetization curves obtained for F2 should display higher coercivity and remnant magnetization than the magnetization curves obtained for F1 with the field perpendicular to the film plane. Once again, magnetization measurements were performed using a VSM with applied fields B_{app} up to ± 12 T.

Fig 4.5 shows magnetization curves obtained for F2 (a) and SL4 (b) at a temperature of 100 K. The results for the film do not follow our expectations. With the field applied perpendicular to the film the coercivity is 0.34(2) T, somewhat less than the 0.79(2) T found for F1. The loop for F2 is also less square, M_{rem}/M_{sat} being only 0.55 compared with 0.91 for F1. These results are surprising because if the applied field is

along the easy axis the magnetization curve obtained should resemble an ideal square loop. The results for SL4 (b), on the other hand, do follow expectations. The irreversible switch now occurs at 4.6(1) T, significantly higher than the 3.9(1) T found for SL2. Note that the coercivity is still positive for SL4 at 100 K, even though it is negative for SL2 at the same temperature.

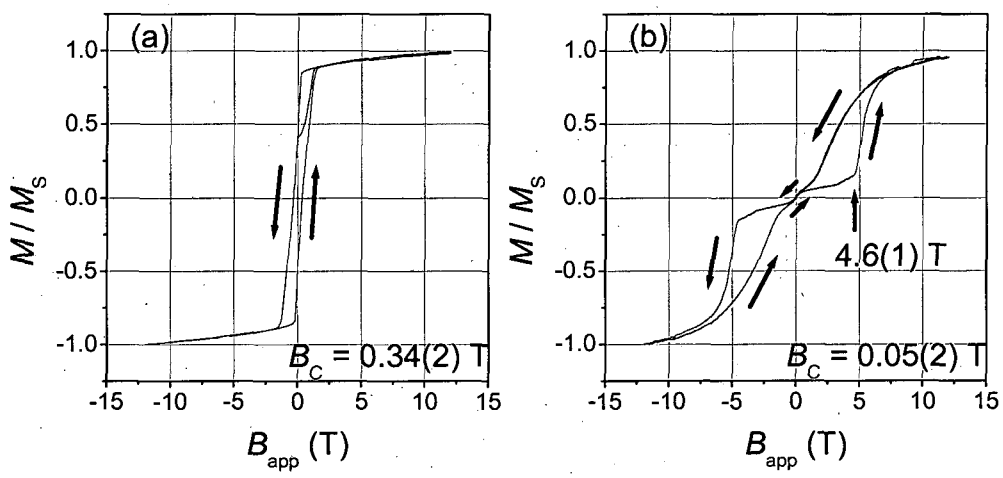

Figure 4.5. Magnetization curves for 4000 Å $ErFe_2$ (F2) (a) and [$ErFe_2$(50 Å)/YFe_2(100 Å)] × 27 (SL4) (b) at a temperature of 100 K. The applied field is in the [111] direction, perpendicular to the film plane.

4.2. Multilayer spin-flop

At low temperatures, magnetic reversal in YFe_2 dominated samples is found to be dominated by exchange springs within the YFe_2 layers. There is just one irreversible switching of the hard layers. But at higher temperatures significant changes occur. Micro-magnetic modelling reveals that this can be attributed to differing spin configurations associated with the anisotropy energy of the $ErFe_2$ layers. In particular, a *multilayer spin-flop state* is found to yield the lowest energy in high fields applied perpendicular to the multilayer plane. In this state the average magnetization of the $ErFe_2$ layers points nearly perpendicular to the applied field direction. The work illustrates a class of spin-flop (SF) transitions driven by magnetic exchange springs in magnetically soft layers. They are generically different from the SF transitions witnessed in the man-made AF multilayers, such as (Co/Re) [116].

Magnetization data was obtained for SL2 and SL3 within a field range of ±12 T, applied along the [110] growth direction. Micromagnetic simulations were performed using the finite difference method with the Object Oriented Micromagnetic Framework (OOMMF) software [117].

At low temperatures the magnetization curve of an $ErFe_2/YFe_2$ multilayer is largely reversible, with one irreversible transition at high fields. However, as the temperature is raised above a crossover temperature T_{CO}, the coercivity becomes positive and the character of the hysteresis loop changes. For SL2 (SL3), T_{CO} is ~180 K (~130 K), respectively. Below T_{CO} there is just one irreversible step in the magnetization curve, but at higher temperatures there are three. This unusual behaviour was confirmed using partial hysteresis loops, carried out above and below T_{CO}.

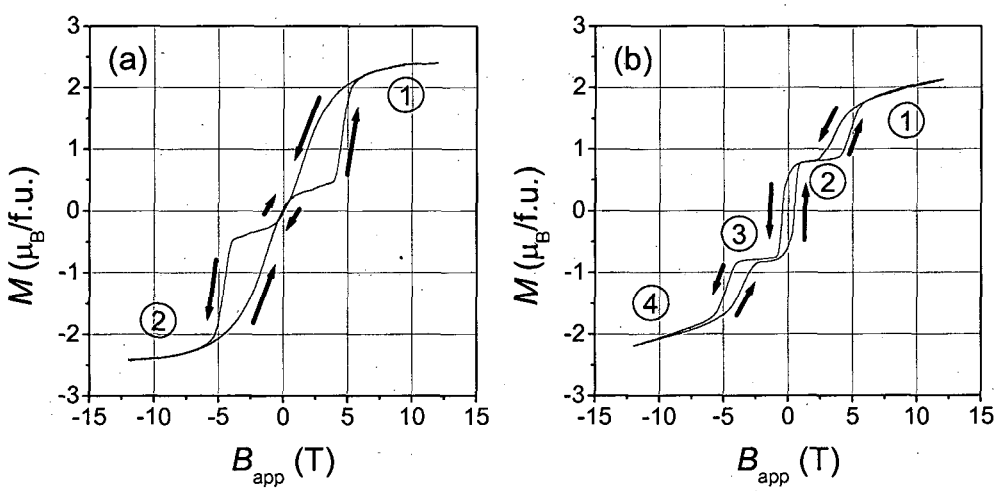

Figure 4.6. Magnetization curves for [$ErFe_2$(50 Å)/YFe_2(100 Å)] × 27 (SL2) at 100 K (a) and 200 K (b). The magnetic field is applied in the [110] direction. The numbers correspond to the numbers on the anisotropy plots of Fig. 4.7.

Fig 4.6 shows magnetization curves obtained for SL2 both above and below T_{CO}. At 100 K (a), reversal involves just one irreversible switching of the $ErFe_2$ layers, at 3.8(1) T. This is similar to the process of magnetic reversal by exchange springs in $DyFe_2/YFe_2$ multilayers described elsewhere, except that the applied field is now parallel to the [110] crystallographic axis and the spin-configurations are out of plane. At 200 K (b), however, there are three irreversible steps in the magnetic loop. The first

irreversible step begins when the applied field is reduced below about 5 T. The second step is associated primarily with the change in polarity of B_{app}, with a positive coercivity of 0.47(2) T. The third step begins at an applied field of -3.4(1) T.

We attribute these changes in the character of the hysteresis loop to differing spin configurations that minimize the total energy of the multilayer. The three contributors are the Fe-Fe exchange energy, the Er anisotropy energy, and the Zeeman energy. The magneto-crystalline energy is calculated using the phenomenological constants K_1, K_2 and K_3 of Atzmony and Dariel [68]. For Er, K_1-K_3 favour <111>-type cubic axes. However the magneto-elastic strain term ($b_2\varepsilon_{xy}$) favours the out of plane [110] crystal growth axis. As a result, the out-of plane e.g. [111] or $[11\bar{1}]$-axes are preferred directions of magnetization. Both the anisotropy constants and the strain term are, of course, temperature dependent, with the former falling more rapidly with increasing temperature. In Fig 4.7 we show the calculated anisotropy surfaces for the $ErFe_2$ layers at 100 K and 200 K. In producing these plots, the anisotropy energy has been shifted by a constant, so that the energy remains positive over the entire surface. At 100 K the energy difference between the maximum and minimum energies is 3.47×10^6 Jm^{-3}, whereas at 200 K it is 0.587×10^6 Jm^{-3}, nearly an order of magnitude smaller. In both cases however, the global minimum is always along an out of plane <111>-axis. For the discussion below, we shall assume that it is the $[11\bar{1}]$ axes. Nonetheless, there are four local minima corresponding to the alignment of the $ErFe_2$ magnetization along in-plane <111>-axes. For these directions, at 200 K, the energy is 2.71×10^5 Jm^{-3} above the global minimum. The arrows shown in Fig 4.7 represent the average direction in which the $ErFe_2$ magnetic moments point, as determined by micro-magnetic modelling. The arrows are numbered to correspond with the numbers on the hysteresis curves of Fig. 4.6.

We interpret the experimental and micro-magnetic data as follows. Below T_{CO} there are only two directions in which the $ErFe_2$ magnetization can point. In a high magnetic field they point out of plane, somewhere between the $[11\bar{1}]$-axis and the applied field along the [110]-axis. But as B_{app} is decreased, the Er moments move closer to the $[11\bar{1}]$ axis, under the action of the strong Er magneto-crystalline anisotropy. Finally, in a sufficiently high negative field, the Er moments switch to

align along an 'inverse' out of plane, say the $[\bar{1}\,\bar{1}\,\bar{1}]$-axis. In summary, the Er and Fe spins are confined to the $[11\bar{1}]-[110]$ plane by the strong Er magneto-crystalline energy and there is just one switching event.

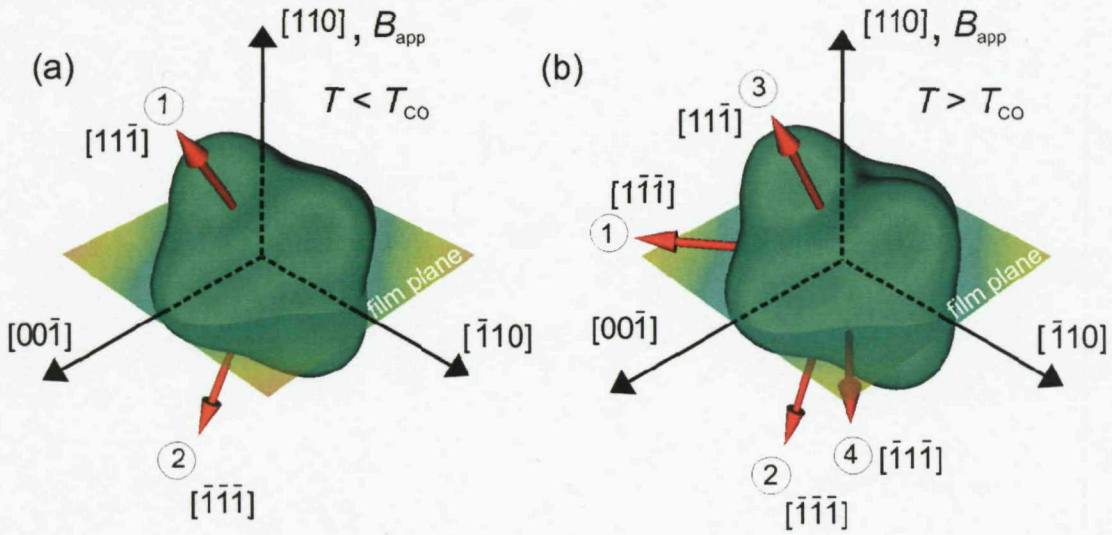

Figure 4.7. Calculated anisotropy energy surfaces for the $ErFe_2$ layers at 100 K (a) and 200 K (b). The red arrows show the average direction of the magnetic moment as the applied field is swept from a high positive value to a high negative one and are obtained by micromagnetic modelling. The numbers on the arrows correspond to the numbers on the magnetization curves of Fig 4.6.

Above T_{CO} there are four directions in which the average $ErFe_2$ moment can point. In a high magnetic field, OOMMF calculations reveal that the average $ErFe_2$ magnetization lies almost perpendicular to the applied field, close to one of the in-plane <111>-axes *e.g.* the $[\bar{1}\,1\,\bar{1}]$-axis. We call this the exchange spring driven spin-flop transition. Here the Er moments take advantage of one of the four in-plane magneto-crystalline local minima. Note that all the moments are confined, primarily, to the $[\bar{1}\,1\,\bar{1}]$-[110] plane (c.f. the $[11\bar{1}]-[110]$ plane at low temperatures). However, as the field is decreased the average the $ErFe_2$ magnetization rotates both *downwards and sideways* to the $[\bar{1}\,\bar{1}\,\bar{1}]-[\bar{1}\,\bar{1}\,0]$ plane, roughly opposite to the applied field. This rotation is driven by (i) the dominant YFe_2 magnetization, (ii) the weakening of the Er anisotropy energy, and (iii) the overall out-of-plane minimum in the Er anisotropy. This rotation signals the first step in the hysteresis loop. On reducing the field to a relatively modest negative value, the $ErFe_2$ layers switch again to point out of plane nearly opposite the applied field direction, but still in the $[\bar{1}\,\bar{1}\,0]-[\bar{1}\,\bar{1}\,\bar{1}]$ plane. This

constitutes the second irreversible step, which can be viewed as simple switching of the soft YFe_2 magnetization. Finally, in a high negative field the third and final irreversible step occurs as the $ErFe_2$ magnetization rotates to take up the exchange spring driven spin-flop state, but this time with the YFe_2 moments in the opposite direction.

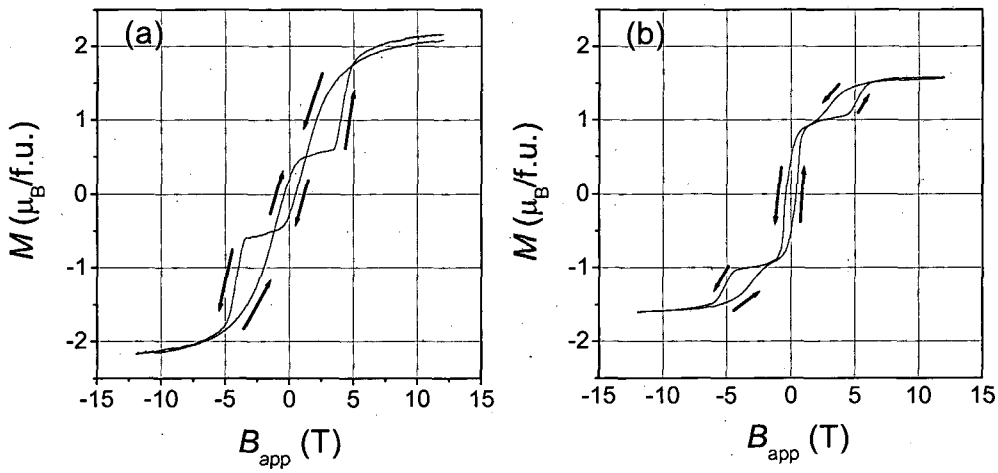

Figure 4.8. Magnetization curves for [$ErFe_2$(50 Å)/YFe_2(100 Å)] × 27 (SL2) (a) and [$ErFe_2$(50 Å)/YFe_2(150 Å)] × 20 (SL3) (b) at 150 K. The applied field is in the [110] direction.

As mentioned above, T_{CO} is dependant on the composition of the multilayers. Fig 4.8 shows magnetization measurements for SL2 (a) and SL3 (b) at 150 K. The result for SL2 is similar to its magnetization curve (or that of SL3) at 100 K. The coercivity is again negative, the reversal is dominated by exchange springs and there is one irreversible switch of the hard layers starting at ± 3.4(1) T. This clearly indicates that 150 K is below T_{CO} for SL2. However, the magnetization loop of SL3 shows the three irreversible transitions and positive coercivity described above for temperatures above T_{CO}. The first irreversible transition begins as the field is reduced below about 5 T. The second transition is associated with the change in polarity of B_{app} and leads to a positive coercivity of 0.41(2) T. Finally, as the applied field reaches -4.3(1) T there is a third irreversible transition.

This temperature dependence can be explained by simple energy considerations. As the temperature is increased two main changes occur. The Er anisotropy associated

with the hard layers falls off rapidly, accompanied by a decrease in the Er magnetic moment. Consequently, the soft YFe_2 layers start to dominate the magnetic behaviour. At low fields the soft layer magnetization points along the field direction, and the hard layer magnetization points opposite the field. In a sufficiently high field the hard layer magnetization switches irreversibly to point along an in plane <111> direction. This transition is driven by the gain in Zeeman energy of the hard layers, but at a cost of anisotropy energy. It is accompanied by the formation of tight exchange springs in the soft layers. The strong Fe-Fe exchange energy prevents the hard layer magnetization from simply aligning along the field direction. Thus T_{CO} can be viewed as the temperature at which the soft layers begin to dominate the magnetic reversal of the superlattice. Clearly this will happen more readily (i.e. at lower temperatures) for superlattices with very thick soft layers.

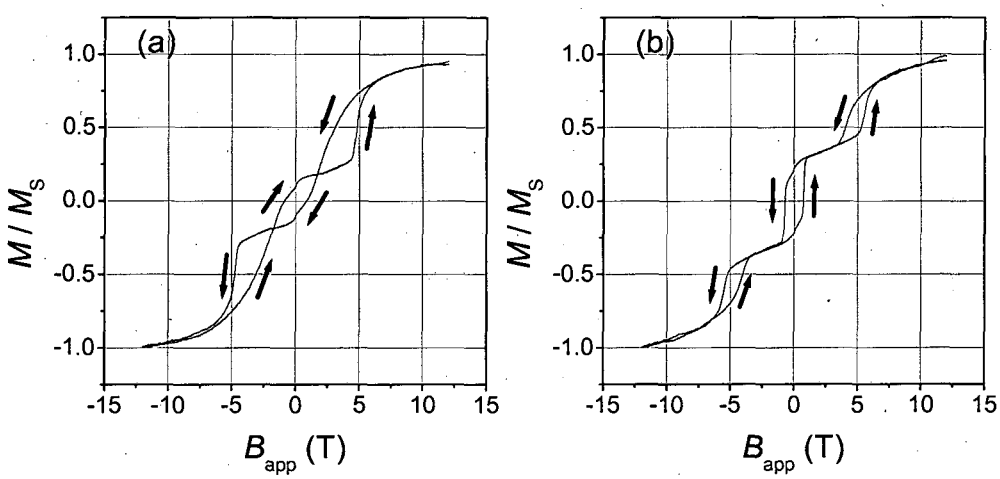

Figure 4.9. Magnetization curves for [$ErFe_2$(50 Å)/YFe_2(100 Å)] × 27 (SL4) at 150 K (a) and 200 K (b). The applied field is along the [111] growth direction.

Exchange spring driven spin-flop behaviour is also seen in (111) $ErFe_2/YFe_2$ multilayers. Fig 4.9 shows magnetization curves for SL4 at 150 K (a) and 200 K (b). At 150 K, below T_{CO} for this superlattice, the single irreversible transition begins at an applied field of 4.3(1) T and the coercivity is -0.81(2) T. The magnetization curve for 200 K has three irreversible transitions and positive coercivity, indicating that 200 K is above T_{CO} for this multilayer. The spin-flop configuration starts to become unstable as the field is reduced below 6.1(3) T. The coercivity is 0.72(2) T.

4.3. Conclusions

Magnetization data has been collected for a rich variety of $ErFe_2$ films and $ErFe_2/YFe_2$ multilayers. The $ErFe_2/YFe_2$ multilayers are very useful model systems in which to study perpendicular exchange springs. The Er moment and anisotropy both fall off quickly with increasing temperature, leading to significant differences in the response of the samples to a magnetic field.

At low temperatures the magnetic reversal of all the superlattices studied is dictated by the hard layers. Magnetic reversal involves a single switch of the hard layers. In the case of the YFe_2 dominated multilayers (SL2, SL3 and SL4) the magnetization curve is largely reversible, a classic sign of exchange springs. The multilayer may show negative coercivity if the soft layers are sufficiently thick.

At high temperatures significant changes occur in the character of the hysteresis loops of YFe_2 dominated multilayers. There are now three irreversible steps in the magnetic reversal and the coercivity becomes positive. At suitably high fields the hard layer spins point at right angles to the applied field. This is called an exchange spring driven multilayer spin-flop. As the field is reduced the hard layer spins switch to point out of plane opposite the applied field. The cross over between the low and high temperature behaviour T_{CO} depends on the multilayer composition and is lower for multilayers with thicker soft YFe_2 layers. T_{CO} can be thought of as the temperature at which the soft layers begin to dominate the response of the multilayer to a magnetic field.

Chapter 5. Multilayers with competing anisotropies

A series of MBE grown (110) $ErFe_2/YFe_2/DyFe_2/YFe_2$ multilayers have been investigated using bulk magnetometry and micromagnetic modelling. $ErFe_2$ and $DyFe_2$ are both hard magnetic materials. These have very different magnetic anisotropies. $DyFe_2$ possesses a uniaxial in-plane anisotropy while $ErFe_2$ favours an out of plane <111> axis. The anisotropy associated with the soft YFe_2 layers is negligible. In practice the coupling between the different hard layers is easily changed by varying the soft YFe_2 layer thickness. The interactions between the competing Er and Dy anisotropies vary both with soft layer thickness and temperature. By tuning these two parameters, we can build up a rich phase diagram of switching processes.

5.1. $ErFe_2/YFe_2/DyFe_2/YFe_2$ multilayers

$ErFe_2/YFe_2/DyFe_2/YFe_2$ multilayers show complex magnetic behaviour. The different hard layer anisotropies compete directly with each other, if there are no YFe_2 spacer layers or these layers are thin. One interesting feature of the $ErFe_2/YFe_2/DyFe_2/YFe_2$ multilayers is that they exhibit 'pre-strung' twisted exchange springs in the remnant state.

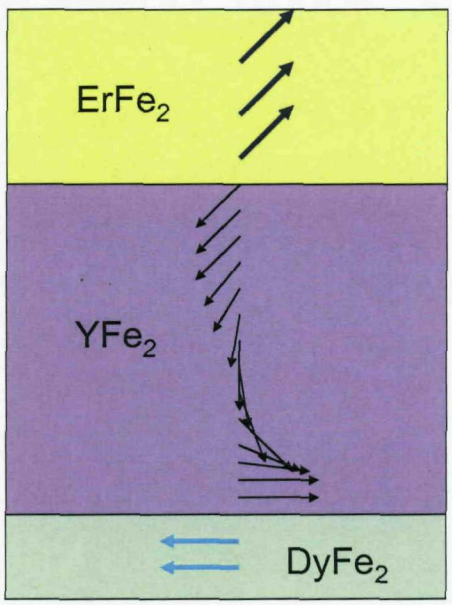

Figure 5.1. Schematic representation of the zero field spin configuration of an $ErFe_2/YFe_2/DyFe_2/YFe_2$ multilayer. A twisted exchange spring is shown in the YFe_2 layer.

The reason for the twisted exchange spring in the remnant state is that the strong Fe-Fe coupling constrains the YFe_2 magnetization to point in different directions at the interfaces with different hard layers. Fig 5.1 shows a schematic representation of such a spring. The $ErFe_2$ easy axis is out of plane, near a <111> crystal axis. By contrast the easy axis of $DyFe_2$ is in-plane along [001] at low temperatures, but moves to a direction 15° out of plane, near $[1\,\bar{1}0]$ at high temperatures [72, 118]. The YFe_2 magnetization reorients throughout the soft layer to minimize the Fe-Fe exchange energy. Pre-strung exchange springs give these materials exchange spring functionalities (GMR, spin transfer torque, etc) in zero field.

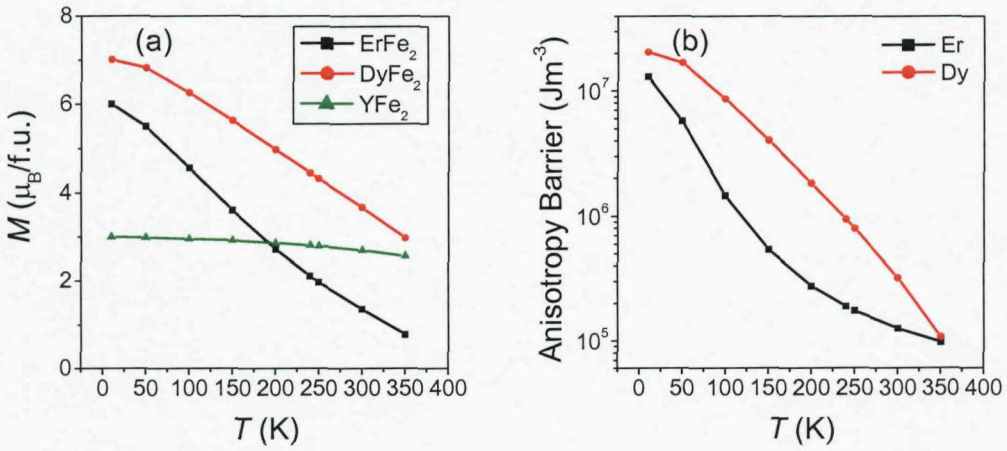

Figure 5.2. Variation with temperature of the magnetization of the compounds that make up the multilayers (a) and the anisotropy energy barrier of the rare earth elements (b). From Martin *et al.* 2006.

The variation of the magnetization associated with the $ErFe_2$, $DyFe_2$ and YFe_2 layers with temperature is shown in Fig 5.2 (a). The $ErFe_2$ and $DyFe_2$ magnetization both fall with increasing temperature; though the magnetization of $DyFe_2$ is always higher than that of $ErFe_2$ within the range shown. On the other hand, the magnetization of the YFe_2 layers remains almost constant within the full temperature range. As in the case of the simpler $ErFe_2/YFe_2$ multilayers, the YFe_2 layers may dominate at higher temperatures, if they are sufficiently thick. Another important parameter is the anisotropy of the different hard layers. Fig 5.2 (b) shows the temperature dependence of the anisotropy barrier in both Er and Dy (the anisotropy barrier is the energy difference between the directions of maximum and minimum energy). The anisotropy barrier falls off faster in Er, and is larger in Dy throughout the relevant temperature range.

The thickness of the soft YFe_2 layers has a direct effect on the exchange coupling between the different RE moments and therefore on the spin configurations of the multilayer. If the soft layer thickness is very large then the different RE layers are effectively de-coupled and switch independently of each other. If, however, the soft layers are very thin, then there is significant exchange coupling between the Er and Dy moments. As explained below, this can force the Er moments to align along a

direction that is unfavourable with respect to the Er anisotropy. This is due to the dominance of the Dy anisotropy, the larger of the two.

Understanding the switching processes of exchange spring systems is vitally important if they are to be utilized for applications. The switching behaviour of multilayers with competing anisotropies can be drastically altered by changing the soft layer thickness or the temperature. The next section details the response of these materials to applied magnetic fields. Bulk magnetometry, performed using a VSM, as well as micromagnetic modelling, performed by Jurgen Zimmermann of the Computational Engineering and Design Group, School of Engineering Sciences, University of Southampton, was employed to explain the rich variety of observed switching processes [119]. The modelling was performed using the finite difference method with the OOMMF software package. The technique has also proved useful for studying $DyFe_2/YFe_2$ multilayers [120], ferromagnetic cones [121], ferromagnetic part spheres [122] and arrays of connected nano rings [123]. The switching behaviour of the mixed $ErFe_2/YFe_2/DyFe_2/YFe_2$ multilayers is even more complex than that described in chapter 4 for $ErFe_2/YFe_2$ films and multilayers.

5.2. Magnetic switching patterns

Bulk magnetometry has been performed on a series of (110) $ErFe_2/YFe_2/DyFe_2/YFe_2$ multilayers. The magnetization data was obtained with applied fields in the range ± 12 T, and between 10 K and 320 K. Micromagnetic modelling was performed for a series of $ErFe_2/YFe_2/DyFe_2/YFe_2$ multilayers with different YFe_2 layer thicknesses, but always with $ErFe_2$ and $DyFe_2$ layer thicknesses of 100 Å and 40 Å, respectively. This ratio of $ErFe_2$ and $DyFe_2$ thicknesses results in a roughly equal contribution to the total magnetization from the two different hard layers over a broad temperature range. Fig 5.2(a) shows the magnetization of the $DyFe_2$, $ErFe_2$ and YFe_2 layers. These values show that both the $ErFe_2$ and $DyFe_2$ layers will have the same total moment at a temperature of around 280 K. The thickness of the YFe_2 layers was between 20 Å and 400 Å. In all cases the applied field is along the [110] growth direction, perpendicular to the film plane.

In Fig 5.3 the experimental (a) and simulated (b) data for [$ErFe_2$(100 Å)/YFe_2(200 Å)/$DyFe_2$(40 Å)/ YFe_2(200 Å)]×10 (SL5) at 100 K can be seen. The qualitative agreement between the curves is very good. There are two irreversible steps in the magnetization curve. The first of these is associated with the switching of the $ErFe_2$ magnetization and takes place at B_{S1}=2.5(1) T. The second is a more gradual reversal associated with the switching of the $DyFe_2$ magnetization. This transition is nowhere near as sharp the one at B_{S1}. The applied field direction, [110], is a hard axis for $DyFe_2$. Therefore the $DyFe_2$ magnetization switches by reversible rotation towards the applied field. The gradual nature of this process makes it difficult to assign an accurate field value for this step. Following Zimmermann *et al.* a field value of $B_{S2}\approx$ 4 T is assigned. These the rest of the loop consists of reversible winding and unwinding of exchange springs in the soft layers. Both the experimental and modelling results indicate that the YFe_2 layers are thick enough to decouple the different hard layers. The hard layers switch separately when the magnetic field is sufficient to overcome the anisotropy barrier of the relevant rare earth.

The simulation does predict negative coercivity, not seen in the experimental results. The latter show a small very small positive coercivity until the temperature is raised to 170 K, at which point the coercivity is small and negative. This discrepancy may be caused by the problem of matching precisely experimental and modelling parameters. The change from positive to negative coercivity is not caused by any qualitative change in the spin configurations occurring during magnetic reversal. In fact, modelling predicts the same spin configurations for all temperatures of 150 K and below for this sample. It is simply that the larger rare earth contribution at slightly lower temperatures keeps the total magnetization positive for positive fields. In fact, the magnetization curve in Fig 5.3 (a) indicates that the magnetization perpendicular to the plane is nearly compensated for SL5 at zero field at 100 K. It should be noted that the switching fields predicted by the model are in excess of those observed experimentally. The one dimensional model used to generate the simulated hysteresis curves cannot take into account the formation of domain walls in the x and y directions, and thus overestimates the fields required to switch the magnetization. This effect is known as Brown's Paradox [124-126].

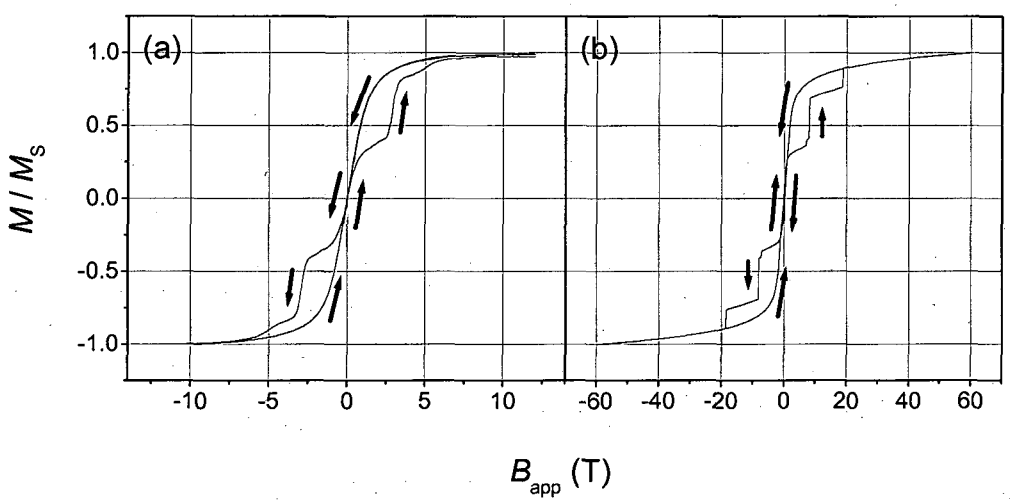

Figure 5.3. Experimental (a) and simulated (b) magnetization curves obtained for [$ErFe_2$(100 Å)/YFe_2(200 Å)/$DyFe_2$(40 Å)/ YFe_2(200 Å)]×10 (SL5) at 100 K.

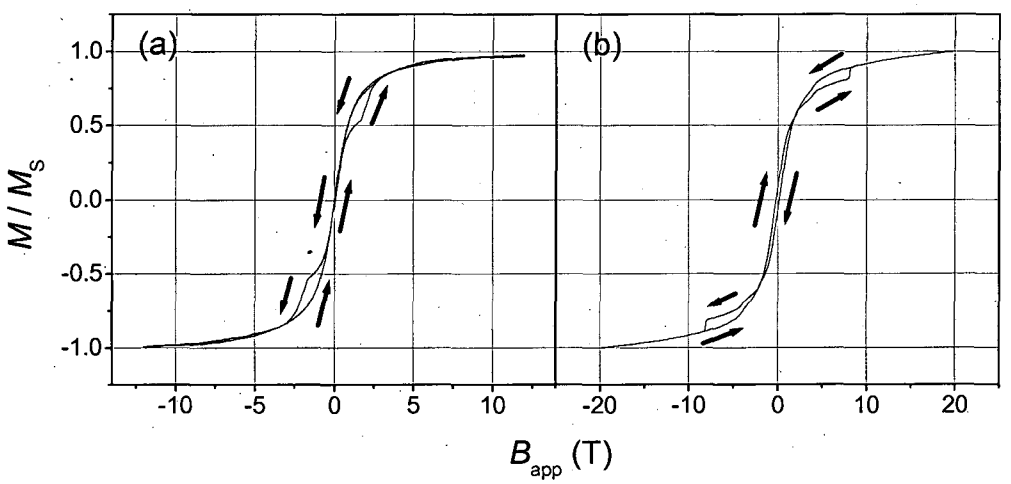

Figure 5.4. Experimental (a) and simulated (b) magnetization curves obtained for [$ErFe_2$(100 Å)/YFe_2(200 Å)/$DyFe_2$(40 Å)/ YFe_2(200 Å)]×10 (SL5) at 200 K

At higher temperatures the magnetization curve of SL5 is markedly different. Fig 5.4 shows the experimental (a) and simulated (b) magnetization curves for SL5 at a temperature of 200 K. The irreversible step associated with the switching of the $ErFe_2$ is no longer apparent. At this temperature, the $ErFe_2$ reverses via the spin-flop direction (as will be illustrated in Fig 5.6 (b), below). The transition into the spin-flop direction occurs at relatively low fields, in the region where the YFe_2 also reverses. The smaller step corresponding to the reversal of $DyFe_2$ remains at B_{S2} = 1.7(1) T (a).

This behaviour is accurately reproduced by the simulated hysteresis curve (b). The $DyFe_2$ layers reverse in the same manner as at 100 K. Both the simulated and experimental magnetization curves possess a very small coercivity. The differences in the magnetization curve compared with the one at 100 K are caused by the different spin configurations accessed by the multilayer during magnetic reversal.

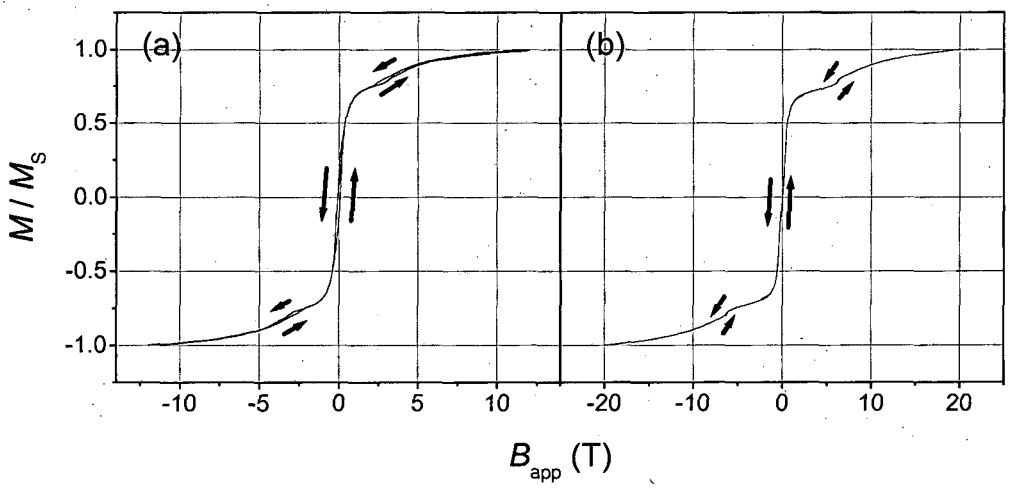

Figure 5.5. Experimental (a) and simulated (b) magnetization curves obtained for [$ErFe_2$(100 Å)/YFe_2(200 Å)/$DyFe_2$(40 Å)/ YFe_2(200 Å)]×10 (SL5) at 320 K and 300 K, respectively.

As the temperature is raised still higher, the magnetic behaviour of the multilayer changes again. Fig 5.5 shows the experimental (a) and simulated (b) magnetization curves for SL5 at 320 K and 300 K, respectively. At high fields all the layers have a component along the field. As the field is reduced the magnetization in the hard layers also reduces. At low fields the magnetization in both the $ErFe_2$ and $DyFe_2$ layers has a component opposite the applied field. At the coercive field all the layers switch together. The coercivity has increased to 0.08(2) T. The experimental curve (a) shows a very small irreversible jump at a field of B_S = 2.8(1) T where the magnetization in the $ErFe_2$ switches irreversibly. Again, the simulated hysteresis loop (b) faithfully reproduces the major features of the experimental loop.

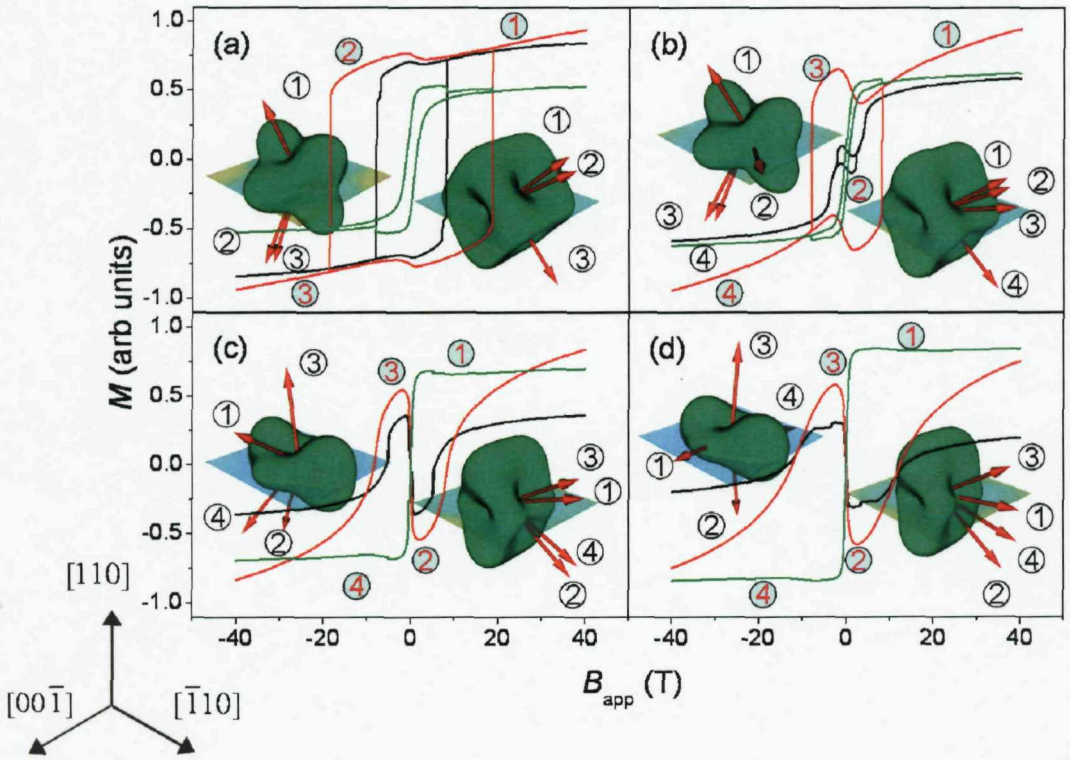

Figure 5.6. Compound specific magnetization curves and calculated anisotropy energy surfaces for [$ErFe_2$(100 Å)/YFe_2(200 Å)/$DyFe_2$(40 Å)/ YFe_2(200 Å)]×10 (SL5) at 100 K (a), 200 K (b), 300 K (c) and 350 K (d). The black, red and green magnetization curves are for $ErFe_2$, $DyFe_2$ and YFe_2, respectively. The green anisotropy energy surfaces on the left (right) of the panels are for $EeFe_2$ ($DyFe_2$). The red arrows indicate the direction of the average magnetization within the relevant material and are labelled by the numbers in clear circles. The red numbers in blue circles label the points during the magnetic reversal, i.e., the field values, which correspond to the arrows with the same number. The out of plane [110] direction and in-plane [00$\bar{1}$] and [$\bar{1}$10] directions are indicated in the bottom left of the figure. From Zimmermann *et al.* (2008).

As in the case of $ErFe_2/YFe_2$ multilayers, micromagnetic modelling has been used to determine the spin configurations of the multilayer. In Fig 5.6 we show the compound specific magnetization curves for SL5 at temperatures of 100 K (a), 200 K (b), 300 K (c) and 350 K (d), obtained by micromagnetic modelling. Fig 5.6 also includes calculated anisotropy energy surfaces for $ErFe_2$ and $DyFe_2$, with red arrows that show the average direction of the magnetization within the compound. The numbers on the arrows correspond to the numbered points on the magnetization curves. At 350 K there is yet another set of spin configurations involved in magnetic reversal, but the

overall magnetization loop shows the same character as at 300 K (Zimmermann *et al.* (2008)). The anisotropy energy surfaces are obtained slightly differently than in the case of $ErFe_2/YFe_2$ multilayers discussed earlier. In light of further research, the values of K_1, K_2 and K_3 have been obtained from calculations that extended the Callen and Callen model to second order [70]. A shear strain term due to the [110] growth of the multilayer (Mougin *et al.* 2000) is incorporated into the strain energy density. The term is approximated by the first order Callen and Callen term $\tilde{K}_2'$ through the formula:

$$\varepsilon_S = \tilde{K}_2'[\alpha_z^2 - \alpha_y^2] \tag{5.1}$$

The values of this are given in Bowden *et al* [106]. However, these values seem to underestimate the strain in $DyFe_2$. It has been shown by vector magnetometry that the easy axes for $DyFe_2$ are at 14° to the film plane at 290 K [72]. In order to simulate this behaviour accurately the values of $\tilde{K}_2'$ given in [106] need to be multiplied by a factor of 2.5.

The compound specific hysteresis loops at 100 K (Fig 5.6(a)) show independent switching of the RE moments at high fields. The $ErFe_2$ magnetization occupies the out of plane $[111]$ or $[11\bar{1}]$ (point 1) direction and switches at a large negative field (point 2) to occupy the $[\bar{1}\bar{1}1]$ or $[\bar{1}\bar{1}\bar{1}]$ directions. This switch is associated with an irreversible step in the hysteresis loop. The $DyFe_2$ magnetization points close to [010] at positive fields (point 1). At a high negative field (point 3) it switches to point close to $[\bar{1}00]$. This switch causes the second irreversible step in the hysteresis loop. The YFe_2 magnetization couples antiferromagnetically at the interfaces to the RE moments. Thus it is constrained to point opposite the applied field.

At 200 K (b) the $ErFe_2$ magnetization reverses via the spin-flop direction. The $ErFe_2$ magnetization occupies the out of plane $[111]$ or $[11\bar{1}]$ direction at high fields (point 1) and switches to the $[\bar{1}1\bar{1}]$ direction at low fields (point 2). At a sufficiently high negative field the magnetization switches again to point in either the $[\bar{1}\bar{1}1]$ or $[\bar{1}\bar{1}\bar{1}]$

direction (point 3). In contrast, the switching behaviour of $DyFe_2$ remains much the same as at 100 K. It should be noted that in this case the spin-flop is unlike the spin-flop described in Chapter 4 for $ErFe_2/YFe_2$ multilayers. At sufficiently high fields both the $ErFe_2$ and YFe_2 magnetization point along the applied field, with a tight domain wall at the interfaces. As the field is reduced, the strong exchange energy can force the $ErFe_2$ magnetization to reverse via the spin-flop direction.

At 300 K (c) the $ErFe_2$ magnetization is closer to the film plane at high fields (point 1) than it is at lower temperatures. The $ErFe_2$ magnetization switches to point in the $[\bar{1}\bar{1}\bar{1}]$ direction, opposite the applied field, as the field is reduced from a high positive value (point 2). As the field reaches a small negative value (point 3) the $ErFe_2$ magnetization switches to point in the $[11\bar{1}]$ direction, and finally, at a high negative field (point 4), the $ErFe_2$ magnetization occupies a direction between $[\bar{1}\bar{1}\bar{1}]$ and the film plane. There are now three irreversible switches of the $DyFe_2$ magnetization. At high fields the $DyFe_2$ magnetization is nearly in plane, just above the $[\bar{1}10]$ axis. As the field is reduced, the magnetization switches to point out of plane, nearly opposite the positive applied field (point 2). At a small negative applied field the $DyFe_2$ magnetization switches again to point nearly opposite the negative applied field (point 3). At a high negative field (point 4) the magnetization is again close to the film plane. This behaviour can be explained by energy considerations similar to those required to explain the $ErFe_2$ spin-flop. As the field is reduced from a high positive value it is energetically favourable for the $DyFe_2$ magnetization to switch into the $[\bar{1}00]$ direction.

At 350 K (d) the behaviour is similar to that at 300 K, but the $ErFe_2$ spin configurations are displaced. At point 2 (3) of the hysteresis curve, the $ErFe_2$ magnetization points almost along $[\bar{1}\bar{1}0]$ ($[110]$), opposite the applied field. The dominance of the strain term at these temperatures significantly alters the $ErFe_2$ anisotropy surfaces, so that these directions become favourable. The $DyFe_2$ magnetization reverses in the same way as at 300 K.

Broadly speaking three different switching regimes are shown for SL5. At low temperatures there is independent switching of the RE moments. When the temperature is raised above a critical value the $ErFe_2$ magnetization reverses via $[\bar{1}1\bar{1}]$, the Er spin-flop regime. When the temperature is raised still further the magnetic reversal becomes dominated by the YFe_2 magnetization. In this high temperature regime the $ErFe_2$ magnetization and $DyFe_2$ magnetization both switch orientation before the applied field reverses.

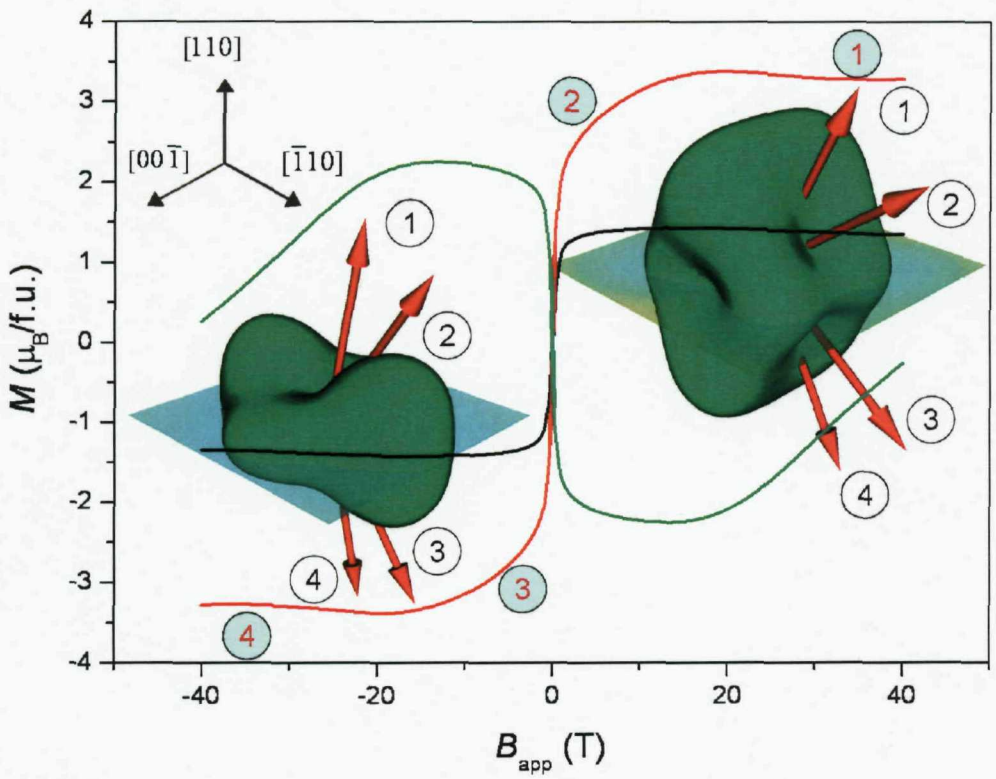

Figure 5.7. Compound specific magnetization curves and calculated anisotropy surfaces for a multilayer with 20 Å YFe_2 layers, but otherwise the same composition as SL5. The data shown is for a temperature of 290 K. The Black, red and green magnetization curves are for $ErFe_2$, $DyFe_2$ and YFe_2, respectively. The anisotropy surface on the left (right) is for $ErFe_2$ ($DyFe_2$). The red arrows indicate the direction of the average magnetization within the relevant material and are labelled by the numbers in clear circles. The red numbers in blue circles label the points during the magnetic reversal, i.e., the field values, which correspond to the arrows with the same number. The out of plane [110] direction and in-plane [00$\bar{1}$] and [$\bar{1}$10] directions are indicated in the top left of the figure. From Zimmermann *et al.* (2008).

The spin configurations in these multilayers depend not only on temperature, but also on the thickness of the magnetically soft YFe_2 layers. Micromagnetic modelling has

been performed for multilayers with YFe_2 layer thicknesses as small as 20 Å and as large as 400 Å. As the thickness of the YFe_2 layers is reduced, the exchange between the moments of the two different RE becomes important. Fig 5.7 shows compound specific magnetization curves at 290 K for a multilayer with 20 Å YFe_2 layers, but otherwise the same composition as SL5. Also shown in Fig 5.7 are the RE anisotropy energy surfaces and red moment arrows, obtained by micromagnetic modelling, indicating the various spin configurations. At 290 K the Er anisotropy is about 100 times smaller than at 10 K (Fig. 5.2(b)). The $ErFe_2$ magnetization points close to the out of plane [110] axis at high fields (point 1). As the field is reduced (point 2) the $ErFe_2$ magnetization moves towards the in plane $[\bar{1}10]$ direction. The exchange between the different RE compounds is strong enough to force the $ErFe_2$ magnetization to switch from state 2 to state 3 via the $[\bar{1}10]$ direction, a hard axis for $ErFe_2$. This is called the coupled switching regime. It is predicted to exist for multilayers with thin YFe_2 layers at higher temperatures, where the exchange energy is enough to overcome the Er anisotropy. At low temperatures the Er anisotropy wins over the exchange, and the multilayer reverses by either the $ErFe_2$ spin-flop or independent switching mechanisms. The coupled switching and $ErFe_2$ spin-flop regimes, as defined above and in Zimmermann *et al.*, are not mutually exclusive. There is in fact a broad range of temperatures where both occur. For most multilayers there is a temperature above which the YFe_2 layers dictate the magnetic behaviour, however this does not occur within the temperature range modelled for a sample with 20 Å or 50 Å YFe_2 layers. For these multilayers, the coupled switching regime persists.

The results of modelling at the full range of temperatures and YFe_2 layer thicknesses can be used to construct a phase diagram of switching mechanisms. This is shown in Fig 5.8 Here we adopt the notation of Zimmermann *et al.* (2008) and give the YFe_2 layer thickness n in nm. The multilayers all show independent switching at low temperatures. The $ErFe_2$ spin-flop regime occupies the region between the independent switching and YFe_2 dominated switching regimes. It begins at 180 K for very thick YFe_2 layers, but extends down to 120 K for multilayers with $n = 2$ nm. This happens because the coupling between the different RE moments pulls the $ErFe_2$ magnetization towards the $[\bar{1}1\bar{1}]$–$[\bar{1}10]$ plane. This coupling is stronger when n is

small, so it can overcome a larger Er anisotropy. Hence, the $ErFe_2$ spin-flop mode occurs at lower temperatures when n is very small. The coupled switching mode is confined to the small n region of the phase diagram. It begins at lower temperatures and persists until higher temperatures as the thickness of the YFe_2 layers decreases. When $n = 2$ nm it stretches from 160 K to the highest temperature modelled. The coupled switching mode does not exist for multilayers with $n > 7$ nm. In the case of a multilayer with $n = 7$ nm the coupled switching mode begins at 210 K and persists until 360 K. The YFe_2 dominated regime occupies the high T, high n quadrant of the phase diagram. At higher temperatures both the anisotropy and the magnetization associated with the RE compounds fall off and the large magnetization of the YFe_2 layers begins to dominate. As n becomes larger, the temperature at which YFe_2 starts to dominate naturally becomes smaller. There is a single instance of a $DyFe_2$ spin-flop reported in Zimmermann *et al.* (2008), however this is believed to be an artefact [127].

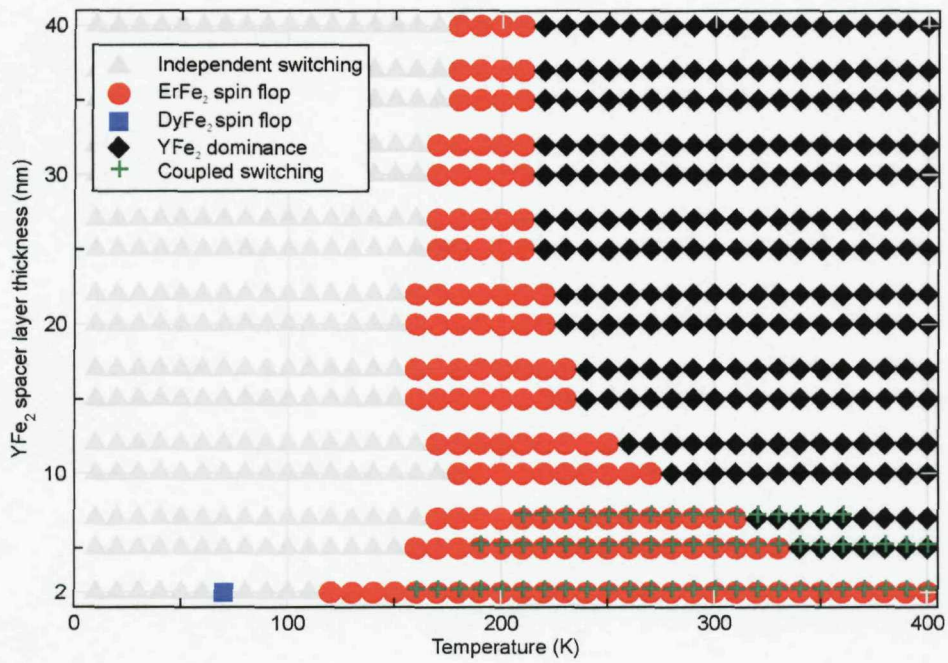

Figure 5.8. Phase diagram of switching states for multilayers with competing anisotropies. From Zimmermann *et al.* (2008).

5.3. Conclusions

$ErFe_2/YFe_2/DyFe_2/YFe_2$ multilayers have been grown by MBE. The hard magnetic materials $ErFe_2$ and $DyFe_2$ possess differing magnetic anisotropies. The interaction between the two different hard materials with the soft YFe_2 layers and with each other has been investigated through bulk magnetometry and micromagnetic modelling. These techniques reveal a rich variety of switching processes. Varying the temperature or the thickness of the soft layers has dramatic effects on the magnetic reversal of the multilayers.

To investigate the effect of varying the temperature, magnetometry data was collected for a typical multilayer, [$ErFe_2$(100 Å)/YFe_2(200 Å)/$DyFe_2$(40 Å)/ YFe_2(200 Å)]×10 (SL5), within a temperature range of 10 - 320 K. Micromagnetic modelling was performed for temperatures in the range 10 - 350 K. SL5 has relatively thick YFe_2 layers. At low temperatures the two different hard layers switch independently of each other. The soft layer magnetization points opposite the hard layer magnetization at the interfaces and reorients throughout the soft layer. At 200 K the $ErFe_2$ layers switch via the spin-flop direction, but the switching behaviour of the $DyFe_2$ layers is the same as for lower temperatures. As the temperature is raised further to 300 K, the soft YFe_2 layers dominate the magnetic reversal of the multilayer, and both the $ErFe_2$ and $DyFe_2$ layers reverse before the applied field.

To investigate the effect of varying the soft layer thickness, micromagnetic modelling was performed for multilayers with different YFe_2 layer thicknesses, but always with $ErFe_2$ and $DyFe_2$ layer thicknesses of 100 Å and 40 Å, respectively. For multilayers with relatively thin YFe_2 layers, a new coupled switching mode is found in which the $ErFe_2$ magnetization is significantly exchange coupled to the $DyFe_2$ magnetization. By performing micromagnetic modelling for a set of multilayers with different soft layer thicknesses and at different temperatures, a phase diagram of switching processes has been built up. The switching processes of $ErFe_2/YFe_2/DyFe_2/YFe_2$ multilayers as shown in the phase diagram are more complex than those described in Chapter 4 for $ErFe_2/YFe_2$ multilayers.

Chapter 6. Giant magnetoresistance and the anomalous Hall effect in $REFe_2$ laves phase materials

A variety of electronic transport measurements have been performed on $REFe_2$ films and multilayers. Giant magnetoresistance (GMR) as high as 12 % has been discovered in $DyFe_2/YFe_2$ multilayers, with the applied field in the sample plane. More recently, $ErFe_2$ films and $ErFe_2/YFe_2$ multilayers have been grown, which order out of plane. Initial measurements on $ErFe_2/YFe_2$ multilayers were performed to characterize the GMR in these materials. Early experiments were carried out on un-patterned samples using four contacts. The data was found to possess a surprising field asymmetry, given that GMR has even symmetry. This was traced to a component of the Hall voltage being measured when the field is applied out of plane. In contrast to GMR, the Hall effect has odd (antisymmetric) field dependence. Thus the data has components with both odd and even field dependence. With appropriate patterning of the samples and choice of experimental geometry, both the magnetoresistance and Hall effect can be measured simultaneously. Measurements of the GMR in $ErFe_2/YFe_2$ multilayers are presented in section 6.1. These were obtained for a range of temperatures, with applied fields both in and out of the film plane.

In section 6.2 measurements of the anomalous Hall effect (AHE) for [ErFe2(50 Å)/YFe2(150 Å)] × 23 are presented and discussed. It is shown that the AHE couples mainly to the Fe magnetization in $ErFe_2/YFe_2$ multilayers. Nevertheless, very specific information about the magnetization processes can be obtained from the AHE data. The AHE data, combined with results both from bulk magnetometry and micromagnetic modelling, has revealed a complex temperature dependence of the magnetic reversal processes.

6.1. Giant magnetoresistance in $REFe_2$ films and superlattices

Magneto-transport measurements have been performed on a variety of $REFe_2$ films and multilayers with perpendicular magnetic anisotropy. These were performed both in house, (with applied fields of up to 13 T), and at the Grenoble High Magnetic Field Laboratory (GHMFL), (with applied fields of up to 28 T). Earlier measurements on $DyFe_2/YFe_2$ multilayers, which order in-plane, revealed GMR as high as 12 % in an applied field of 23 T [12]. Using the model of Levy and Zhang (see chapter 2.4 and references therein) it was calculated that the GMR due to exchange springs in this case was 32 %. More recently, magneto-transport measurements have been performed in order to characterize both GMR and the AHE in $ErFe_2/YFe_2$ multilayers.

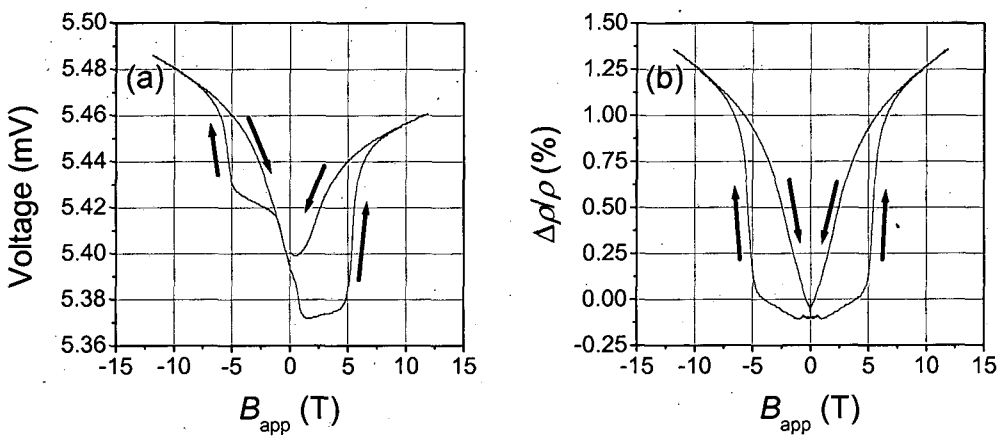

Figure 6.1. Voltage (a) and magnetoresistance (b) measured parallel to the applied current for the (110) multilayer [$ErFe_2$(50 Å)/YFe_2(150 Å)] × 20 at 100 K. The applied field is along the [110] growth direction. The arrows indicate the direction in which the field is being swept.

A block schematic of a typical magnetoresistance measurement is shown in Fig 3.4. Earlier measurements were made on un-patterned films and multilayers, with a simple contact arrangement (see Fig 3.5). Although the four contact measurement used was meant for measuring magnetoresistance, slight misalignment of the contacts resulted in a component of the Hall voltage being measured when the field is applied out of plane. This gives rise to pronounced asymmetry in the voltage loop. This can be seen in Fig 6.1 (a), which shows the voltage measured parallel to the applied current for the (110) multilayer [$ErFe_2$(50 Å)/YFe_2(150 Å)] × 20 at 100 K. This measurement was

made using a six contact arrangement as shown in Fig 3.5. The field was applied along the [110] direction, perpendicular to the film plane.

The result clearly shows the field asymmetry caused by the Hall voltage. To remove the Hall contribution, we make use of the fact that magnetoresistive effects are even in applied field, whereas both the ordinary and anomalous Hall effects are odd with respect to applied field. Once the even component of the data is obtained, as described in chapter 3, the GMR ratio can be determined. The result is shown in Fig 6.1 (b). The resistance initially decreases slightly, then increases slowly with the applied field. However, there is a rapid increase in resistance at an applied field of 4.4 T. This is caused by the formation of tight exchange springs in the YFe_2 layers that accompanies the reversal of the $ErFe_2$ layers (see chapter 4). The exchange springs act like domain walls with an effective thickness δ_w equal to the thickness required for the Fe moments to rotate by 180°. The effective domain wall width is calculated by doubling the thickness required for the magnetization to rotate by 90°, following the method of Gordeev *et al.* [12]. As the applied field is increased and the exchange springs wind tighter, δ_w decreases. This increases the resistance as described by the Levy and Zhang model of domain wall GMR [83]. The rather modest GMR of just over 1.5 % at 12 T indicates that δ_w is relatively large for this multilayer. In multilayers with thinner YFe_2 layers δ_w should be reduced.

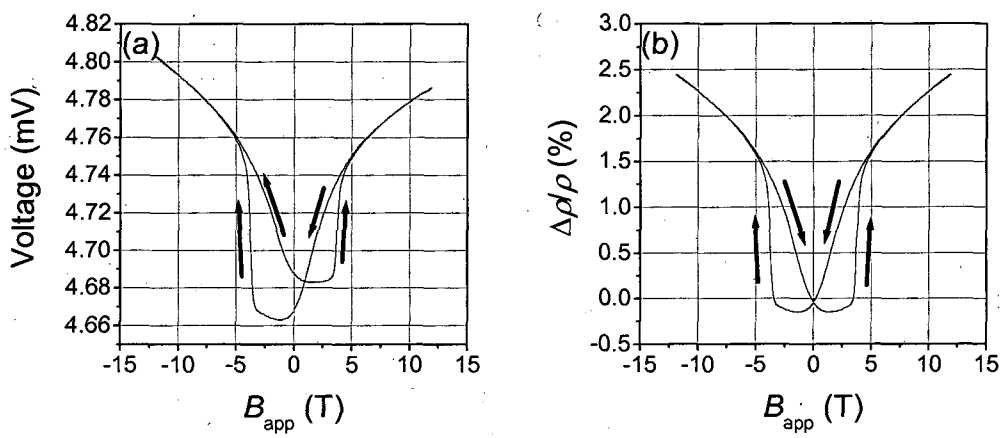

Figure 6.2. Voltage (a) and magnetoresistance (b) measured for the (110) multilayer [$ErFe_2$(50 Å)/YFe_2(100 Å)] × 27 at 100 K. The applied field is along the [110] direction. The arrows indicate the direction in which the field is being swept.

The magnetoresistance for the (110) multilayer [$ErFe_2$(50 Å)/YFe_2(100 Å)] × 27 at 100 K, again with the applied field along the [110] direction, can be seen in Fig 6.2. Once again, a slight decrease in resistance at low fields precedes a rapid rise in resistance at 3.5 T, associated with the formation of tight exchange springs in the soft layers. This multilayer shows just over 2.4 % GMR at 12 T. The higher GMR indicates that δ_w is smaller in the multilayer with thinner soft layers.

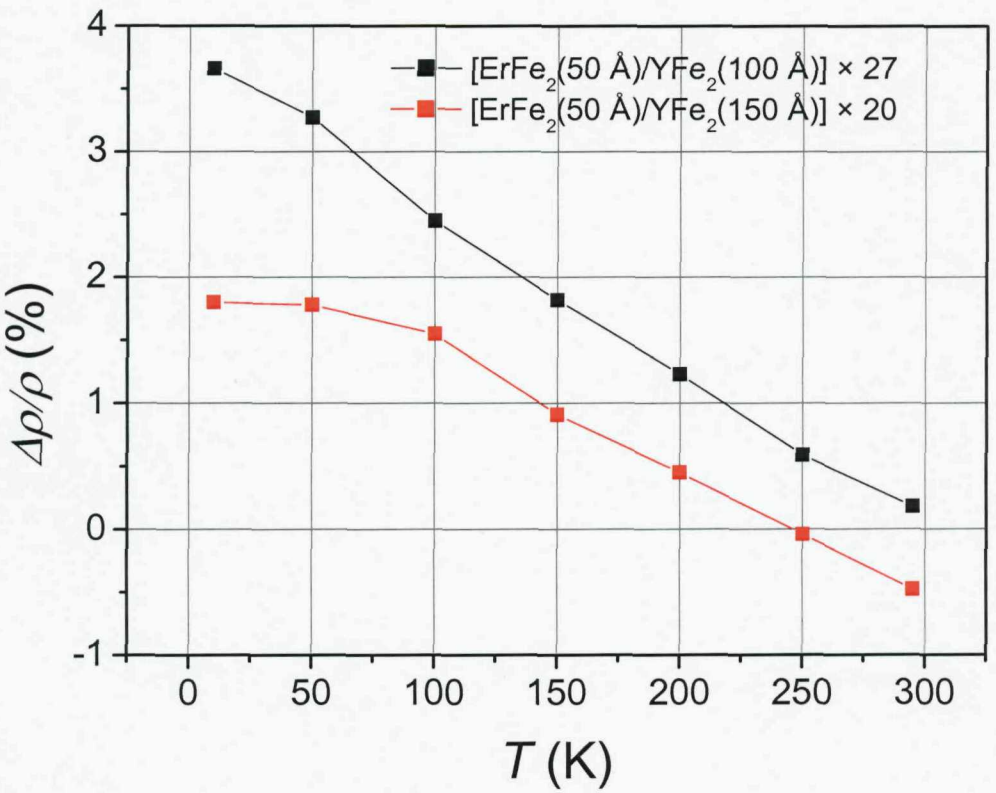

Figure 6.3. Magnetoresistance versus temperature for both [$ErFe_2$(50 Å)/YFe_2(100 Å)] × 27 and [$ErFe_2$(50 Å)/YFe_2(150 Å)] × 20. A field of 12 T is applied along the [110] direction.

The magnetoresistance at 12 T for un-patterned samples of [$ErFe_2$(50 Å)/YFe_2(150 Å)] × 20 and [$ErFe_2$(50 Å)/YFe_2(100 Å)] × 27 over a wide range of temperatures is shown in Fig 6.3. The applied field is along the [110] growth axis. The effect is made up of ordinary magnetoresistance (MR) as well as AMR and GMR. MR and AMR decrease with increasing resistivity in agreement with Kohler's rule (equation (2.6)). In addition, the temperature dependent scattering in Fe appears to be independent of

spin [128]. Therefore, the contribution to the resistivity from spin-dependent scattering in domain walls in Fe is considerably smaller at high temperatures than low temperatures [83]. This reduces the exchange spring GMR. The magnetoresistance of [$ErFe_2$(50 Å)/YFe_2(100 Å)] × 27 is larger than that of [$ErFe_2$(50 Å)/YFe_2(150 Å)] × 20 at all temperatures. This is due to the tighter domain walls in the thinner soft YFe_2 layers.

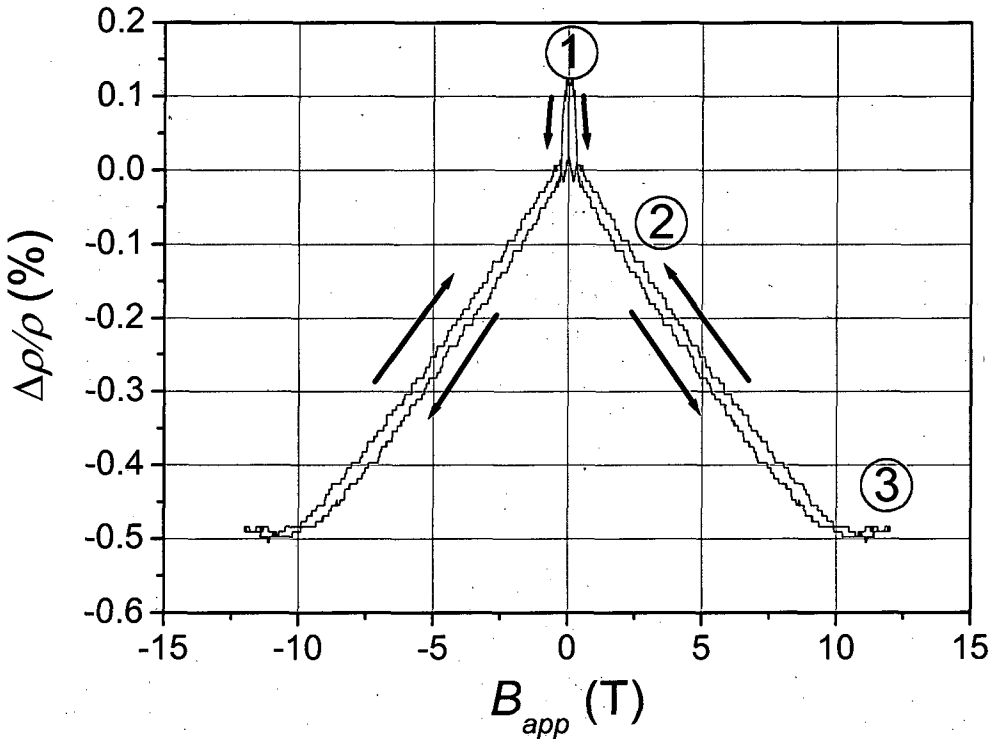

Figure 6.4. Magnetoresistance of [$ErFe_2$(50 Å)/YFe_2(150 Å)] × 20 at 295 K. The applied field is along the [110] direction. The arrows indicate the direction in which the field is being swept.

From an examination of Fig 6.3, it will be seen that the magnetoresistance of [$ErFe_2$(50 Å)/YFe_2(150 Å)] × 20 at 12 T changes sign at high temperature. This is due to the increase in magnetic order caused by the high field susceptibility discussed in chapter 2 (equation (2.17)). The increase in magnetic order reduces spin-disorder scattering and lowers the resistivity [129]. At high temperatures this effect overcomes the positive contribution from MR.

In Fig 6.4, the magnetoresistance for [$ErFe_2$(50 Å)/YFe_2(150 Å)] × 20 at 295 K can be seen. At low fields (point 1 on Fig 6.4) the resistivity peaks sharply before falling off.

This is most likely due to AMR. The resistivity then decreases with increasing applied field due to the high field susceptibility (point 2). At high fields (point 3), the hard layers switch irreversibly and exchange springs form in the soft layers. The resistivity then increases due to exchange spring GMR. At 295 K, exchange springs are starting to form at 12 T, the maximum applied field.

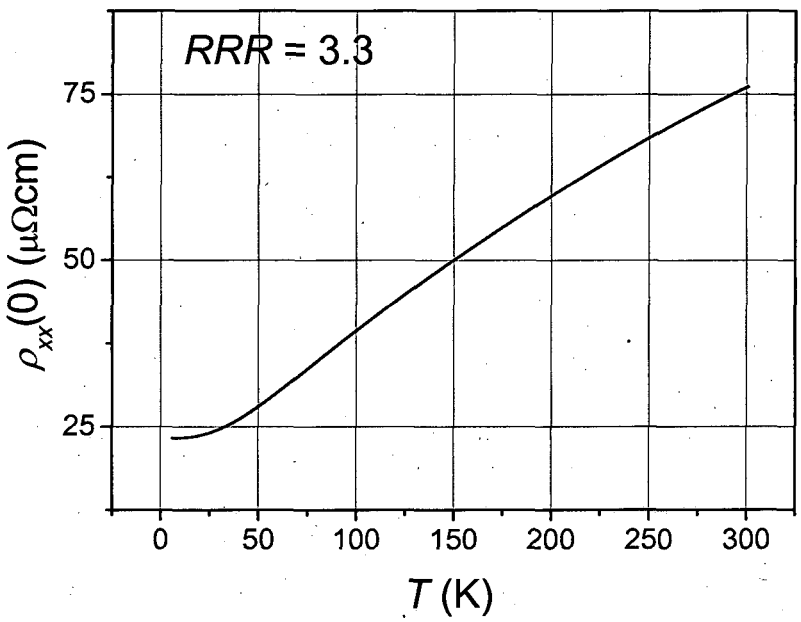

Figure 6.5. Resistivity against temperature for [$ErFe_2$(50 Å)/YFe_2(150 Å)] × 23. This data was obtained using a mechanically patterned sample.

Later experiments were performed on mechanically patterned samples, as described in chapter 3. One benefit of using patterned samples is that when the pattern geometry and film thickness are known, the resistivity of the material can be calculated. Fig 6.5 shows the zero field resistivity $\rho_{xx}(0)$ measured for [$ErFe_2$(50 Å)/YFe_2(150 Å)] × 23 for the temperature range 6 K – 300 K. In this case, the residual resistance ratio (RRR=R(300 K)/R(0 K)) is 3.3. Resistivity in metals is caused by scattering of the conduction electrons. At low temperatures the dominant mechanism is scattering from impurities in the regular lattice potential. Electron-phonon scattering is another source of resistance in metals. As the temperature increases, so does the number of phonons in the metal, leading to an increase in the resistivity. The relatively high value of residual resistivity in this material implies a large amount of impurity scattering. The error in the stoichiometry of the multilayers is roughly 2 %, and is the probable source of impurity scattering. In a magnetic material, electron scattering from disorder in the

spin system causes an anomalous increase in resistivity near the curie temperature T_C [4]. However, this does not occur for [$ErFe_2$(50 Å)/YFe_2(150 Å)] × 23 within the temperature range investigated.

In principal, patterning allows contacts to measure MR alone, with no component due to the AHE, and vice versa. In practice, the mechanical patterning methods used define the geometry of the multilayers has an accuracy of around ±20 %. Thus the resistance measurement thus still has a small odd component due to the Hall effect. This was removed by extracting the even component from the data. The pattern shown in Fig 3.6 also allowed simultaneous measurement of MR in two different directions. This is important in the case where the applied magnetic field is in-plane. If the field is applied along the direction of one of the current channels, then the MR data can be obtained both parallel and perpendicular to the field direction. These measurements are usually referred to as the longitudinal and transverse MR, respectively. In many cases reported here, the field was applied perpendicular to the film plane. In this case, the distinction between the MR in the two different legs is less clear. All measurements are of transverse MR, but it is possible that the resistance itself may be orientation dependent.

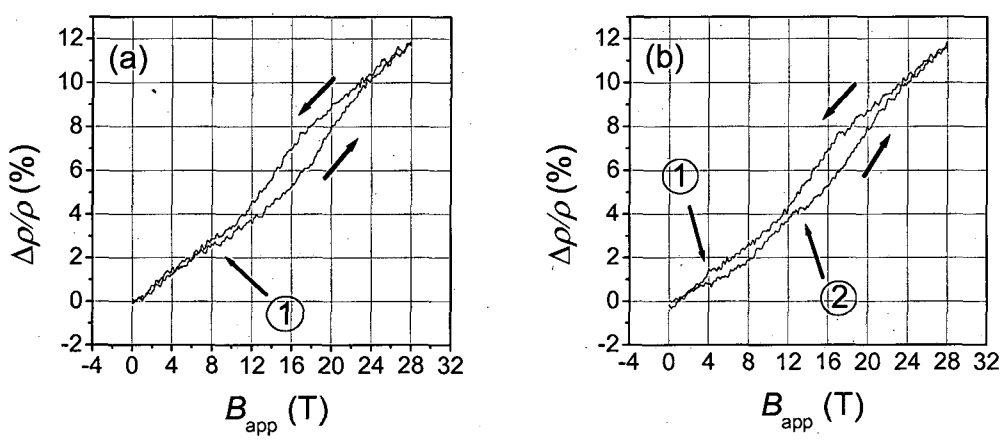

Figure 6.6. Magnetoresistance data for [$ErFe_2$(50 Å)/YFe_2(100 Å)] × 27 at 10 K with the applied field along an in-plane [1 $\bar{1}$1] axis. The multilayer is magnetized before the measurement with a large positive (a) or negative (b) field. The arrows indicate the direction in which the field is being swept.

When the field is applied along in plane directions the character of the GMR is very different, as is the magnetic reversal. Fig 6.6 (a,b) shows data collected for the (110) multilayer [$ErFe_2$(50 Å)/YFe_2(100 Å)] × 27 at 10 K, using a four contact arrangement on an un-patterned sample. The field is applied in the [$1\bar{1}1$] direction. The measured GMR at 28 T is 11.6(3) %. The GMR is not saturated even at 28 T. This indicates that the exchange springs are still winding up, forming effectively shorter domain walls. The effective domain wall width calculated by micro-magnetic modelling [130] is 18 Å at 28 T.

Unfortunately bulk magnetometry has not been performed for this sample with the field applied in the [$1\bar{1}1$] direction. However, the GMR data shows irreversible behaviour that gives information about the switching processes occurring within the multilayer. The result obtained after initially magnetizing the sample in a large positive field is shown in Fig 6.6 (a). A large open loop, indicating an irreversible response, begins at a field of 9(1) T. This corresponds to point 1 on Fig. 6.6 (a). The large error in the field value was caused by temperature drift during the experiment. This problem is noted in chapter 4. The open loop does not close, indicating that irreversible processes are still occurring even at fields as high as 28 T. Fig 6.6 (b) shows the result obtained after initially magnetizing the sample in a large negative field. In this case, there is an irreversible transition beginning at a field of 4(1) T, corresponding to point 1 of Fig 6.6 (b). The second transition is more difficult to observe in Fig 6.6 (b) as the voltage loop is already open. The loop does become noticeably wider at 13.5(5) T. Taken together the results in Fig 6.6 (a,b) provide information about the hysteresis loop of the material. At a small positive field the multilayer can be in different states, depending on its magnetic history. When the field is increased to 4 T the multilayer undergoes a transition into another state given that it had previously been magnetized in a large negative field. There is a transition to another state at a field of 13.5(5) T. Irreversible processes are still occurring in fields as high as 28 T. All of these transitions warrant further investigation.

6.2. Anomalous Hall effect in $REFe_2$ films and superlattices

These measurements use much the same equipment as the magnetoresistance measurements described above. The only difference in the measurement is that the measured Hall voltage is perpendicular to both the current through the sample and the applied field. As described in chapter 2, the Hall effect in these materials is expected to exhibit both an ordinary and an anomalous component. There are many different models of the AHE, however it is generally agreed that the effect is due to spin-orbit coupling combined with an appropriate scattering mechanism [96].

Magnetization and AHE data is shown in Fig 6.7 for $ErFe_2/YFe_2$ multilayers at 50 K (a,b) and 200 K (c,d). The magnetization data was collected for the (110) multilayer [$ErFe_2$(50 Å)/YFe_2(150 Å)] × 20. In all cases, the applied field of up to 12 T was directed along the [110] growth direction. The magnetometry results show the out of plane component of the magnetization, since it is the out of plane magnetization that generates the anomalous Hall effect. The transport data was collected in-house, for the multilayer [$ErFe_2$(50 Å)/YFe_2(150 Å)] × 23, using applied fields of up to 14 T. The spin configurations in these multilayers have been previously discussed in chapter 4. The magnetic reversal at 50 K (Fig. 6.7 (a)) is relatively simple. At high fields (see point 1), the Er magnetization points out of plane near to the applied field direction. As a result, there is a tight exchange spring in the soft YFe_2 layers. All moments are confined to the $[11\bar{1}]-[110]$ plane. Hereafter, we shall refer to this spin configuration as the *vertical spring configuration*. On reducing the field, the exchange springs in the soft layers unwind reversibly. One consequence of this unwinding is that for multilayers with sufficiently thick YFe_2 layers, the magnetization reverses before the applied field reaches zero. This occurs for [$ErFe_2$(50 Å)/YFe_2(150 Å)] × 20, as shown in Fig. 6.7 (a,b). Thus the conventionally defined coercivity of this multilayer is negative, a familiar feature of exchange spring multilayers with relatively thick soft layers [34]. For this multilayer at 50 K, the measured coercivity B_C is -0.30(3) T. On reducing the field to zero, the exchange spring unwinds completely, and the multilayer enters an AF configuration with the YFe_2 and $ErFe_2$ net magnetizations opposing each other. This corresponds to point 2 on Fig. 6.7 (a,b). At this point, the out of plane component of the Fe magnetization is a maximum, giving rise to the largest value of

the AHE (Fig. 6.7 (b)).When the applied field reaches a sufficiently high negative value, the hard $ErFe_2$ layer switches irreversibly to point close to the now negative field direction. Now the magnetic moments are in the reverse *vertical spring configuration*. This corresponds to point 3 on Fig. 6.7 (a,b). The field required to switch the hard layers at 50 K is 5.5(2) T. After the switch, the hard Er moments point roughly in the direction of the applied field. This is accompanied by the formation of a tight exchange spring in the YFe_2 layer, leading to an increase in overall magnetization, but a diminution in the magnitude of the overall Fe moment and hence the AHE. At low temperatures, the magnetic reversal of the multilayer is relatively simple. In summary, the moments never leave the $[11\bar{1}]-[110]$ plane, and the magnetic loop is characterized by just one irreversible transition at high fields.

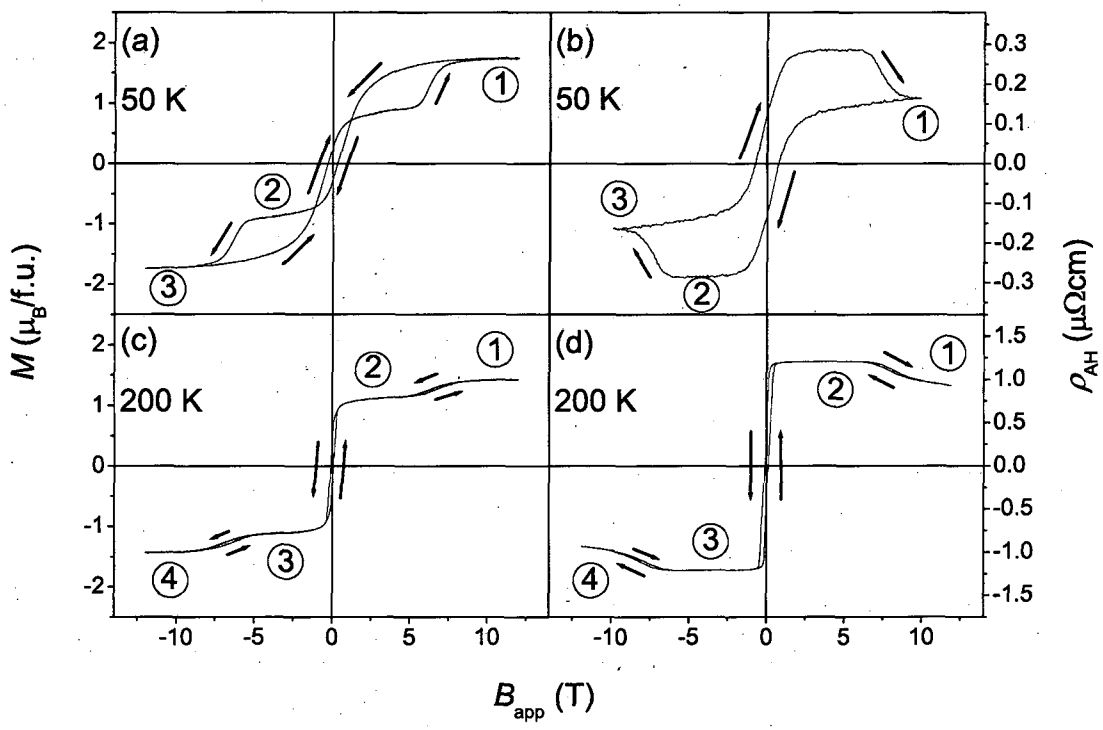

Figure 6.7. Experimental results at 50 K (a,b) and 200 K (c,d). The left hand panels (a,c) show the magnetization and the right hand panels (b,d) show the anomalous Hall effect. The arrows show the direction in which the field is being swept.

At 200 K (Fig. 6.7 (c,d)) the magnetic reversal process is more complicated, involving more than one irreversible switch. At high fields (point 1), the average $ErFe_2$ magnetization lies almost perpendicular to the applied field, close to one of the in-plane <111>-axes *e.g.* the $[\bar{1}\,1\,\bar{1}]$-axis. Concomitantly, there is a tight exchange spring

in the soft YFe_2 layers. This is the *spin-flop configuration* described in chapter 4. Here the Er moments take advantage of one of the four in-plane magneto-crystalline local minima. Note that all the moments are confined, primarily, to the $[\bar{1}\,1\,\bar{1}]$-[110] plane (c.f. the $[11\,\bar{1}]-[110]$ plane at low temperatures). However, as the field is decreased below about 6 T the average the $ErFe_2$ magnetization rotates both *downwards and sideways* to the $[\bar{1}\,\bar{1}\,\bar{1}]-[\bar{1}\,\bar{1}\,0]$ plane, roughly opposite to the applied field. This irreversible rotation causes the first step in the hysteresis loop. At this point (2) the multilayer reverts to a *vertical spring configuration*. However, this spin configuration differs from the low temperature version in that the Fe moments are now more dominant. The Fe moments are aligned with the applied field, which generates a large AHE (Fig. 6.7 (d)). Further, on reducing the field to -0.4(1) T, the $ErFe_2$ layers switch again, pointing out of plane nearly opposite the applied field direction, but still in the $[\bar{1}\,\bar{1}\,0]-[\bar{1}\,\bar{1}\,\bar{1}]$ plane. This constitutes the second irreversible step, which can be described simply as simple switching of the soft YFe_2 magnetization. The multilayer is now in the reverse *vertical spring configuration*, i.e. with the moments in the opposite direction. This too generates a large AHE, but with the opposite sign to that at point 2. Finally, when the field is reduced to below -8 T (point 4), the Er magnetization rotates to take advantage of an in-plane <111> axis taking up the *reverse spin-flop configuration*. This spin configuration has less Fe aligned along the field direction and so gives rise to a smaller AHE signal.

Fig. 6.8 shows calculated hysteresis curves for 50 K (a,b) and 200 K (c,d). The modelled hysteresis curves were calculated by numerical methods, using the 1-3D magnetic exchange spring model of Bowden *et al.* [130], the Er anisotropy parameters of Martin *et al.* [70] and the first order strain parameter of Bowden *et al.* [106]. The left hand panels of Fig. 6.8 (a,c) show the total magnetization of the multilayer, whereas the right hand panels (b,d) show the calculated Fe magnetization. It will be seen that there is a high degree of correlation between the AHE and the Fe magnetization curve at both 50 K (b) and 200 K (d). Further, the agreement between the experimental and modelled magnetization data is very good.

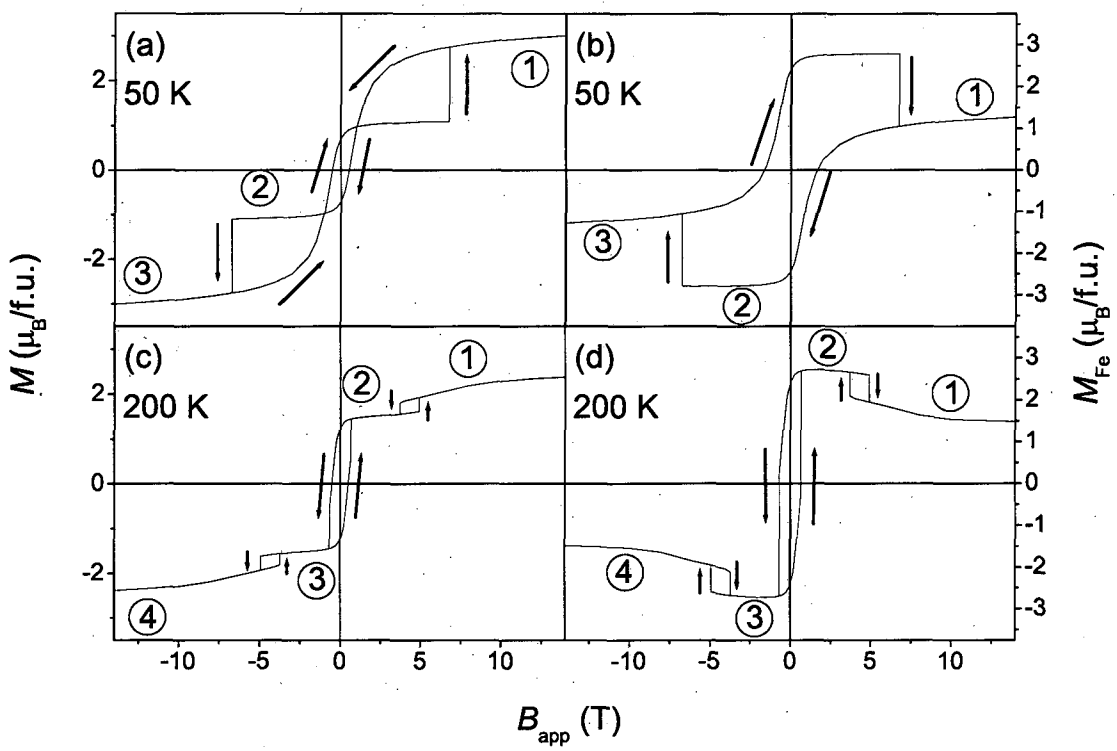

Figure 6.8. Calculated results at 50 K (a,b) and 200 K (c,d). The left hand panels (a,c) show the full magnetization curve and the right hand panels (b,d) show the component of the magnetization due to the Fe alone. The arrows show the direction in which the field is being swept.

The above results show that AHE measurements in $ErFe_2/YFe_2$ multilayers, can be used as a simple method for quantifying the response of both Fe and Er to an applied field. In many ways the technique is similar to polar magneto-optical Kerr effect (MOKE), which is also sensitive to the transition metal sub-lattice magnetization. Indeed, longitudinal MOKE studies performed in-house on $DyFe_2/YFe_2$ multilayers have yielded similar results to those described above. We should also remark that similar results have been obtained for $DyFe_2/YFe_2$ multilayers, using an element specific technique: X-ray Magnetic Circular Dichroism (XMCD) [35]. However, the AHE measurements described here can be performed relatively cheaply in-house, thereby avoiding the need for expensive synchrotron facilities.

The anomalous Hall coefficient, R_s, takes the form of equation (2.15). It has terms both linear and quadratic in the standard resistivity ρ. The linear term is normally attributed to a mechanism known as skew scattering and the quadratic term to another mechanism, the quantum mechanical side jump proposed by Berger in the 1970's

[99]. Experimental AHE data is often fitted by a single power expression $\rho_{AH} \propto \rho_{xx}^{n}$ (equation (2.16)), where $n = 1$ corresponds to skew scattering, $n = 2$ corresponds to the side jump and $1 \leq n \leq 2$ indicates a superposition of these two mechanisms. The value of ρ_{AH} is usually obtained from Hall effect data by removing the linear contribution of the OHE and high field susceptibility as shown in Fig 3.7. These components have been removed from the data shown in Fig 6.7, leaving the anomalous contribution only. However, the response of $ErFe_2/YFe_2$ multilayers to an applied field is more complex than the simple response shown in Fig 3.7. The AHE couples mainly to the Fe magnetization. As such, it is a maximum when the Fe moments in both the hard and soft layers point out of plane. This occurs when the multilayer enters the AF configuration at low temperatures or the *vertical spring configuration* at high temperatures. These spin configurations occur at applied fields significantly below those required to saturate the magnetization. The determination of ρ_{AH} from the Hall effect data is shown in Fig 6.9 for [$ErFe_2$(50 Å)/YFe_2(150 Å)] × 23 at 295 K (a) and 70 K (b).

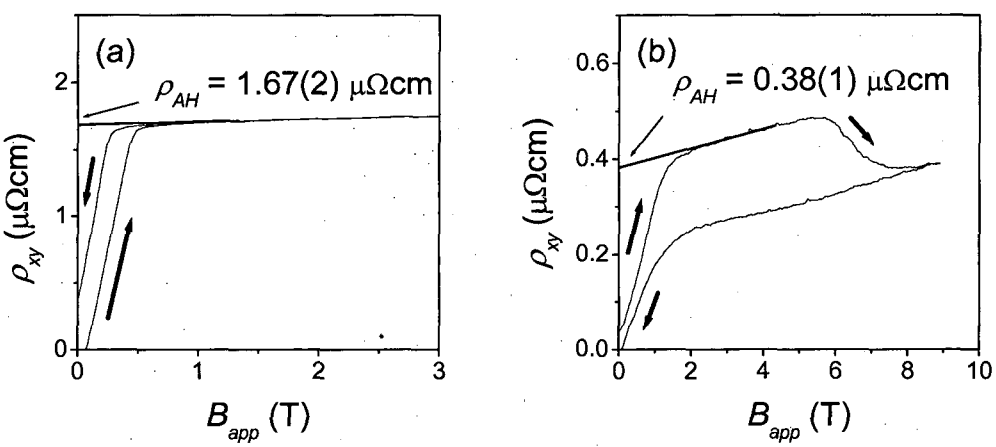

Figure 6.9. Determination of ρ_{AH} from the Hall data for [$ErFe_2$(50 Å)/YFe_2(150 Å)] × 23 at 295 K (a) and 70 K (b).

The variation of ρ_{AH} with the standard resistivity ρ_{xx} at zero field is shown in Fig 6.10. The black line corresponds to the experimental data and the red line a single power fit of the form of equation (2.16). The value of n obtained from this data is 1.83, within the expected range for most models of the AHE. The fit shown in Fig

6.10 is $\rho_{AH} = 6.62\times10^{-4}\rho_{xx}^{1.83}$. The fit appears best at low temperatures (low resistivity). At high temperatures (high resistivity), the data appears to be more linear, i.e. n is closer to 1. This is surprising as the side jump mechanism ($n = 2$) is expected to dominate the skew scattering in a metal at high temperatures. But this surprising result could be due to the different spin configurations that occur at temperatures above and below T_{CO}, giving rise to different values of the perpendicular magnetization of Fe. Another possible explanation is that the Er magnetization also contributes to the AHE. In this respect we note the Er magnetization falls off more quickly with temperature than the Fe magnetization (Fig 4.1 (a) and Fig 5.2 (a)) and so would generate a smaller Hall effect at higher temperatures.

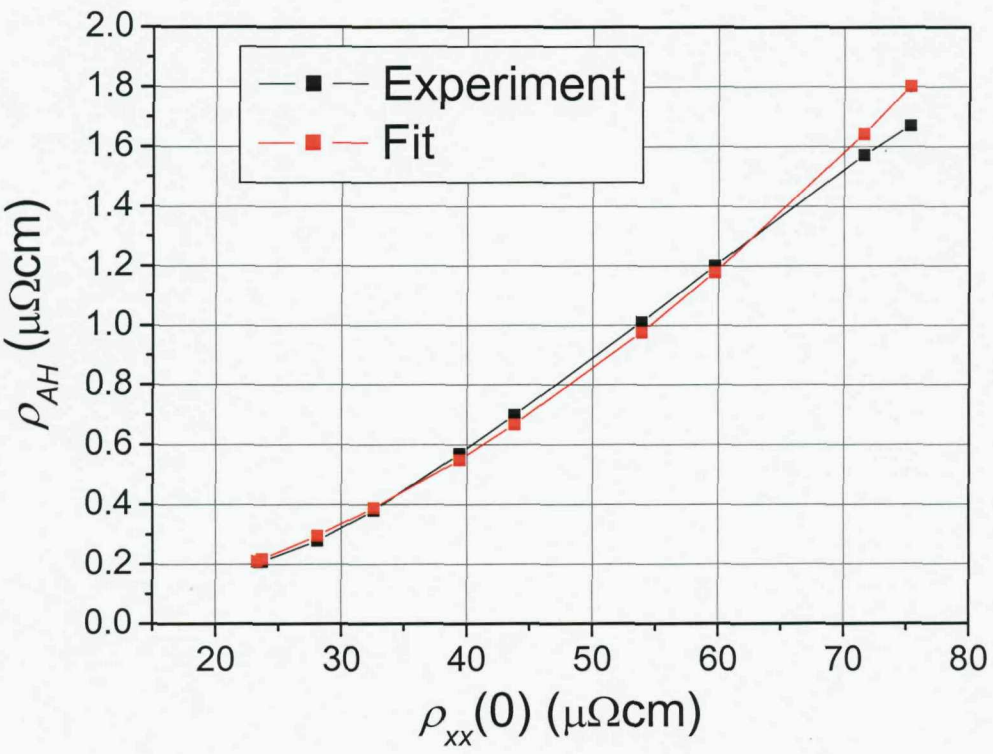

Figure 6.10. Variation of anomalous Hall resistivity with standard resistivity for [$ErFe_2$(50 Å)/YFe_2(150 Å)] × 23. The experimental results (black squares) are compared with a single power fit (red squares).

6.3. Conclusions

Magneto-transport measurements have been performed on $ErFe_2$ films and $ErFe_2/YFe_2$ multilayers. These were performed both in house, with applied fields of up to 12 T, and at Grenoble High Magnetic Field Laboratory (GHMFL), with applied fields of up to 28 T. Both GMR and AHE have been studied in detail.

GMR measurements have been performed at a range of temperatures, with the applied field both in plane and out of plane. The formation of exchange springs in the multilayers gives rise to a large increase in GMR, which can be understood in terms of the Levy and Zhang model of domain wall magnetoresistance [83]. At a temperature of 10 K, with the field applied in plane, there are still irreversible processes occurring at applied fields exceeding 20 T. GMR of 11.6(3) % has been seen in fields of 28 T. Even at such high fields, it is not saturated.

AHE and magnetization data have been presented and discussed for a YFe_2 dominated (110) MBE-grown $ErFe_2/YFe_2$ multilayer. The experimental data has been compared with model calculations of both the bulk and Fe sub-lattice magnetizations. The qualitative agreement between theory and experiment is good. In particular, the results show that the AHE closely follows the Fe sub-lattice magnetization. In this regard, the technique is similar to polar MOKE. Thus the AHE offers a convenient and simple method for the characterization of the magnetization processes in magnetic superlattices. In particular, it has been demonstrated that the AHE results at high temperatures (200 K) mirror the complex magnetic reversal mechanisms associated with transitions between *vertical* and *spin-flop spring configurations*. Finally, the variation of the anomalous Hall resistivity as a function of the standard resistivity of the multilayer has also been investigated. The results are consistent with standard models of the AHE.

Chapter 7. Summary

The aim of this work has been to study the magnetic reversal and transport properties of MBE grown Laves Phase $REFe_2$ materials, in particular $ErFe_2$ films, $ErFe_2/YFe_2$ multilayers and $ErFe_2/YFe_2/DyFe_2/YFe_2$ multilayers with competing anisotropies. This has been accomplished primarily through bulk magnetometry and magneto-transport measurements. Extensive micromagnetic modelling work has also been performed in a parallel project by Jurgen Zimmerman, in the Computational Engineering and Design Group, School of Engineering Sciences. The materials display effects including negative coercivity, spin-flop transitions and the anomalous Hall effect.

Bulk magnetization measurements of $ErFe_2$ films and $ErFe_2/YFe_2$ multilayers have been presented and discussed. $ErFe_2/YFe_2$ multilayers are useful model systems in which to study perpendicular exchange springs. The Er moment and anisotropy both fall off quickly with increasing temperature, leading to significant differences in the response to a magnetic field. Both (110) and (111) grown multilayers have been studied. The magnetocrystalline easy axes of $ErFe_2$ are the <111> body diagonals. In the case of (110) $ErFe_2$ multilayers, the magneto-elastic strain term ($b_2\varepsilon_{xy}$) (see Mougin *et al.* [51, 71]) favours an easy axis nearly along the out of plane <111> axes, roughly 35° from the growth axis and in the $[11\bar{1}]-[110]$ plane. In the case of (111) $ErFe_2$ multilayers, both the magneto-elastic strain term and magnetocrystalline anisotropy favour an easy axis along the out of plane <111> directions, perpendicular to the film plane.

At low temperatures the magnetic reversal of all the superlattices studied is dictated by the hard layers. At high fields the $ErFe_2$ magnetization points out of plane, close to the applied field direction, and there is a tight exchange spring in the soft YFe_2 layers. As the field is reduced the exchange springs gradually unwind. This can result in negative coercivity in multilayers with sufficiently thick soft YFe_2 layers. The magnetization curve of YFe_2 dominated multilayers is largely reversible at low temperatures. But at a large negative field, the hard layers switch to point out of plane

close to the new applied field direction. This irreversible transition is accompanied by the formation of tight exchange springs in the soft layers. In summary, at low temperatures the magnetic loop is characterized by just one irreversible transition at high fields

At high temperatures significant changes occur in the character of the hysteresis loops of YFe_2 dominated multilayers. There are now three irreversible steps in the magnetic reversal and the coercivity becomes positive. At suitably high fields the hard layer spins point at right angles to the applied field. This is called an exchange spring driven multilayer spin-flop. As the field is reduced the hard layer spins switch irreversibly to point out of plane opposite the applied field. The soft layer magnetization is along the field direction. At a modest negative field, both the hard layer magnetization and soft layer magnetization reverse. Finally, at a large negative field, the hard layer spins once again switch to point in plane. The cross over between the low and high temperature behaviour happens at the temperature T_{CO}. T_{CO} depends on the multilayer composition and is lower for multilayers with thicker soft layers. It can be thought of as the temperature at which the soft layers begin to dominate the response of the multilayer to a magnetic field. The hysteresis curves of a typical $ErFe_2/YFe_2$ multilayer at temperatures both above and below T_{CO} are shown in Fig 4.6 (a,b).

The magnetic behaviour of $ErFe_2/YFe_2/DyFe_2/YFe_2$ multilayers is even more varied. The hard magnetic materials $ErFe_2$ and $DyFe_2$ have different magnetic anisotropies. The interaction between the two different hard materials with the soft YFe_2 layers and with each other has been investigated through bulk magnetometry and micromagnetic modelling. These techniques reveal a rich variety of switching processes. Varying the temperature or the thickness of the soft layers has a drastic effect on the magnetic reversal of the multilayers. By performing micromagnetic modelling for a set of multilayers with different soft layer thicknesses and at different temperatures, a phase diagram of switching processes is built up, as shown in Fig 5.8.

To investigate the effect of varying the temperature, magnetometry data was collected for the multilayer [$ErFe_2$(100 Å)/YFe_2(200 Å)/$DyFe_2$(40 Å)/ YFe_2(200 Å)] × 10 within a temperature range of 10 - 320 K. This multilayer has relatively thick soft layers. Micromagnetic modelling was performed for temperatures in the range 10 -

350 K. At low temperatures the two different hard layers switch independently of each other. The soft layer magnetization points opposite the hard layer magnetization at the interfaces and reorients throughout the soft layer. We call this reversal mechanism independent switching. At 200 K the $ErFe_2$ layers switch via an in plane direction, but the switching behaviour of the $DyFe_2$ layers is the same as for lower temperatures. We call this behaviour the $ErFe_2$ spin-flop. As the temperature is raised further to 300 K, the soft YFe_2 layers dominate the magnetic reversal of the multilayer, and both the $ErFe_2$ and $DyFe_2$ layers reverse before the applied field. We call this switching behaviour YFe_2 dominance.

In order to investigate the effect of varying the soft layer thickness, micromagnetic modelling was performed for multilayers with different YFe_2 layer thicknesses, but always with $ErFe_2$ and $DyFe_2$ layer thicknesses of 100 Å and 40 Å, respectively. For multilayers with relatively thin YFe_2 layers, a new switching mode is found in which the $ErFe_2$ magnetization is significantly exchange coupled to the $DyFe_2$ magnetization. The exchange between the different RE compounds is strong enough to force the $ErFe_2$ magnetization to switch via the $[\bar{1}10]$ direction, a hard axis for $ErFe_2$. We call this the coupled switching regime. It is predicted to exist for multilayers with thin YFe_2 layers at higher temperatures, where the exchange energy is enough to overcome the Er anisotropy. The switching processes of $ErFe_2/YFe_2/DyFe_2/YFe_2$ multilayers, as shown in the phase diagram, are even more complex than those described in Chapter 4 for $ErFe_2/YFe_2$ multilayers.

Magneto-transport measurements have been performed on $ErFe_2$ films and $ErFe_2/YFe_2$ multilayers. These were performed both in house, with applied fields of up to 12 T, and at Grenoble High Magnetic Field Laboratory (GHMFL), with applied fields of up to 28 T. Both the anomalous Hall effect and exchange spring GMR have been studied in detail. GMR in the multilayers is understood in terms of the Levy and Zhang model of domain wall magnetoresistance [83]. In this model, the inability of the electron spin to track the reorientation of magnetization in a domain wall mixes current channels of opposite spin. This effect increases spin dependent scattering from impurity centres. Exchange springs in the multilayers act like domain walls. As the

applied field is increased, the exchange springs are wound tighter, thereby decreasing the effective domain wall width and so increasing the resistance.

GMR as high as 11.6(3) % has been obtained for the (110) multilayer [$ErFe_2$(50 Å)/YFe_2(100 Å)] × 27 at a temperature of 10 K and field of 28 T applied in plane, as shown in Fig 6.6 (a,b). The GMR is not saturated, even at 28 T. This indicates that the exchange springs are still winding tighter, forming effectively shorter domain walls. The GMR shows irreversible behaviour that gives information about the switching processes occurring in the multilayers. The data is irreversible even at fields exceeding 20 T.

AHE data has also been obtained for $ErFe_2/YFe_2$ multilayers. The variation of the anomalous Hall resistivity ρ_{AH} with standard resistivity ρ_{xx} of the multilayer has been investigated. The experimental data has been fitted with a single power expression $\rho_{AH} = 6.62 \times 10^{-4} \rho_{xx}^{1.83}$, as shown in Fig 6.10. This is consistent with standard models of the AHE. AHE data reveals the temperature dependence of the magnetic reversal processes. It is clear that the AHE couples mainly to the Fe magnetization in these materials. The AHE data have been complemented with modelled hysteresis curves, calculated by numerical methods, using the 1-3D magnetic exchange spring model of Bowden *et al.* [130], the Er anisotropy parameters of Martin *et al.* [70] and the first order strain parameter of Bowden *et al.* [106]. There is a high degree of correlation between the AHE and the Fe magnetization curves at both 50 K and 200 K, as illustrated in Fig 6.7 and Fig 6.8. The results show that AHE measurements can be used as a simple method for quantifying the response of both Fe and Er to an applied field. This information cannot be obtained by bulk magnetometry alone.

References

[1] J. W. M. DuMond, and J. P. Youtz, Phys. Rev. **48**, 703 (1935).
[2] M. Sawicki *et al.*, Appl. Phys. Lett. **77**, 573 (2000).
[3] R. F. C. Farrow, C. H. Lee, and S. S. P. Parkin, IBM J. Res. Dev. **34**, 903 (1990).
[4] R. C. O'Handley, *Modern Magnetic Materials: Principles and Applications* (John Wiley & Sons, New York, 2000).
[5] Y. Kaneko, IEEE Trans. Magn. **36**, 3275 (2000).
[6] A. E. Clark, and H. S. Belson, Phys. Rev. B **5**, 3642 (1972).
[7] M. R. J. Gibbs, E. W. Hill, and P. J. Wright, J. Phys. D **37**, R237 (2004).
[8] D. Suess *et al.*, J. Magn. Magn. Mater. **290**, 551 (2005).
[9] K. Dumesnil *et al.*, Phys. Rev. B **62**, 1136 (2000).
[10] E. E. Fullerton, J. S. Jiang, and S. D. Bader, J. Magn. Magn. Mater. **200**, 392 (1999).
[11] J.-M. L. Beaujour, in *Department of Physics and Astronomy* (University of Southampton, Southampton, 2003), p. 161.
[12] S. N. Gordeev *et al.*, Phys. Rev. Lett. **87**, 186808 (2001).
[13] H. Fritzsche *et al.*, Phys. Rev. B **77**, 054423 (2008).
[14] K. Wang *et al.*, Phys. Stat. solidi (a) **203**, 3831 (2006).
[15] K. Wang *et al.*, App. Phys. A **86**, 325 (2007).
[16] K. Wang *et al.*, J. All. Comp. **440**, 23 (2007).
[17] M. R. J. Gibbs, J. Magn. Magn. Mater. **290-291**, 1298 (2005).
[18] A. Ludwig, and E. Quandt, J. Appl. Phys. **87**, 4691 (2000).
[19] C. T. Pan, and S. C. Shen, J. Magn. Magn. Mater. **285**, 422 (2005).
[20] T.-S. Chin, J. Mag. Magn. Mater. **209**, 75 (2000).
[21] D. Suess *et al.*, Appl. Phys. Lett. **87**, 12504 (2005).
[22] R. H. Victora, and X. Shen, IEEE Trans. Magn. **41**, 537 (2005).
[23] A. J. Rosengart *et al.*, J. Mag. Magn. Mater. **293**, 633 (2005).
[24] J. F. Herbst, Rev. Mod. Phys **63**, 819 (1991).
[25] E. F. Kneller, E. F. Kneller, and R. Hawig, IEEE Trans. Magn. **27**, 3588 (1991).
[26] J. M. D. Coey, and R. Skomski, Physica Scripta **T49**, 315 (1993).
[27] J. R. Davis, *AMS Handbook. Properties and selection : nonferrous alloys and special-purpose materials 10th ed* (ASM International, Materials Park, OH, 1990), Vol. 2.
[28] R. Skomski, and J. M. D. Coey, IEEE Trans. Magn. **29**, 2860 (1993).
[29] R. Skomski, and J. M. D. Coey, Phys. Rev. B **48**, 15812 (1993).
[30] E. E. Fullerton *et al.*, Phys. Rev. B **58**, 12193 (1998).
[31] K. Kang *et al.*, J. Appl. Phys. **98**, 113906 (2005).
[32] Y. Choi *et al.*, Appl. Phys. Lett. **91**, 022502 (2007).
[33] Y. Choi *et al.*, J. Appl. Phys. **103**, 07E132 (2008).
[34] J.-M. L. Beaujour *et al.*, Appl. Phys. Lett. **78**, 964 (2001).
[35] K. Dumesnil *et al.*, J. Appl. Phys. **95**, 6843 (2004).
[36] M. R. Fitzsimmons *et al.*, Phys. Rev. B **73**, 134413 (2006).
[37] S. M. Watson *et al.*, Appl. Phys. Lett. **92**, 202507 (2008).
[38] S. Mangin *et al.*, Phys. Rev. B **58**, 2748 (1998).

[39] J. Nogues, and I. K. Schuller, J. Mag. Magn. Mater. **192**, 203 (1999).
[40] O. Cugat *et al.*, IEEE Trans. Magn. **39**, 3607 (2003).
[41] A. E. Clark, *Handbook on the Physics and Chemistry of Rare Earths* Amsterdam, 1979), Vol. 2.
[42] R. D. Greenough *et al.*, J. Mag. Magn. Mater. **101**, 75 (1991).
[43] F. Claeyssen *et al.*, J. All. Comp. **258**, 61 (1997).
[44] S. N. Piramanayagam, J. Appl. Phys **102**, 011301 (2007).
[45] D. Weller, and A. Moser, IEEE Trans. Magn. **35**, 4423 (1999).
[46] M. F. Doerner *et al.*, IEEE Trans. Magn. **36**, 43 (2000).
[47] J.-U. Thiele, S. Maat, and E. E. Fullerton, Appl. Phys. Lett. **82**, 2859 (2003).
[48] E. C. Stoner, and E. P. Wohlfarth, Philos. Trans. R. Soc. A **240**, 599 (1948).
[49] G. Kai-Zhong, and H. N. Bertram, IEEE Trans. Magn. **38**, 3675 (2002).
[50] J. P. Wang *et al.*, IEEE Trans. Magn. **39**, 1930 (2003).
[51] A. Mougin *et al.*, Phys. Rev. B **59**, 5950 (1999).
[52] R. Stuart, and W. Marshall, Phys. Rev. **120**, 353 (1960).
[53] C. Zener, Phys. Rev. **81**, 440 (1951).
[54] C. Zener, Phys. Rev. **82**, 403 (1951).
[55] C. Zener, Phys. Rev. **83**, 299 (1951).
[56] C. Zener, Phys. Rev. **85**, 324 (1952).
[57] M. A. Ruderman, and C. Kittel, Phys. Rev. **96**, 99 (1954).
[58] T. Kasuya, Prog. Theor. Phys. **16**, 45 (1956).
[59] K. Yosida, Phys. Rev. **106**, 893 (1957).
[60] M. B. Stearns, Phys. Rev. **129**, 1136 (1963).
[61] M. B. Stearns, Phys. Rev. **147**, 439 (1966).
[62] M. B. Stearns, Phys. Rev. B **4**, 4069 (1971).
[63] M. B. Stearns, Phys. Rev. B **4**, 4081 (1971).
[64] M. B. Stearns, Phys. Rev. B **8**, 4383 (1973).
[65] M. B. Stearns, in *Physics Today*1978), pp. 34.
[66] I. A. Campbell, J. Phys. F **2**, L47 (1972).
[67] H. B. Callen, and E. Callen, J. Phys. Chem. Solids **27**, 1271 (1966).
[68] U. Atzmony, and M. P. Dariel, Phys. Rev. B **13**, 4006 (1976).
[69] G. Aubert, J. Appl. Phys **39**, 504 (1968).
[70] K. N. Martin *et al.*, J. Phys. Cond. Matter. **18**, 459 (2006).
[71] A. Mougin *et al.*, Phys. Rev. B **62**, 9517 (2000).
[72] A. A. Zhukov *et al.*, J. Mag. Magn. Mater. **270**, 312 (2004).
[73] G. J. Bowden *et al.*, Journal of Physics: Condensed Matter **20**, 285226 (2008).
[74] E. Goto *et al.*, J. Appl. Phys **36**, 2951 (1965).
[75] G. J. Bowden *et al.*, J. Phys. Cond. Matter. **12**, 9335 (2000).
[76] M. Kohler, Ann. Phys. **424**, 211 (1938).
[77] G. Binasch *et al.*, Phys. Rev. B **39**, 4828 (1989).
[78] M. N. Baibich *et al.*, Phys. Rev. Lett. **61**, 2472 (1988).
[79] GerstnerEd, Nat Phys **advanced online publication** (2007).
[80] A. Cho, Science **318**, 179 (2007).
[81] J. F. Gregg *et al.*, Phys. Rev. Lett. **77**, 1580 (1996).
[82] M. Viret *et al.*, Phys. Rev. B **53**, 8464 (1996).
[83] P. M. Levy, and S. Zhang, Phys. Rev. Lett. **79**, 5110 (1997).
[84] E. H. Hall, Philos. Mag. **10**, 301 (1880).
[85] E. H. Hall, Philos. Mag. **12**, 157 (1881).
[86] A. Gerber *et al.*, J.Mag.Magn.Mater. **242-245**, 90 (2002).

[87] N. H. Duc, N. T. M. Hong, and J. Teillet, J. Mag. Magn. Mater. **316**, e269 (2007).
[88] S. Nakagawa, I. Sasaki, and M. Naoe, J. Appl. Phys. **91**, 8354 (2002).
[89] J. Lindemuth, and B. Dodrill, IEEE Trans. Magn. **40**, 2191 (2004).
[90] R. Karplus, and J. M. Luttinger, Phys. Rev. **95**, 1154 (1954).
[91] F. D. M. Haldane, Phys. Rev. Lett. **93**, 206602 (2004).
[92] J. Ye *et al.*, Phys. Rev. Lett. **83**, 3737 (1999).
[93] Y. Yao *et al.*, Phys. Rev. Lett. **92**, 037204 (2004).
[94] J. Kotzler, and W. Gil, Phys. Rev. B **72**, 060412(R) (2005).
[95] A. Gerber *et al.*, Phys. Rev. B **69**, 224403 (2004).
[96] C. M. Hurd, *The Hall Effect in Metals and Alloys* (Plenum Press, New York, 1972).
[97] A. W. Smith, and R. W. Sears, Phys. Rev. **34**, 1466 (1929).
[98] E. M. Pugh, Phys. Rev. **36**, 1503 (1930).
[99] L. Berger, Phys. Rev. B **2**, 4559 (1970).
[100] P. Xiong *et al.*, Phys. Rev. Lett. **69**, 3220 (1992).
[101] S. M. Durbin, J. E. Cunningham, and C. P. Flynn, J. Phys. F **12**, L75 (1982).
[102] S. M. Durbin *et al.*, J. Phys. F **11**, L223 (1981).
[103] J. E. Cunningham, and C. P. Flynn, J. Phys. F **15**, L221 (1985).
[104] P. Sonntag *et al.*, Phys. Rev. B **49**, 2869 (1994).
[105] M. J. Bentall *et al.*, J. Phys. Cond. Matter. **15**, 6493 (2003).
[106] G. J. Bowden *et al.*, J. Phys. Cond. Matter. **18**, 5861 (2006).
[107] M. Springford, J. R. Stockton, and W. R. Wampler, J. Phys. E. **4**, 1036 (1971).
[108] J. A. Gerber, W. L. Burmester, and D. J. Sellmyer, Rev. Sci. Instrum. **53**, 691 (1982).
[109] S. Foner, Rev. Sci. Instrum. **27**, 548 (1956).
[110] S. Foner, Rev. of Sci. Instrum. **30**, 548 (1959).
[111] M. Sawicki *et al.*, J. Appl. Phys. **87**, 6839 (2000).
[112] K. N. Martin *et al.*, J. Appl. Phys. **101**, 09K511 (2007).
[113] K. N. Martin *et al.*, Appl. Phys. Lett. **89**, 132511 (2006).
[114] V. Oderno *et al.*, J. Cryst. Growth **165**, 175 (1996).
[115] M. Sawicki *et al.*, Phys. Rev. B **62**, 5817 (2000).
[116] Z. Tun *et al.*, J. Appl. Phys. **76**, 7075 (1994).
[117] M. J. Donahue, and D. G. Porter, *OOMMF Users Guide* (NIST, Gaithersburg, MD, 1999).
[118] V. Oderno *et al.*, Phys. Rev. B **54**, 375 (1996).
[119] J. Zimmermann *et al.*, (University of Southampton, Southampton, 2008).
[120] J. P. Zimmermann *et al.*, J. Appl. Phys. **99** (2006).
[121] R. P. Boardman *et al.*, J. Mag. Magn. Mater. **312**, 234 (2007).
[122] R. P. Boardman *et al.*, J. Appl. Phys **97** (2005).
[123] G. Bordignon *et al.*, IEEE Trans. Magn. **43**, 2881 (2007).
[124] A. Aharoni, Rev. Mod. Phys **34**, 227 (1962).
[125] W. F. Brown Jr., *Micromagnetics* (Wiley Interscience, New York, 1963).
[126] A. Hubert, and R. Schafer, *Magnetic Domains* (Springer - Verlag, Berlin Heidelberg, 1998, 2000).
[127] J. Zimmermann, private communication, (2007).
[128] A. Fert, and I. A. Campbell, J. Phys. F **6**, 849 (1976).
[129] T. McGuire, and R. Potter, IEEE Trans. Magn. **11**, 1018 (1975).
[130] G. J. Bowden *et al.*, J. Phys. Cond. Matter. **20**, 015209 (2008).

Publications

Micromagnetic simulation of the magnetic exchange spring system $DyFe_2/YFe_2$
J. P. Zimmermann, G. Bordignon, R. P. Boardman, T. Fischbacher, H. Fangohr, K. N. Martin, G. J. Bowden, A. A. Zhukov, P. A. J. de Groot, J. Appl. Phys **99**, 08B904 (2006)

Magnetic anisotropy terms in [110] MBE-grown $REFe_2$ films involving the strain term ε_{xy}
G. J. Bowden, P. A. J. de Groot, B. D. Rainford, K. Wang, K. N. Martin, J. P. Zimmermann, H. Fangohr, J. Phys. Cond. Matt. **18**, 5861 (2006)

Magnetization reversal in micron-sized stripes of epitaxial (110) YFe_2 films
K. Wang, K. N. Martin, C. G. Morrison, R. C. C. Ward, G. J. Bowden, and P. A. J. de Groot, Phys. Stat. solidi (a) **203**, 3831 (2006)

Exchange spring driven spin flop transition in $ErFe_2/YFe_2$ multilayers
K. N. Martin, K. Wang, G. J. Bowden, A. A. Zhukov, P. A. J. de Groot, J. P. Zimmermann, H. Fangohr and R. C. C. Ward, App. Phys. Lett. **89**, 132511 (2006)

Investigation of magnetization reversal in micron-sized stripes of epitaxial-grown (1 1 0) Laves phase $DyFe_2$ films
K. Wang , C. Morrison, K. N. Martin, R. C. C. Ward, G. J. Bowden and P. A. J. de Groot , J. All. Comp **440**, 23 (2007)

Spin-flop transition driven by exchange springs in $ErFe_2/YFe_2$ multilayers
K. N. Martin, K. Wang, G. J. Bowden, P. A. J. de Groot, J. P. Zimmermann, H. Fangohr and R. C. C. Ward, J. App. Phys. **101**, 09K511 (2007)

Engineering coercivity in YFe_2 dominated $DyFe_2/YFe_2$ superlattice by patterning
K. Wang, K. N. Martin, C. G. Morrison, R. C. C. Ward, G. J. Bowden and P. A. J. de Groot, App. Phys. A **86**, 325 (2007)